

CARMENES input catalogue of M dwarfs

V. Luminosities, colours, and spectral energy distributions[★]

C. Cifuentes¹, J. A. Caballero¹, M. Cortés-Contreras^{1,2}, D. Montes³, F. J. Abellán³, R. Dorda⁴, G. Holgado¹, M. R. Zapatero Osorio⁵, J. C. Morales^{6,7}, P. J. Amado⁸, V. M. Passegger^{9,10}, A. Quirrenbach¹¹, A. Reiners¹², I. Ribas^{6,7}, J. Sanz-Forcada¹, A. Schweitzer⁹, W. Seifert¹¹, and E. Solano^{1,2}

¹ Centro de Astrobiología (CSIC-INTA), ESAC, Camino Bajo del Castillo s/n, E-28691 Villanueva de la Cañada, Madrid, Spain
e-mail: ccifuentes@cab.inta-csic.es

² Spanish Virtual Observatory, Spain

³ Departamento de Física de la Tierra y Astrofísica & IPARCOS-UCM (Instituto de Física de Partículas y del Cosmos de la UCM), Facultad de Ciencias Físicas, Universidad Complutense de Madrid, E-28040 Madrid, Spain

⁴ Instituto de Astrofísica de Canarias (IAC), Calle Vía Láctea, s/n, E-38205 San Cristóbal de La Laguna, Tenerife, Spain

⁵ Centro de Astrobiología (CSIC-INTA), Carretera de Ajalvir km 4, E-28850 Torrejón de Ardoz, Madrid, Spain

⁶ Institut de Ciències de l'Espai (CSIC-IEEC), Can Magrans s/n, Campus UAB, E-08193 Bellaterra, Barcelona, Spain

⁷ Institut d'Estudis Espacials de Catalunya (IEEC), E-08034 Barcelona, Spain

⁸ Instituto de Astrofísica de Andalucía (IAA-CSIC), Glorieta de la Astronomía s/n, E-18008 Granada, Spain

⁹ Hamburger Sternwarte, Gojenbergsweg 112, D-21029 Hamburg, Germany

¹⁰ Homer L. Dodge Department of Physics and Astronomy, University of Oklahoma, 440 West Brooks Street, Norman, OK-73019 Oklahoma, United States of America

¹¹ Landessternwarte, Zentrum für Astronomie der Universität Heidelberg, Königstuhl 12, D-69117 Heidelberg, Germany

¹² Institut für Astrophysik, Georg-August-Universität, Friedrich-Hund-Platz 1, D-37077 Göttingen, Germany

Received 29 April 2020 / Accepted 10 July 2020

ABSTRACT

Context. The relevance of M dwarfs in the search for potentially habitable Earth-sized planets has grown significantly in the last years.

Aims. In our on-going effort to comprehensively and accurately characterise confirmed and potential planet-hosting M dwarfs, in particular for the CARMENES survey, we have carried out a comprehensive multi-band photometric analysis involving spectral energy distributions, luminosities, absolute magnitudes, colours, and spectral types, from which we have derived basic astrophysical parameters.

Methods. We have carefully compiled photometry in 20 passbands from the ultraviolet to the mid-infrared, and combined it with the latest parallactic distances and close-multiplicity information, mostly from *Gaia* DR2, of a sample of 2479 K5 V to L8 stars and ultracool dwarfs, including 2210 nearby, bright M dwarfs. For this, we made extensive use of Virtual Observatory tools.

Results. We have homogeneously computed accurate bolometric luminosities and effective temperatures of 1843 single stars, derived their radii and masses, studied the impact of metallicity, and compared our results with the literature. The over 40 000 individually inspected magnitudes, together with the basic data and derived parameters of the stars, individual and averaged by spectral type, have been made public to the astronomical community. In addition, we have reported 40 new close multiple systems and candidates ($\rho < 3.3$ arcsec) and 36 overluminous stars that are assigned to young Galactic populations.

Conclusions. In the new era of exoplanet searches around M dwarfs via transit (e.g. *TESS*, *PLATO*) and radial velocity (e.g. CARMENES, NIRPS+HARPS), this work is of fundamental importance for stellar and therefore planetary parameter determination.

Key words. astronomical data bases – virtual observatory tools – catalogues – stars: low-mass – stars: late-type – planetary systems

1. Introduction

Low-mass stars are remarkably abundant and long-lived objects in the Galaxy. Among them, M dwarfs are by far the most common type of star in the solar neighbourhood, vastly outnumbering their more massive counterparts (Henry et al. 1994, 2006; Reid et al. 2004; Bochanski et al. 2010; Winters et al. 2015). In

their mainly convective interiors, the fusion process is slow and, therefore, the lifespan is long, as they remain on the main sequence for tens of billions of years (Adams & Laughlin 1997; Baraffe et al. 1998). Such abundance and prevalence make low-mass stars very attractive targets for multiple areas of astrophysical research.

Collectively, M dwarfs are excellent probes for the examination of the Galactic structure (Bahcall & Soneira 1980; Scalo 1986; Reid et al. 1997; Chabrier 2003; Pirzkal et al. 2005; Caballero et al. 2008; Ferguson et al. 2017), and are also very convenient tracers of Galactic kinematics and evo-

[★] Table A.3 (summary table) is available at the CDS via anonymous ftp to cdsarc.u-strasbg.fr (130.79.128.5) or via <http://cdsarc.u-strasbg.fr/viz-bin/qcat?J/A+A/MMM/NNN>. An extended version of this table can be downloaded from the GitHub repository <https://github.com/ccifuentesr/CARMENES-V>.

lution (Reid et al. 1995; Gizis et al. 2002; West et al. 2006; Bochanski et al. 2007). Individually, M dwarfs have proven to be interesting targets for the discovery of low-mass exoplanets, and a sizable body of current literature pays special attention to them (e.g. Boss 2006; Tarter et al. 2007; Zechmeister et al. 2009; Bonfils et al. 2013; Mann et al. 2013; Clanton & Gaudi 2014; Dressing & Charbonneau 2015; Fischer et al. 2016; Kopparapu et al. 2017; Reiners et al. 2018b). In particular, low-mass, small-sized stars are particularly suited to the search for close-in terrestrial planets because their detection becomes easier with decreasing stellar size and planetary orbital period (Anglada-Escudé et al. 2016; Gillon et al. 2017; Zechmeister et al. 2019).

Our understanding of how planets form and evolve rests fundamentally on the characterisation of their host stars. As an example, the luminosity of the star determines the equilibrium temperature of its planet and delimits the habitable zone, which is the circumstellar region where water can be liquid (Kasting et al. 1993; Kopparapu et al. 2017, but see Tarter et al. 2007 for the particular M-dwarf case). Determining precise stellar parameters of M dwarfs and how their uncertainties propagate to those of their planets is, therefore, of paramount importance. Many efforts have been undertaken in this respect, including empirical determination of masses, radii, and their relation to luminosity (Veeder 1974; Henry & McCarthy 1993; Chabrier & Baraffe 1997; Delfosse et al. 2000; Bonfils et al. 2005; Mann et al. 2015, 2019; Terrien et al. 2015; Benedict et al. 2016; Schweitzer et al. 2019), effective temperature, surface gravity, and metallicity (Casagrande et al. 2008; Rojas-Ayala et al. 2013; Montes et al. 2018; Passegger et al. 2018, 2019; Rajpurohit et al. 2018a), or activity and rotation periods (Stauffer & Hartmann 1986; Reid et al. 1995; Hawley et al. 1996; Morales et al. 2008; Hawley et al. 2014; Newton et al. 2015; Jeffers et al. 2018; Díez Alonso et al. 2019; Schöfer et al. 2019).

This work is part of a series of papers devoted to describing the CARMENES input catalogue of M dwarfs. CARMENES, the Calar Alto high-Resolution search for M dwarfs with Exoearths with Near-infrared and optical Echelle Spectrographs¹ (Quirrenbach et al. 2014), is the name of an instrument specifically designed for discovering M-dwarf planets with the radial-velocity method, the consortium that built it, and of the science project that is being carried out during guaranteed time observations (GTO; Quirrenbach et al. 2018; Reiners et al. 2018b). Here we continue the work started by Alonso-Floriano et al. (2015b) on spectral typing from low-resolution spectroscopy of M dwarfs (I), and followed up by Cortés-Contreras et al. (2017) on multiplicity from high-resolution lucky imaging (II), Jeffers et al. (2018) on activity from high-resolution spectroscopy (III), and Díez Alonso et al. (2019) on rotation periods from photometric time series (IV).

In this fifth item of the series, we focus on the analysis of multi-wavelength photometry, from the far ultraviolet to the mid infrared, of a large sample of nearby, bright M dwarfs, including those monitored by CARMENES, as well as some late K dwarfs and early and mid L dwarfs. We derive accurate bolometric luminosities, identify new close binaries, members in young stellar kinematic groups, and other outliers in colour-colour, colour-magnitude, and colour-spectral type diagrams. We also explore different relationships between colours, absolute magnitudes, spectral types, luminosities, masses, and radii. For that, we make extensive use of the second data release of *Gaia* astrometry and photometry (*Gaia* DR2; *Gaia* Collaboration et al.

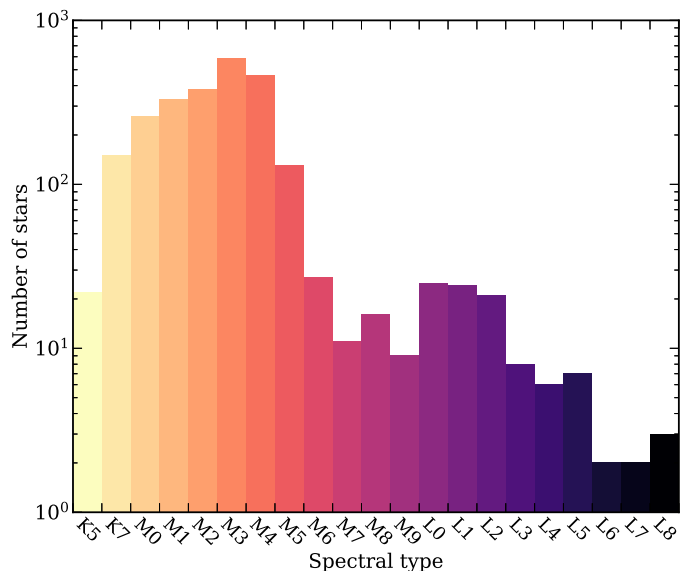


Fig. 1. Distribution of spectral types in our sample.

2018b), numerous public all-sky surveys from the ground and space, and Virtual Observatory tools such as the Aladin interactive sky atlas (Bonnarel et al. 2000), the Tool for OPERations on Catalogues And Tables (TOPCAT; Taylor 2005), and the Virtual Observatory Spectral energy distribution Analyser (VOSA; Bayo et al. 2008).

Our work is also connected to that of Schweitzer et al. (2019), who derived masses and radii from effective temperatures (determined from spectral synthesis) and luminosities (measured exactly as in the present paper) for 293 M dwarfs monitored by CARMENES. As a result, here we complement the description of the calculation of stellar masses and radii of all planet hosts detected by CARMENES (e.g. Reiners et al. 2018a; Ribas et al. 2018; Trifonov et al. 2018; Zechmeister et al. 2019; Luque et al. 2019; Morales et al. 2019, to cite a few).

2. Data

In this Section we describe the building process of our sample, as well as the compilation of their photometric and astrometric data from public catalogues.

2.1. Sample

Our sample is based mainly on Carmencita, the CARMENES input catalogue (Alonso-Floriano et al. 2015b; Caballero et al. 2016). Currently, Carmencita contains 2191 M dwarfs and 3 K dwarfs, namely J04167–120 (LP 714–47), J11110+304E (HD 97101 A), and J18198–019 (HD 168442), which satisfied simple selection criteria based on *J*-band magnitude and spectral type regardless of multiplicity, age, or metallicity (cf. Alonso-Floriano et al. 2015b). Except for the three K dwarfs, Carmencita includes M dwarfs visible from the Calar Alto Observatory in Southern Spain ($\delta \gtrsim -23$ deg) with spectral types from M0.0 V to M9.0 V and near-infrared brightnesses between $J = 4.2$ mag and 11.5 mag. The spectral types, compiled by Caballero et al. (2016), came from a number of sources. However, the spectral types of 2028 M dwarfs (92.5%) were taken from only three references: Hawley et al. (2002), Lépine et al. (2013), and Alonso-Floriano et al. (2015b), which are equivalent among them according to the latter authors. Of the re-

¹ <http://carmenes.caha.es>

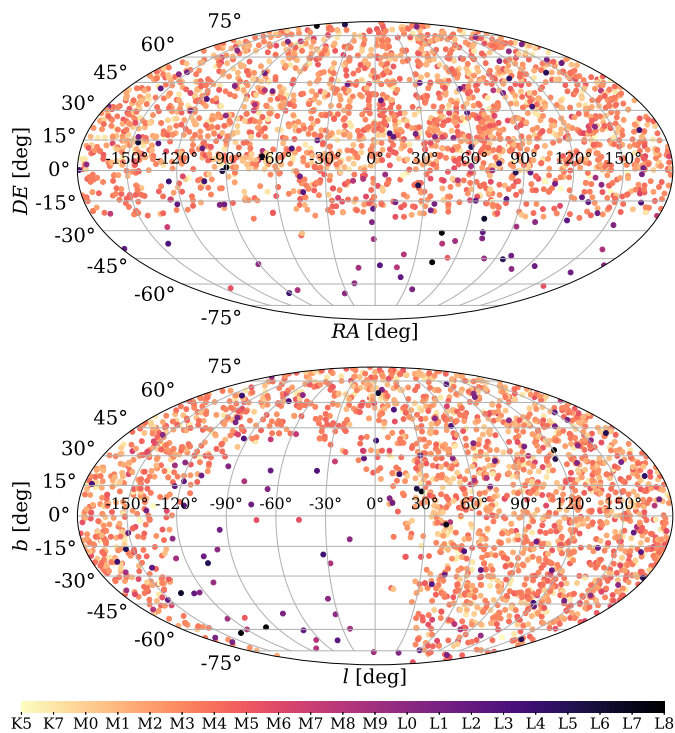


Fig. 2. Location in the sky of the 2479 targets in our sample, colour-coded by spectral type, in equatorial (top) and Galactic coordinates (bottom). We note the absence of Carmencita M dwarfs with declinations lower than $\delta = -23$ deg.

maining 163 M dwarfs, most spectral types also came from reliable, equivalent sources (e.g. Gray et al. 2003; Scholz et al. 2005; Riaz et al. 2006), which assures a relative homogeneity in our sample.

As described in the references above, Carmencita is unbiased except for the fact that it may include overluminous and lack underluminous stars in the J band at a fixed spectral type. This fact probably translates into a larger fraction of (overluminous) close multiples and young active stars, and a lower fraction of (underluminous) very low metallicity M-type dwarfs (subdwarfs and extreme subdwarfs; Gizis 1997; Lépine et al. 2007). From the distribution of the ζ index, a metallicity proxy measured in low-resolution spectra of a large number of Carmencita stars (cf. Alonso-Floriano et al. 2015b), we extrapolated that most of our M dwarfs have solar-like metallicities, but that there could be a significant number of them with $[\text{Fe}/\text{H}] < -1.0$.

In order to extend the photometric sample to a wider spectral range and to avoid any boundary value problem, we complemented Carmencita with additional stars earlier than M0.0 V, and with stars and brown dwarfs later than M6.5 V. The eventual distribution of spectral types is displayed in Fig. 1. On the warm side, we included 168 bright stars with spectral types between K5 V and K7 V from Kirkpatrick et al. (1991), Lépine et al. (2013), and Alonso-Floriano et al. (2015b), and the RECONS list of the 100 nearest stars² (Henry et al. 2006). We did not include the very bright K stars η Cas B, 36 Oph C, BD+01 3942 A, ξ Cap B, 61 Cyg A, and 61 Cyg B, whose photometry is strongly affected by saturation or blending due to close multiplicity.

On the cool side, we first included seven M5.0–9.0 V stars from the REsearch Consortium On Nearby Stars (RECONS) with declinations of $\delta < -23$ deg. Next, we added

² <http://www.recons.org/TOP100.posted.htm>

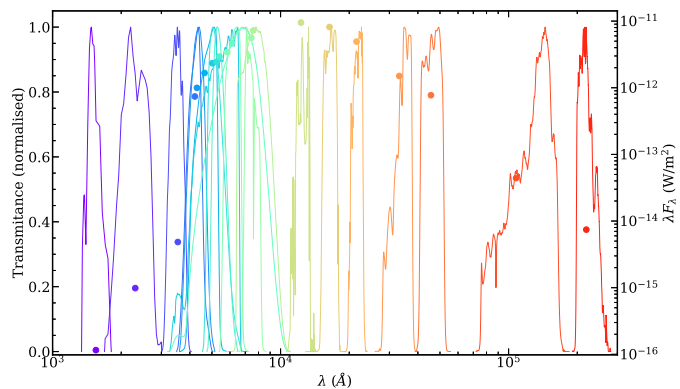


Fig. 3. Normalised transmission curves of the 20 passbands employed for the compilation of photometry, taken from the SVO Filter Profile Service. For comparison, coloured filled circles depict the spectral energy distribution of DS Leo (Karmn J11026+219, M1.0 V).

110 ultracool dwarfs from Smart et al. (2017) with a Two Micron All-Sky Survey (2MASS) near-infrared counterpart (Skrutskie et al. 2006) and relative error in *Gaia* DR2 parallaxes ($\delta\varpi/\varpi$) less than 1%. That addition made 12 M8.0–9.5 V and 98 L0.0–8.0 ultracool dwarfs. We did not include four T-type brown dwarfs (SIMP J013656.57+093347.3, ULAS J141623.94+134836.30, 2MASS 15031961+2525196, and WISE J203042.79+074934.7) and one L dwarf, HD 16270 B, because of their poor 2MASS photometric quality (see Sect. 2.2).

As a result, the joint K-M-L spectro-photometric sample contained 2479 targets distributed among 171 late-K dwarfs, 2210 M dwarfs, and 98 L dwarfs. For all targets in the sample we employed and tabulated equatorial coordinates from *Gaia* DR2 except for the 58 stars (five K, 53 M) that were not catalogued by the ESA space mission. For all 58 stars, we used the positions at the epoch of 2MASS projected to the epoch J2015.5 with proper motions from van Leeuwen (2007) and Zacharias et al. (2012), as compiled by Caballero et al. (2016).

The spatial distribution of the 2479 targets is illustrated in Fig. 2. For the sake of simplicity, we will use hereafter the term “stars” for the 2479 objects in our sample, including the stellar and substellar objects later than M7 V, also known as ultracool dwarfs (Kirkpatrick et al. 1997).

2.2. Photometry

For every star in the sample, we compiled multiwavelength broadband photometry covering a wide spectral range from the ultraviolet to the mid-infrared, as illustrated in Fig. 3. First of all, with Aladin we manually retrieved the 2MASS equatorial coordinates, JHK_s magnitudes and uncertainties, and photometric quality flags of all 2479 stars (we had done this previously for the Carmencita stars; Caballero et al. 2016). Next, we added photometric data from different public catalogues. We started by adding *Gaia* DR2 G , G_{BP} , and G_{RP} magnitudes, obtained with the query form available in the *Gaia* Archive³. We followed by adding magnitudes and uncertainties of the Galaxy Evolution Explorer (*GALEX*) FUV and NUV , the Ninth Sloan Digital Sky Survey Data Release (SDSS9) $u'g'r'i'$, Tycho-2 B_T and V_T , the AAVSO Photometric All-Sky Survey Data Release 9 (APASS9) B and V , the Fourth US Naval Observatory CCD Astrograph Catalog (UCAC4) $BVG'r'i'$, the Carlsberg Meridian

³ <http://gea.esac.esa.int/archive/>

Table 1. Passbands employed for the compilation of photometry.

Band	λ_{eff} (Å)	W_{eff} (Å)	F_{λ}^0 (W m ⁻² Å ⁻¹)	Survey ^a	Description
<i>FUV</i>	1549.0	265.6	6.491×10^{-12}	<i>GALEX</i>	<i>GALEX FUV</i>
<i>NUV</i>	2304.7	768.3	4.450×10^{-12}	<i>GALEX</i>	<i>GALEX NUV</i>
<i>u'</i>	3594.9	558.4	3.639×10^{-12}	SDSS9	SDSS <i>u'</i> full transmission
<i>B_T</i>	4206.4	708.4	6.598×10^{-12}	Tycho-2	Tycho <i>B</i>
<i>B</i>	4297.2	843.1	6.491×10^{-12}	UCAC4	UCAC4 <i>B</i> filter, defined as identical to GCPD/Johnson.B_Landolt
	4297.2	843.1	6.491×10^{-12}	APASS9	APASS <i>B</i> filter, defined as identical to GCPD/Johnson.B_Landolt
<i>g'</i>	4640.4	1158.4	5.521×10^{-12}	UCAC4	UCAC4 <i>g'</i> filter, defined as identical to MISC/APASS.sdss_g and SLOAN/SDSS.g
	4640.4	1158.4	5.521×10^{-12}	SDSS9	SDSS <i>g'</i> full transmission
	4640.4	1158.4	5.521×10^{-12}	APASS9	APASS <i>g'</i> filter, defined as identical to SLOAN/SDSS.g
	4810.8	1053.1	5.043×10^{-12}	PS1 DR1	PS1 <i>g'</i> filter
<i>G_{BP}</i>	5020.9	2279.5	4.035×10^{-12}	<i>Gaia</i> DR2	<i>Gaia G_{BP}</i> filter, DR2 revised curve
<i>V_T</i>	5243.9	1005.7	3.984×10^{-12}	Tycho-2	Tycho <i>V</i>
<i>V</i>	5394.3	870.6	3.734×10^{-12}	UCAC4	UCAC4 <i>V</i> filter, defined as identical to GCPD/Johnson.V_Landolt
	5394.3	870.6	3.734×10^{-12}	APASS9	APASS <i>V</i> filter, defined as identical to GCPD/Johnson.V_Landolt
<i>r'</i>	6122.3	1111.2	2.529×10^{-12}	UCAC4	UCAC4 <i>r'</i> filter, defined as identical to MISC/APASS.sdss_r and SLOAN/SDSS.r
	6122.3	1111.2	2.529×10^{-12}	SDSS9	SDSS <i>r'</i> full transmission
	6122.3	1111.2	2.529×10^{-12}	APASS9	APASS <i>r'</i> filter, defined as identical to SLOAN/SDSS.r
	6122.3	1318.1	2.529×10^{-12}	CMC15	SDSS <i>r'</i> full transmission
	6156.4	1252.4	2.480×10^{-12}	PS1 DR1	PS1 <i>r'</i> filter
<i>G</i>	5836.3	4358.4	2.495×10^{-12}	<i>Gaia</i> DR2	<i>Gaia G</i> filter, DR2 revised curve
<i>i'</i>	7439.5	1044.6	1.409×10^{-12}	UCAC4	UCAC4 <i>i'</i> filter, defined as identical to MISC/APASS.sdss_i and SLOAN/SDSS.i
	7439.5	1044.6	1.409×10^{-12}	SDSS9	SDSS <i>i'</i> full transmission
	7439.5	1044.6	1.409×10^{-12}	APASS9	APASS <i>i'</i> filter, defined as identical to SLOAN/SDSS.i
	7503.7	1206.6	1.372×10^{-12}	PS1 DR1	PS1 <i>i'</i> filter
<i>G_{RP}</i>	7588.8	2943.7	1.294×10^{-12}	<i>Gaia</i> DR2	<i>Gaia G_{RP}</i> filter, DR2 revised curve
<i>J</i>	12285.4	1624.2	3.143×10^{-13}	2MASS	2MASS <i>J</i>
<i>H</i>	16386.1	2509.4	1.144×10^{-13}	2MASS	2MASS <i>H</i>
<i>K_s</i>	21521.6	2618.9	4.306×10^{-14}	2MASS	2MASS <i>K_s</i>
<i>W1</i>	33156.6	6626.4	8.238×10^{-15}	AllWISE	WISE <i>W1</i> filter
	33156.6	6626.4	8.238×10^{-15}	WISE	WISE <i>W1</i> filter
<i>W2</i>	45644.9	10422.7	2.431×10^{-15}	AllWISE	WISE <i>W2</i> filter
	45644.9	10422.7	2.431×10^{-15}	WISE	WISE <i>W2</i> filter
<i>W3</i>	107868.4	55055.7	6.570×10^{-17}	AllWISE	WISE <i>W3</i> filter
	107868.4	55055.7	6.570×10^{-17}	WISE	WISE <i>W3</i> filter
<i>W4</i>	219149.6	41016.8	4.995×10^{-18}	AllWISE	WISE <i>W4</i> filter
	219149.6	41016.8	4.995×10^{-18}	WISE	WISE <i>W4</i> filter

Notes. ^(a) *GALEX* DR5: Galaxy Evolution Explorer, Bianchi et al. (2011); SDSS DR9: Sloan Digital Sky Survey, Ahn et al. (2012); UCAC4: The fourth U.S. Naval Observatory CCD Astrograph Catalog, Zacharias et al. (2012); Pan-STARRS1: Panoramic Survey Telescope and Rapid Response System, Kaiser et al. (2010), Tonry et al. (2012), and Chambers et al. (2016); CMC15: Carlsberg Meridian Catalogue, Niels Bohr Institute et al. (2014); APASS9: The AAVSO Photometric All-Sky Survey, Henden et al. (2016); Tycho-2: Høg et al. (2000); 2MASS: Two Micron All-Sky Survey, Skrutskie et al. (2006); *Gaia* DR2: *Gaia* Collaboration et al. (2016); Evans et al. (2018) with the revised response curves of Maíz Apellániz & Weiler (2018); AllWISE: Cutri & et al. (2014); WISE: Wide-field Infrared Survey Explorer, Cutri & et al. (2012).

Catalogue 15 (CMC15) *r'*, and of the Wide-field Infrared Survey Explorer (AllWISE and WISE) *W1W2W3W4* (and their quality flags when available). For that, we used the TOPCAT automatic positional cross-match tool CDS X-match with a search radius of 5 arcsec and the “All” find option. For a few high proper motion stars, we enlarged the search radius to 10 arcsec. Next we used Aladin to: (i) visually inspect the automatic cross-matches of all sources (and correct them, especially in mismatched cases of high proper motion and close binary sources), and (ii) compile, by hand, the most reliable photometry of Pan-STARRS1 DR1 only for the stars for which *g'*, *r'*, or *i'* magnitudes were not available in other catalogues (PS1 DR1 delivered up to 60 multi-epoch observations for every star over three years in the five PS1 passbands). The passband name, effective wavelength λ_{eff} , effective width W_{eff} , zero point flux F_{λ}^0 , survey acronym, and corresponding references of the 20 compiled passbands are listed in Table 1. The passband parameters were calculated by

VOSA with the latest filter transmission curves available at the Filter Profile Service⁴ of the Spanish Virtual Observatory. When there were several surveys providing photometric data in the same passband (e.g. *r'* in UCAC4, SDSS9, APASS9, and PS1 DR1), we prioritised the surveys with the highest spatial resolution, sensitivity, and accuracy. PanSTARRS1 DR1 has slightly different passband parameters from those of the other *g'r'i'* surveys. Virtually all our K and M dwarfs saturated or were in the non-linear regime in SDSS9 *z'* and PS1 DR1 *z'y'*, so we did not compile data in these passbands.

Gaia *G*, *G_{BP}*, and *G_{RP}* magnitude uncertainties were derived from the uncertainties in the fluxes, while UCAC4 *BVg'r'i'* magnitude uncertainties were collected from an additional TOPCAT table access protocol query. However, we chose APASS9 *BV* over UCAC4 *BV* when the UCAC4 uncertainties were

⁴ <http://svo2.cab.inta-csic.es/theory/fps/>

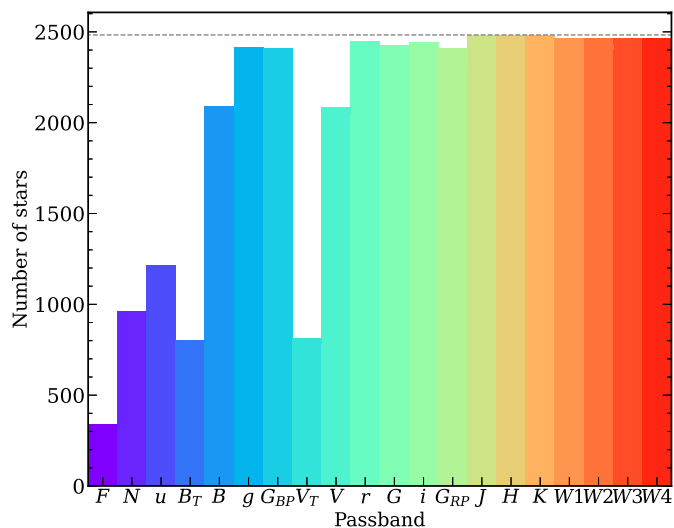


Fig. 4. Completeness in every passband. Light shaded regions account for measurements with poor quality flags. The dashed horizontal line indicates the total number of stars in the sample.

0.00 mag, 0.99 mag, or missing. In the case of poor photometric quality in AllWISE *W1* to *W4* (*Qflag* \neq A,B), we chose the data available in WISE when it improved the quality of AllWISE data. We also identified possible flux excesses in the *Gaia* DR2 *G_{BP}* and *G_{RP}* photometric data with the keyword *phot_bp_rp_excess_factor*, following the guidelines of Evans et al. (2018) to separate well-behaved single sources from spurious ones.

J band magnitudes are available for all the stars in the sample, and the completeness in passbands *g'*, *G_{BP}*, *G*, *r'*, *i'*, *G_{RP}*, *H*, *K_s*, *W1*, *W2*, *W3*, and *W4* is greater than 97%. For Johnson *B* and *V* the completeness is around 86%, whereas for Tycho-2 *B_T* and *V_T* it is only 25%. At the blue end, *u'* is complete for 50% of the sample, and the ultraviolet passbands *FUV* and *NUV* are available for 39% and 14%, respectively. This is graphically summarised in Fig. 4.

In total, we collected 40 094 individual magnitudes. Of them, 39 896 have magnitude uncertainties and 33 594 have good quality photometry, defined as: 2MASS *Qflag* = A (with signal-to-noise ratio ≥ 10), WISE *Qflag* = A,B, *G_{BP}* < 19.5 mag (see Sect. 3.3.2), and no flux excess in *Gaia* *G_{BP}* and *G_{RP}*. Figure 5 shows the distribution of magnitudes for each band, ordered by increasing λ_{mean} . The distributions of the bluest bands are broader than the redder ones, while those of the most complete bands (e.g. *g'*, *r'*, *G*, *J*, *W1*) exhibit small secondary peaks at fainter magnitudes, which correspond to late M and early L dwarfs.

2.3. Distances

We compiled equatorial coordinates, proper motions, parallaxes, and astrometric quality indicators from *Gaia* DR2. Of the 2479 stars in our sample, 2425 (97.8%) had parallactic distances. Of them, 2306 parallaxes came from *Gaia* DR2 (93.0%) and 119 from a number of references, as detailed in Table 2. For 16 stars with unavailable parallactic distances, we used the trigonometric distances of their confirmed proper motion companions from *Gaia* DR2 (ten cases) and van Leeuwen (2007, six cases). As a result, there were 54 stars without parallactic distance, of which 23 are close binaries: four spectroscopic binaries from

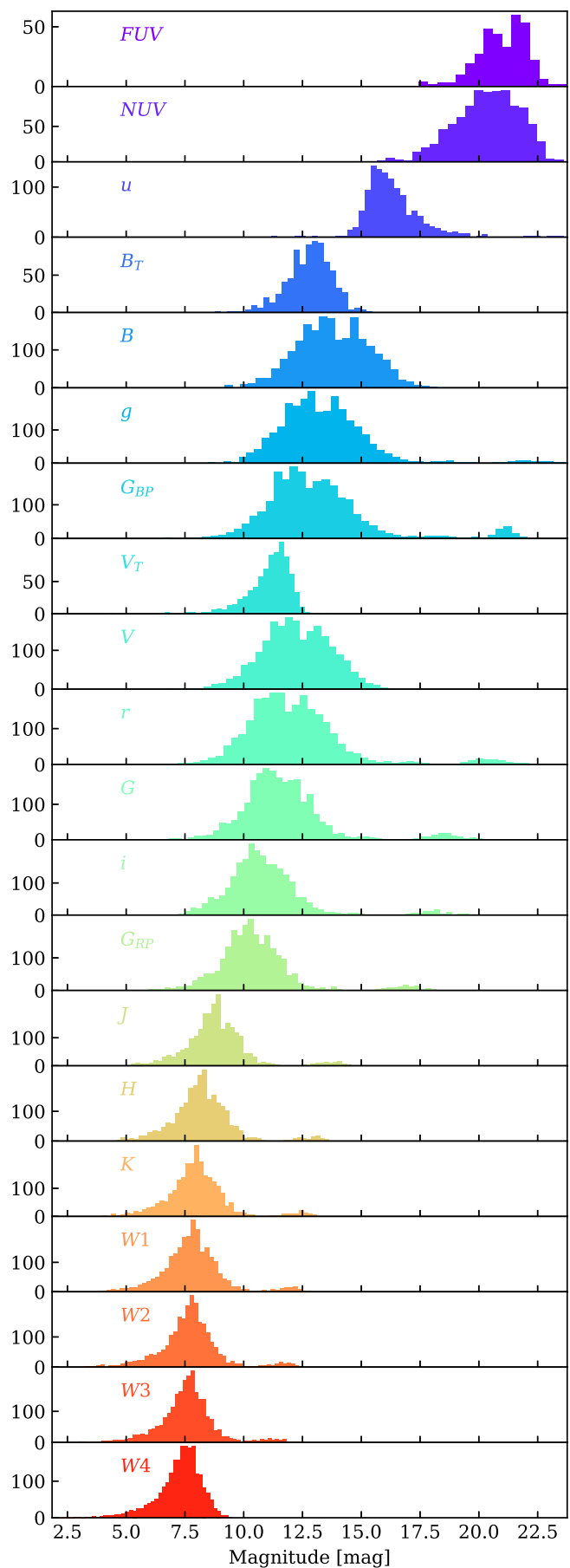
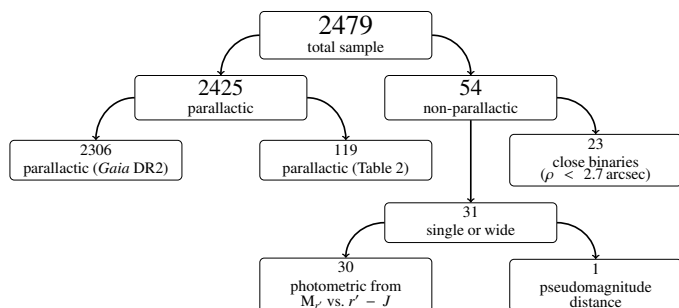


Fig. 5. Distribution of compiled magnitudes in every passband. The width of the bins follows the Freedman-Diaconis rule.

Table 2. Reference of the 2425 parallactic distances in the sample.

Acronym ^a	Number of stars	Reference
Gaia2	2306	Gaia Collaboration et al. 2018b
HIP2	41	van Leeuwen 2007
Dit14	34	Dittmann et al. 2014
vAl95	16	van Altena et al. 1995
FZ16	14	Finch & Zacharias 2016
Galli18	2	Galli et al. 2018
Hen06	2	Henry et al. 2006
Jao05	2	Jao et al. 2005
Wein16	2	Weinberger et al. 2016
Dahn17	1	Dahn et al. 2017
GC09	1	Gatewood & Coban 2009
Jen52	1	Jenkins 1952
Lep09	1	Lépine et al. 2009
Ried10	1	Riedel et al. 2010
TGAS	1	Gaia Collaboration et al. 2016

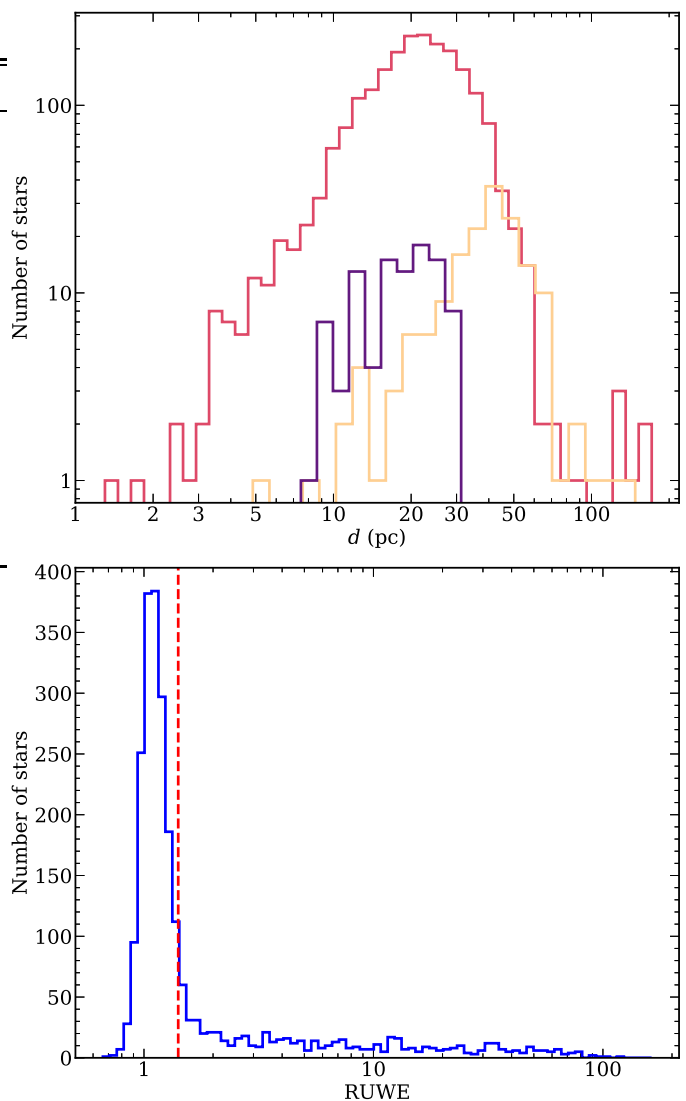
Notes. ^(a) Acronyms used in on-line table.


Fig. 6. Schematic diagram of sources of heliocentric distances.

Reiners et al. (2012) and Jeffers et al. (2018), and 19 resolved binaries (16 with $\rho \lesssim 0.8$ arcsec, and three at $\rho = 1.1$ –2.7 arcsec; see Sect. 2.4). The remaining 31 stars are single or have wide companions at angular separations of $\rho > 16$ arcsec. For 30 of them, we derived photometric distances from $r' - J$ colours following the prescription in Sect. 3.3.3. For the remaining star, a Pleiades member with an $r' - J$ colour outside the validity range, we adopted the “pseudomagnitude” distance to the open cluster of Chelli & Duvert (2016). As a result, we compiled or derived distances for 2456 stars (i.e. all but the 23 close binaries without parallax). Figure 6 shows a schematic summary of the origin of all compiled distances.

Our sample spans a distance range from 1.30 pc (Proxima Centauri) to 171 pc (Haro 6–36). However, ignoring late K dwarfs, overluminous young M dwarfs (in Taurus, Upper Scorpius, and the β Pictoris moving group; Sect. 3.2), and one star with a large parallax uncertainty ($\delta\varpi/\varpi \sim 8\%$), the most distant “regular” M dwarf is LP 415–17, at 73.0 pc (Díez Alonso et al. 2018; Hirano et al. 2018). Actually, 92% of the stars are at less than 40 pc, with only half a dozen objects further than 100 pc. The top panel in Fig. 7 shows the distance distribution of our K, M, and L sub-samples.

Gaia DR2 provides statistical parameters to assess the quality of the astrometric data for each source. The a posteriori mean error of unit weight (UWE) is a goodness-of-fit indicator that is implicit in the Gaia DR2 solution. Because of its strong dependence on colour and magnitude, a re-normalised UWE, or RUWE, is a more convenient indicator of well-behaved astrometric solu-


Fig. 7. Histogram of distances for all stars in the sample, for K (yellow), M (red), and L (violet) dwarfs (top), and RUWE values for the stars identified in the Gaia DR2 catalogue (bottom). The vertical red dashed line in the bottom panel sets the threshold for well-behaved astrometric solutions at RUWE = 1.41.

tions (Arenou et al. 2018; Lindegren et al. 2018). The latter authors set a threshold on RUWE at 1.4, based on the empirical distribution of a large sample of stars, under which they retained 70% of their sources. We derived the RUWE values for all stars with Gaia DR2 measurements in our sample (2421; there are 125 Gaia DR2 stars without parallax), and display the corresponding RUWE histogram in the bottom panel of Fig. 7. In our case, by retaining 70% of our sources we re-defined a cut in RUWE = 1.41, which is equivalent to the 1.4 value.

Our sample is not volume limited. First, its basis, the Carmencita catalogue, is not complete. Carmencita contains all known M dwarfs in the solar neighbourhood that are further north than $\delta = -23$ deg with published “spectroscopic” (i.e. non-photometric) spectral types that are brighter than the completeness magnitudes shown in Alonso-Floriano et al. (2015b), meaning they are magnitude limited by spectral subtype: M0.0–0.5 V with $J < 7.3$ mag, M1.0–1.5 V with $J < 7.8$ mag, M2.0–2.5 V with $J < 8.3$ mag, and so on. We refer the reader to the consequences of these selection criteria on the metallicity properties

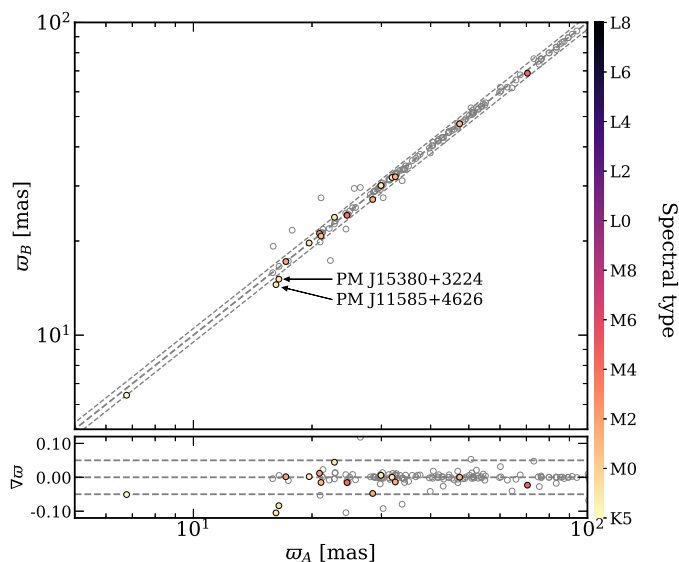


Fig. 8. Parallax diagram of the primary (A) and secondary (B) components of the 15 new binary systems in Table A.1 with parallactic information in both components, colour-coded by spectral type. The bottom panel shows the normalised difference between both parallaxes, i.e. $\nabla\varpi = (\varpi_B - \varpi_A)/\varpi_A$. Grey empty circles are the 134 previously known pairs in our sample with parallactic information for both components and angular separation of $\rho < 5$ arcsec. The black dash-dotted and dashed lines mark the 1:1 and $1:1 \pm 0.05$ (i.e. 5% difference), respectively. Two slight outliers from our list of binary candidates are labelled with their common names.

of the sample described in Sect. 2.1. Next, the K dwarf and ultra-cool dwarf additions are not complete either, because, for example, we discarded known K and L dwarf binaries. However, from the distribution of distances, our sample in the Calar Alto sky is complete for M0.0 V, M4.0 V, and M6.0 V stars at approximate distances of 25 pc, 15 pc, and 5 pc, respectively.

2.4. Multiplicity

We searched for additional *Gaia* DR2 sources within 5 arcsec of our target stars at epoch J2015.5 using the ADQL⁵ query form in the *Gaia* Archive. According to [Gaia Collaboration et al. \(2018b\)](#) and, especially, [Arenou et al. \(2018\)](#), *Gaia* can resolve equal-brightness sources separated by down to 0.4 arcsec, which were not resolved in most previous all-sky surveys, such as 2MASS or AllWISE (see [Caballero et al. 2019](#) for a practical example of close binaries resolved for the first time by *Gaia*). For the 2421 stars in our sample that were catalogued by *Gaia*, the search provided 388 additional sources around 353 stars at $\rho < 5$ arcsec. Of them, 324 stars had only one additional source, 24 stars had two sources, 4 stars had three sources, and 1 star had four sources. Besides, for the 58 stars in our sample not tabulated in the *Gaia* catalogue, we used the projected positions as explained in Sect. 2.1, which resulted in 11 additional sources around 6 stars. The cases of three or more additional sources corresponded to stars in crowded regions at low Galactic latitudes.

Of the 359 stars with close *Gaia* companion candidates, 166 were already tabulated as members in known physical pairs in the Washington Double Star catalogue ([Mason et al. 2001](#)), 4 in [Ansdell et al. \(2015\)](#), and 1 in [Heintz \(1987\)](#). Next, we analysed in detail the remaining 188 systems. Of these, we classified 148 faint sources as background stars and point-like galaxies based

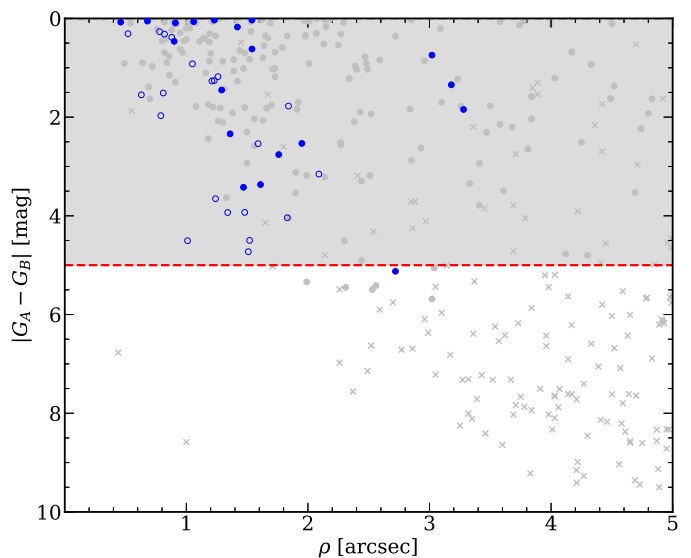


Fig. 9. Difference in the *Gaia* *G* magnitude values for the 359 stars with their closest companion within 5 arcsec as a function of angular separation at epoch J2015.5. Known binaries and background stars are depicted with grey filled circles and grey crosses, respectively. New binaries are represented with blue circles, filled if they are confirmed by common parallactic distance, and open if only one component has a measured parallax. The red dashed line marks the boundary at $\Delta G = 5$ mag for contaminated sources.

on astrometric and photometric criteria: 96 sources have parallaxes $\varpi < 2$ mas and so are located at more than 0.5 kpc; four sources have parallaxes $2 \text{ mas} < \varpi < 7$ mas and turned to be unrelated sources at 47–225 pc (Bayesian distances computed by [Bailer-Jones et al. 2018](#)); one source with a parallax of 21.3 mas is located twice as far as the main source; and 47 sources do not have measured parallaxes, proper motions, or 2MASS near-infrared counterparts. In spite of being more than 5 mag fainter than the primary in *G* band, all 47 sources are visible in digitisations of blue photographic plates of the 1950s (Digitised Sky Survey I), implying that they are background sources much bluer than the stellar primaries⁶.

We investigated the remaining 40 sources not included in the two previous groups. Of them, 15 are in physically bound systems with *Gaia* parallaxes for both components that agree within 1σ errors except for two cases, marked in Fig. 8. The two systems are bona fide high proper motion pairs, for which we see that the tangential component of the orbital motion and the *Gaia* astrometric solution has not yet taken the close binarity into account. All remaining 25 candidate companions are not visible in the Digitised Sky Survey I and satisfy $\Delta G \lesssim 5$ mag ($\Delta G \sim 0.3$ mag in three cases with G_{BP} , G , and G_{RP} photometry; see below). In Table A.1 we list the *Gaia* DR2 equatorial coordinates, proper motions, parallaxes, *G* magnitudes, angular separations ρ , and position angles θ of the 40 new binary systems and candidates. Among them, there are three triple systems consisting of a spectroscopic binary and a fainter companion (see Table A.1 notes). All systems are separated by 3.3 arcsec at most, which explains why other surveys, such as 2MASS, were not able to resolve them.

In the presence of a close companion, either physically associated or not, photometric measurements of a star can be com-

⁶ However, there are certain systems that deserve a high-resolution imaging follow-up, such as J02033–212 (G 272–145), J04429+189 (HD 285968), J05466+441 (Wolf 237), and J11311–149 (LP 732–035).

⁵ <http://www.ivoa.net/documents/ADQL/>

Table 3. Set of constraints for the spectral energy distribution modelling in VOSA^a.

Spectral types	T_{eff} [K]	$\log g$ [dex]
K5 V to M2.0 V	3300–4600	4.5–5.0
M2.5 V to M5.0 V	2800–3700	4.5–5.5
M5.5 V to L8.0	1200–3200	5.0–5.5

Notes. ^(a) Iron abundance set to zero ($[\text{Fe}/\text{H}] = 0.0$).

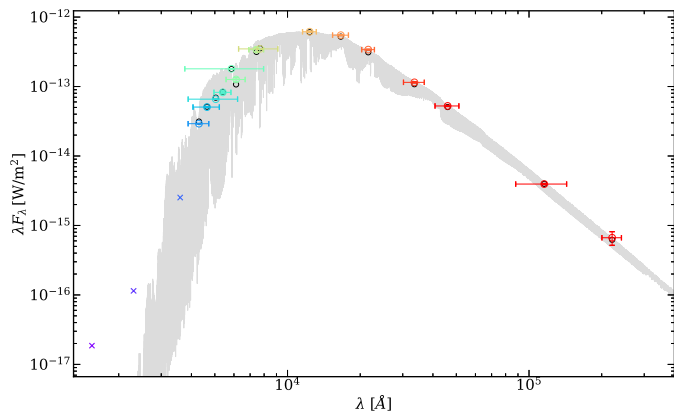


Fig. 10. Spectral energy distribution of LP 167–071 (J10384+485, M3.0 V). The empirical fluxes (coloured empty circles, following the same colour scheme as in Fig. 5) are overlaid on the best-fitting BT-Settl CIFIST spectrum (grey; $T_{\text{eff}} = 3300$ K and $\log g = 5.5$). The modelled fluxes are depicted as grey empty circles. Photometric data in the ultraviolet are shown as crosses, and are not considered in the modelling. Horizontal bars represent the effective widths of the bandpasses, while vertical bars (visible only for relatively large values) represent the flux uncertainty derived from the magnitude and parallax errors.

promised, especially when their brightness is comparable. This photometric contamination impacts negatively on the parameters derived from it, such as luminosity, distance, or colours. In this work, we considered the photometry of a star as contaminated if the G flux of any companion at $\rho < 5$ arcsec, regardless of physical binding, is more than 1% of its flux, that is if $\Delta G < -2.5 \log(F_{G,B}/F_{G,A}) = 5$ mag, where $F_{G,A}$ and $F_{G,B}$ represent the fluxes of the primary and secondary components in the G band, respectively. In Fig. 9 we plot ΔG versus ρ of the 359 pairs in our sample with $\rho < 5$ arcsec. Of them, 238 meet the criteria above, and their photometry is therefore flagged as potentially contaminated. To those 238 stars we added another 372 stars from Caballero et al. (2016) that are known to be very close physical systems unresolved by *Gaia* (but resolved with micrometers, speckle, lucky imaging, or adaptive optics systems) and spectroscopic binaries. The 610 “close binaries” are plotted as a reference in most figures afterwards with grey dots, but will not be considered in the following analysis.

3. Analysis and results

In this Section we present the main products of the exploitation of the astrometric and photometric data in the sample, including luminosities, masses, radii, colours, and bolometric corrections.

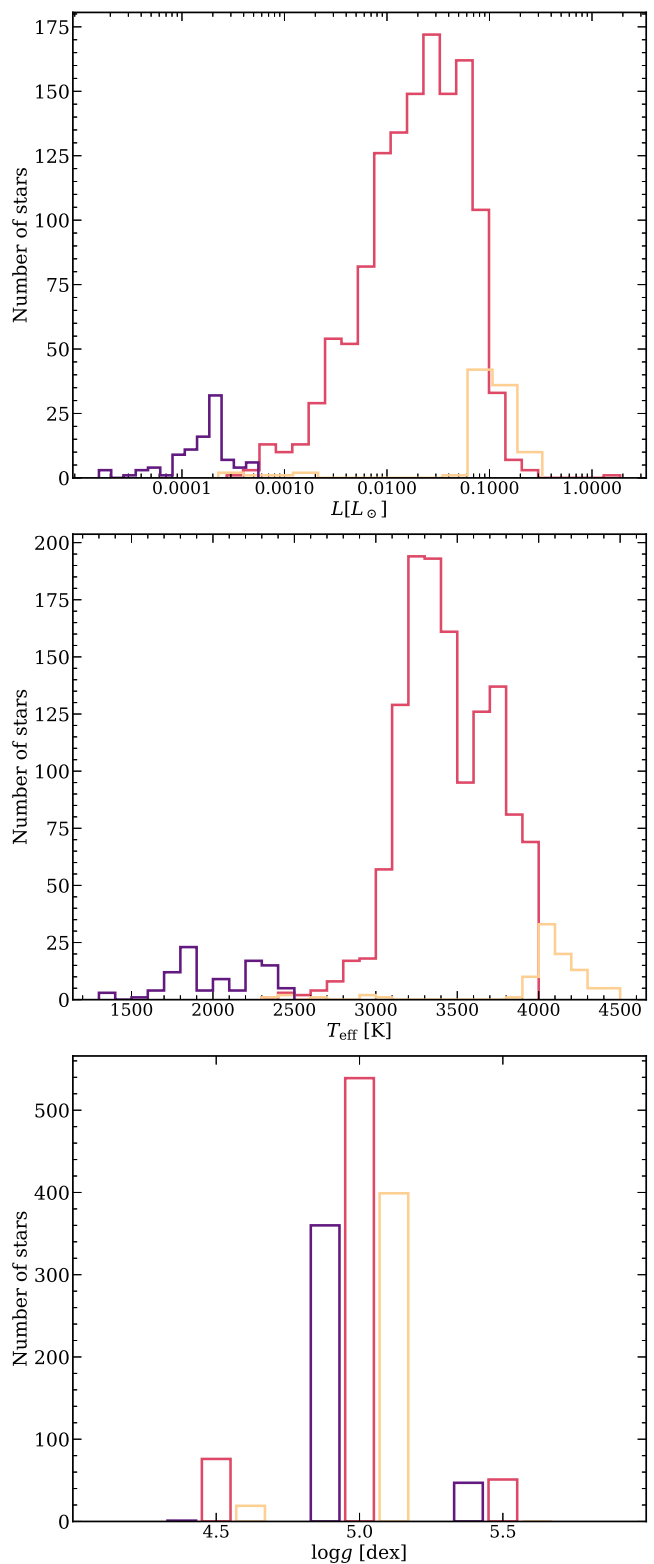


Fig. 11. Distribution of bolometric luminosities (top), effective temperatures (middle), and surface gravities (bottom) for K (yellow), M (red), and L (violet) dwarfs.

3.1. Luminosities

After discarding the 610 close binaries ($\rho < 5$ arcsec), we kept 1843 stars with parallax and whose photometry was not affected by close multiplicity (however, many of the latter are members of wide multiple systems; Cortés-Contreras et al. 2017).

We used VOSA to compute their basic stellar parameters: bolometric luminosity, L_{bol} , effective temperature, T_{eff} , and surface gravity, $\log g$. Among the theoretical model grids available in VOSA for reproducing the observed spectral energy distribution (SED) of each target star, we used the latest BT-Settl CIFIST grid (Husser et al. 2013; Baraffe et al. 2015). We conservatively constrained the possible values of T_{eff} and $\log g$ as a function of spectral type as discussed by Pecaut & Mamajek (2013) and Passegger et al. (2018), respectively, and summarised in Table 3. We fixed the metallicity to solar (BT-Settl CIFIST models are provided for $[\text{Fe}/\text{H}] = 0.0$ only) and visual extinction to zero ($A_V = 0$ mag, in view of the closeness of the overall sample; see Sect. 2.3). For each star, the VOSA input was the compiled photometry in the passbands in Table 1, parallaxic distance, and their uncertainties.

In the fitting process, we included the observed fluxes of up to 17 passbands, from optical Tycho-2 B_T to mid-infrared All-WISE W4. Since we were only interested in the photospheric emission, we excluded from the fit the other three passbands (i.e. GALEX FUV and NUV and SDSS9 u') because the chromospheric emission dominates in the bluest spectral range, especially in late-M dwarfs (Reiners et al. 2012; Stelzer et al. 2013). At wavelengths bluewards of B_T ($\lambda < 4280 \text{ \AA}$) and redwards of W4 ($\lambda > 220883 \text{ \AA}$) we followed the VOSA best-fit model (see example in Fig. 10). The uncertainty in this assumption was very small, as the estimated fraction of photospheric energy in BT-Settl CIFIST spectra bluewards of B_T (in the Wien domain) ranges from 0.46 % to 0.0002 % for M0 V and M8 V, respectively, and redwards of W4 (in the Rayleigh-Jeans domain) ranges from 0.0036 % to 0.0087 % for M0 V and M8 V, respectively.

For the best fit, VOSA uses a χ^2 metric, where each photometric point is weighted with its uncertainty. If this uncertainty is blank or artificially set to zero, VOSA assumes a large value instead, which depends on the largest relative error on the SED, and assigns to the point a low weight⁷. The theoretical uncertainties of T_{eff} and $\log g$ are determined by the BT-Settl CIFIST model grid, which provides synthetic models in steps of 100 K (50 K for spectra cooler than 2400 K) and 0.5 dex, respectively. VOSA estimates the error in the output parameters as half the grid step around the best-fit value.

Complementing the VOSA automatic identification of photometric outliers in the SED, we inspected all the 1843 individual SEDs and marked 7.1 % of all data points as ‘Bad’, as they had bad quality flags (Sect. 2.2) or clearly deviated from the SED trend in the optical and, therefore, were not included in the model fitting. After a careful inspection, we also ignored the possible infrared excesses automatically detected by VOSA, even for the two single, very young stars in the Taurus-Auriga association (see Sect. 3.2).

In Fig. 11 we show the distributions of luminosities, effective temperatures, and surface gravities stacked by spectral type. We derived luminosity values ranging from $1.54 \cdot 10^{-5} L_{\odot}$ for the nearby L8 dwarf DENIS-P J0255-4700, to $0.3276 L_{\odot}$ for the K7 V dwarf HD 196795, except for a very young early M member of the β Pictoris moving group, namely StKM 1-1155, which has an exceptional luminosity of $1.8817 L_{\odot}$. Although very similar, our luminosities supersede those tabulated by Schweitzer et al. (2019) for the M dwarfs in the CARMENES GTO survey, as we updated some parallaxic distances and APASS9 and PS1 DR1 optical magnitudes.

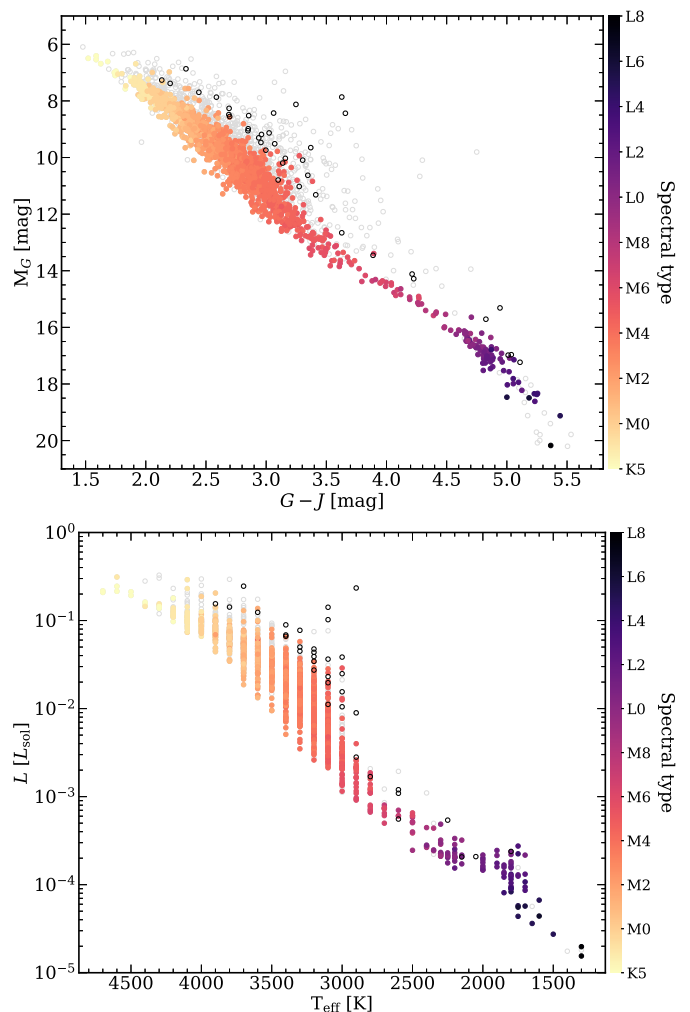


Fig. 12. Absolute magnitude M_G against $G - J$ colour (top), and bolometric luminosity against effective temperature from VOSA (bottom). In the top panel, empty grey circles represent stars with poor photometric quality data in G , J , or both passbands (Sect. 2.2), poor astrometric quality data (RUWE > 1.41) or non-parallaxic distances (Sect. 2.3), and close binary stars (Sect. 2.4). In the bottom panel, empty grey circles represent stars with poor astrometric quality data or non-parallaxic distances, and close binary stars. In both panels, black empty circles are the 36 known young overluminous stars identified in our sample. The remaining ‘regular’ stars are colour-coded by spectral type.

3.2. Young star candidates

In the two panels of Fig. 12 we display two related plots: a Hertzsprung-Russell diagram with luminosities and effective temperatures from our VOSA analysis, and a colour-absolute magnitude diagram with *Gaia* and 2MASS data. After discarding stars with poor astro-photometric data or very close companions, we identified overluminous stars that departed from the main sequence defined by ‘regular’ single stars in the M_G versus $G - J$ diagram, as in the case of StKM 1-1155. We searched the literature for information on their membership in known young kinematic groups (i.e. younger than or of the age of the Hyades, $\tau \lesssim 0.6$ Ga – Perryman et al. 1998; Montes et al. 2001; Zuckerman & Song 2004). The 36 identified overluminous stars include members of very young associations and moving groups (Taurus-Auriga, Upper Scorpius, β Pictoris), moderately young groups (Argus, Tucana-Horologium, Columba, IC 2391 super-cluster), middle-aged open clusters and groups (Pleiades, AB

⁷ <http://svo2.cab.inta-csic.es/theory/vosa/>

Table 4. Overluminous young stars identified in our sample.

Karmn	Name	Stellar kinematic group	Reference
J0045+1634 ^a	2MUCD 20037	Argus	Gagné et al. 2014
J01352-072	Barta 161 12	β Pictoris	Alonso-Floriano et al. 2015a
J02443+109W	MCC 401	β Pictoris	Janson et al. 2017
J03510+142	2MASS J03510078+1413398	β Pictoris	Gagné et al. 2015
J03548+163	LP 413–108	Hyades	Crain et al. 1986
J03565+319	HAT 214–02089	Hyades?	Röser et al. 2011
J04206+272	XEST 16–045	Taurus	Scelsi et al. 2007
J04238+092	LP 535–073	Hyades	Weis et al. 1979
J04238+149	IN Tau	Hyades	van Rhijn & Raimond 1934
J04252+172	V805 Tau	Hyades	van Altena 1966
J04369-162	2MASS J04365738–1613065	Tuc-Hor	Malo et al. 2014
J04414+132	TYC 694–1183–1	Hyades	Johnson et al. 1962
J0443+0002 ^a	2MUCD 10320	β Pictoris	Alonso-Floriano et al. 2015a
J04433+296	Haro 6-36	Taurus	Haro et al. 1953
J04595+017	V1005 Ori	β Pictoris	Alonso-Floriano et al. 2015a
J05019+011	1RXS J050156.7+010845	β Pictoris	Alonso-Floriano et al. 2015a
J05084-210	2MASS J05082729–2101444	β Pictoris	Alonso-Floriano et al. 2015a
J0608-2753 ^a	2MASS 06085283-2753583	β Pictoris	Alonso-Floriano et al. 2015a
J07310+460	1RXS J073101.9+460030	Columba	Malo et al. 2013
J07446+035	YZ CMi	β Pictoris	Alonso-Floriano et al. 2015a
J09449-123	G 161-071	Argus	Bartlett et al. 2017
J11519+075	RX J1151.9+0731	β Pictoris	Alonso-Floriano et al. 2015a
J12508-213	DENIS J125052.6–212113	Pleiades?	Clarke et al. 2010
J14200+390	IZ Boo	Young?	Mochnecki et al. 2002
J14259+142	StKM 1–1155	β Pictoris	Alonso-Floriano et al. 2015a
J15079+762	HD 135363 B	IC 2391	Montes et al. 2001; Lépine & Bongiorno 2007
J15166+391	LP 222–065	Young disc	Jeffers et al. 2018
J1552+2948 ^a	2MASS J15525906+2948485	~100 Ma	Cruz et al. 2009
J15597+440	RX J1559.7+4403	AB Dor	Binks & Jeffries 2016
J16102-193	K2–33	USco	Preibisch et al. 2001
J17572+707	LP 044–162	Argus?	Gagné et al. 2015
J21100-193	BPS CS 22898-0065	β Pictoris	Alonso-Floriano et al. 2015a
J22088+117	2MASS J22085034+1144131	β Pictoris	Shkolnik et al. 2017
J23228+787	NLTT 56725	Columba	Makarov et al. 2007; Montes et al. 2018
J23301-026	2MASS J23301129–0237227	β Pictoris	Alonso-Floriano et al. 2015a
J23317-027	AF Psc	β Pictoris	Alonso-Floriano et al. 2015a

Notes. ^(a) Ultra-cool dwarfs from Smart et al. (2017) not in the CARMENES catalogue of M dwarfs.

Doradus, Hyades), and a miscellanea classification including one star of about 100 Ma (Cruz et al. 2009), an active one that kinematically belongs to the young Galactic disc (Jeffers et al. 2018), and an ultra-fast-rotating, H α -variable, X-ray-emitting, young star candidate (IZ Boo – Stephenson 1986; Fleming 1998; Mochnecki et al. 2002; Jeffers et al. 2018). The 36 stars and their respective references are listed in Table 4. As expected, these sources are also overluminous in the Hertzsprung-Russell diagram. Besides, there are a dozen stars neither tabulated by us nor classified as young star candidates in the literature that are also overluminous, which will deserve attention in forthcoming works.

3.3. Diagrams

We present and discuss several diagrams involving colours, absolute magnitudes, and bolometric corrections.

3.3.1. Colour-spectral type

We computed 20 average colour indices for adjacent filters and their standard deviation for late-K to late-L dwarfs, using only the good quality photometric data. We list them in Table A.2. The size of the sample for each colour index and spectral type is shown in parentheses. Colour indices computed from samples with less than four elements are included for completeness, albeit with a word of caution. As expected, the amount of data available in the ultraviolet and optical blue passbands decreases for later spectral types (see again Fig. 5). In particular, for spectral types M4 V and earlier we have all possible colour combinations, and for spectral types later than M4 V and up to L5 we have all possible colour combinations only between *G* and *W3*. This colour compilation complements, and most of the time supersedes, previous determinations (Bessell et al. 1998; Dahn et al. 2002; Hawley et al. 2002; Knapp et al. 2004; West et al. 2005; Covey et al. 2007; Zhang et al. 2009; Bochanski et al. 2010; Lépine et al. 2013; Pecalet & Mamajek 2013; Rajpurohit et al.

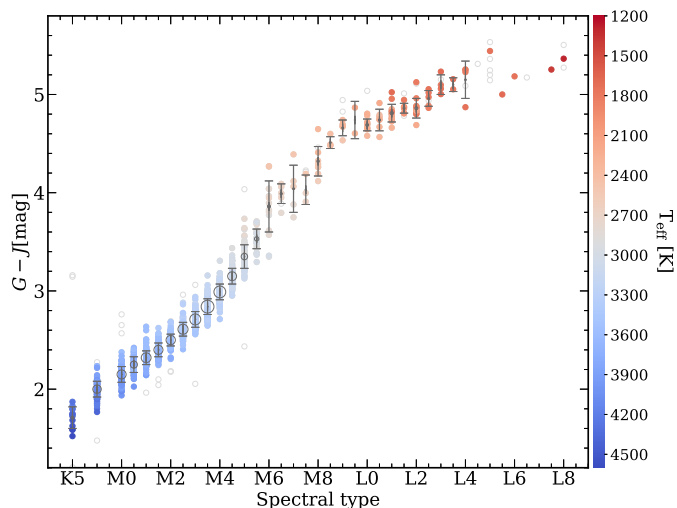


Fig. 13. $G - J$ colour against spectral type. Black empty circles mark the average colour for each spectral type with a size proportional to the number of stars and vertical bars account for their standard deviation in spectral types with more than one valid colour value. Empty grey circles depict bad photometric data, as explained in Sect. 2.2, and their values are not considered in the calculations of the average colours.

2013; Davenport et al. 2014; Filippazzo et al. 2015; Mann et al. 2015; Best et al. 2017).

From all the possible combinations, the *Gaia* DR2-2MASS colour $G - J$ provides one of the most solid estimators of spectral type from late-K to mid-L dwarfs. This is illustrated in Fig. 13. Firstly, $G - J$ covers a wide range in colour of about 3.6 mag between K5 V and L8, with a slight flattening restricted to the late L objects. Secondly, it exhibits one of the smallest dispersions in late-M and L dwarfs among all analysed colours, with a median deviation of 0.08 mag. Thirdly, the G and J passbands offer a high availability in this spectral type range, with 97.7% and 100% completeness in G and J , respectively. Also, faint objects benefit from the reliability of 2MASS and *Gaia* DR2 photometry. This colour index is superior to previous colour indices used to discriminate late spectral types, such as $i' - J$ (Reid et al. 2001; Hawley et al. 2002; West et al. 2005; Covey et al. 2008), and finds a compromise between completeness, photometric data quality (*Gaia* and 2MASS), scatter of the data, and colour interval spanned by the sequence. On the contrary, the use of *Gaia*-only and 2MASS-only colours for spectral typing presents some serious caveats, from the degeneracy of $G_{BP} - G_{RP}$ for spectral types M8 V and later, to the narrow interval of 1 mag of $G - G_{RP}$ from late-K to late-M dwarfs and its pronounced flattening from late-M to mid-L dwarfs, to the blueing of $J - H$ in the M-dwarf domain.

In Fig. A.1, we plot six additional colour-spectral type diagrams that show the behaviour of other passbands from the near-ultraviolet to mid-infrared, and their adequacy for spectral type estimation. In all cases, data with poor photometric quality are included as empty grey circles, but not considered for any calculation. Firstly, the optical-mid-infrared $G - W3$ colour serves as a useful complement for the $G - J$ colour, especially in the late-M and early-L regime. The $G - W3$ colour also exhibits a monotononic, low-scatter, steady increase from K5 V to L8, although the median of the dispersion is 0.17 mag, twice the value obtained with the $G - J$ index. Additionally, it benefits from the widest interval in colour of all the diagrams, with approximately 7 mag separating K5 V and L8.

The purely optical colour $r' - i'$, extensively used in the literature, can help to determine spectral types of late-K to late-M dwarfs, but it fails to discriminate the types for cooler objects. It peaks at about 2.8 mag (around M7–8 V), and becomes bluer beyond this point, as shown by for example Hawley et al. (2002) and Liebert & Gizis (2006).

The purely infrared colour $J - W2$ exhibits a remarkably low dispersion from M0 V to M8 V (less than 0.06 mag), but it covers a colour interval of only 0.5 mag. The colour $G_{RP} - W1$ offers an adequate alternative, with a dispersion slightly larger in the same range (0.09 mag), but spanning five times the colour interval. Furthermore, colours including the $W4$ passband suffer from poor quality data for spectral types M8 V and later.

The $NUV - G_{RP}$ colour is sensitive to both spectral type and ultraviolet flux excesses, which may be caused by chromospheric activity and/or interaction between close binaries. The first case includes “regular” stars later than M3–4 V at the boundary of stellar full convection. The second case comprises, according to Ansdell et al. (2015), young stars (including all our over-luminous young stars except one Hyades member) and unidentified binaries, which include unresolved background ultraviolet sources, unresolved old binaries with white dwarf companions, and short-period ($P < 10$ d) tidally interacting binaries that induce ongoing activity on each other. These phenomena give rise to a distinguishable population appended to the main sequence.

Finally, the optical $B - V$ colour became a commonly used index in the literature, including Bessell et al. (1998), Ramírez & Meléndez (2005), Casagrande et al. (2008), Smith (2018), Sun et al. (2018), del Burgo & Allende Prieto (2018), or Cochrane & Smith (2019), just to name a few. However, the $B - V$ colour has some disadvantages in the M-dwarf domain:

- Both B and V lack the completeness in the optical range that other passbands, such as G_{BP} , r' , i' , or G_{RP} , deliver.
- $B - V$ fails to produce a photometric sample statistically that is consistent beyond M5 V, while the *Gaia* DR2, 2MASS, or AllWISE passbands succeed.
- $B - V$ does not correlate with spectral type beyond M5 V.
- The width of the colour interval from late K to mid M is 1 mag, only a few times the scatter of the main sequence (0.12 mag), with a striking flattening between M0 V and M3 V.
- The mean uncertainties of B and V in our sample are 0.056 mag and 0.048 mag, respectively. For comparison, the same parameters for G and J are 0.0012 mag and 0.029 mag, respectively.

Therefore, we discourage the use of $B - V$ as an estimator of spectral type for stars cooler than K5 V. This is especially applicable when the *Gaia* DR2 (and 2MASS or AllWISE) magnitudes are available. The same reasoning above also applies to the B_T and V_T Tycho-2 passbands, which are even less complete.

3.3.2. Colour-colour

As in the colour-spectral type diagrams, main sequence stars occupy a well-defined locus in colour-colour diagrams. In spite of the degeneracy beyond M8 V, the narrowest main sequence is observed in the 2MASS-*Gaia* $G_{BP} - G_{RP}$ versus $G - J$ colour-colour diagram shown in the top panel of Fig. 14. Outliers in the diagram are mostly unresolved binaries and young stars for colours bluer than $G - J \sim 4.5$ mag (spectral types earlier than M8 V), albeit other possibilities also exist. For example, G 78–3 (J02455+449), at 57.8 pc (Gaia Collaboration et al. 2018b), is an M5 V star (Hawley et al. 1996), which exhibits a

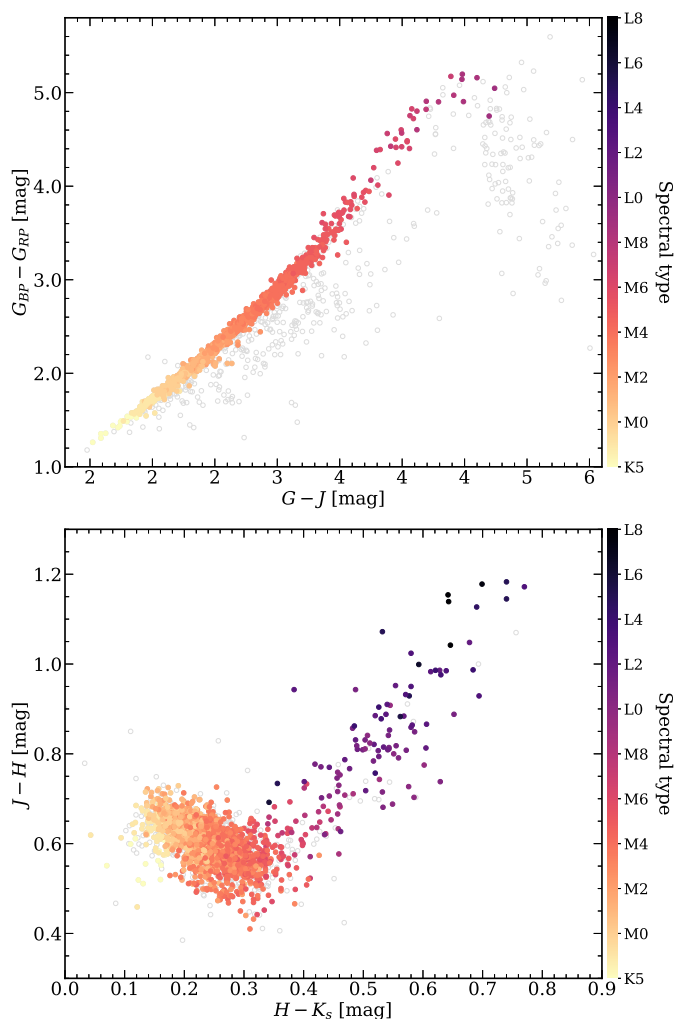


Fig. 14. Colour-colour diagrams representing $G_{BP} - G_{RP}$ vs. $G - J$ (top panel) and $J - H$ vs. $H - K_s$ (bottom panel). In both panels, empty grey circles represent stars with poor photometric quality data in any of the involved passbands, close binaries, or young stars. The remaining “regular” stars are colour-coded by spectral type.

$G - J$ colour typical of an early-M dwarf. For colours redder than $G - J \sim 4.5$ mag, we confirm the findings of [Smart et al. \(2019\)](#), who reported an unreliability in *Gaia* blue-band photometry of very late objects with $G_{BP} > 19.5$ mag due to background underestimation by the *Gaia* automatic pipeline ([Gaia Collaboration et al. 2018a](#); [Evans et al. 2018](#); [Smart et al. 2019](#)). As a comparison, in Fig. 14 we also show a widely used, 2MASS-only, colour-colour diagram ([Kirkpatrick et al. 1999](#); [Knapp et al. 2004](#); [Lépine & Shara 2005](#); [Hewett et al. 2006](#); [Covey et al. 2007](#)). There, late-K to late-M dwarfs occupy a compact region that ranges from $H - K_s \sim 0.15$ mag, $J - H \sim 0.65$ mag to $H - K_s \sim 0.30$ mag, $J - H \sim 0.55$ mag, while later stars and brown dwarfs become redder ([Kirkpatrick et al. 1999](#), and references above). We did not notice any near-infrared flux excess, as found in young T Tauri M-type stars and brown dwarfs with warm circumstellar discs ([Carpenter 2001](#); [Caballero et al. 2004](#); [Hernández et al. 2008](#)).

In Fig. A.2 we display a selection of six additional colour-colour diagrams. In all cases we plot far-ultraviolet to mid infrared-colours against $G - J$. Apart from the stars with poor photometric quality, we also discarded the 2MASS magnitudes of the extraordinarily red 2MUCD 20171 (J03552+113;

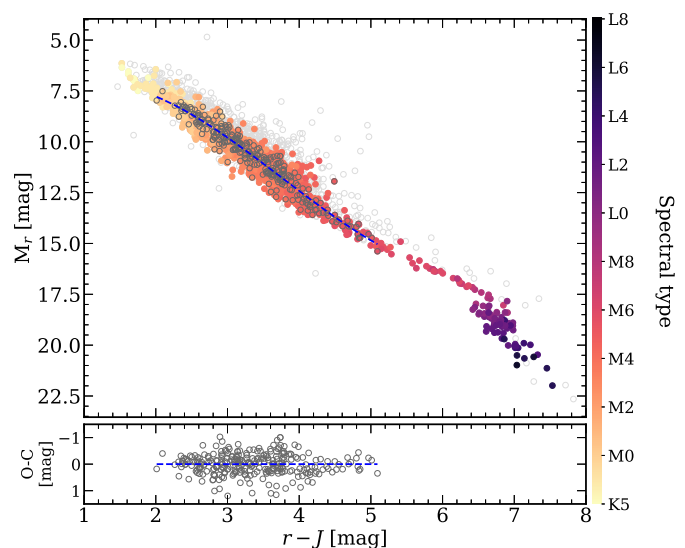


Fig. 15. Same as Fig. 12 but for M_r vs. $r' - J$. The GTO stars in the sample are shown in dark grey. The blue dashed line represents the polynomial fit given in Table 5. The fit residuals are shown in the small bottom panel.

[Faherty et al. 2013](#)) and blue SDSS J141624.08+134826.7 (J1416+1348A; [Burgasser et al. 2010](#)) ultracool dwarfs, which were clear outliers in many colour-colour diagrams involving 2MASS magnitudes. As in the colour-spectral type diagrams, the two colour-colour diagrams involving the bluest colours illustrate the two populations of ultraviolet active and inactive sources ($NUV - G_{RP}$) and the poor spectral sequence based on $B - V$ colour. The two diagrams involving UCAC4/SDSS9/APASS9/CMC15/PS1 DR1 $g'r'i'$ passbands, which will also be used at the Vera C. Rubin Observatory for the Legacy Survey of Space and Time (LSST), show a slightly larger spread than *Gaia* data and the double slope of the $r' - i'$ colour also found by [Hawley et al. \(2002\)](#) and [Liebert & Gizis \(2006\)](#). Interestingly, $g' - i'$ has a smaller dispersion in the late K and M dwarf domain than $r' - i'$, but a much larger dispersion at $G - J \gtrsim 4.5$ mag. This extra scatter at the reddest colours is more likely due to the intrinsic spectral variations at the M/L boundary (à la [Hawley et al. 2002](#); e.g. metallicity) than due to data analysis systematics or Poissonian error at the survey magnitude limits (à la [Smart et al. 2019](#); e.g. background). Finally, the colour-colour diagrams with near-infrared 2MASS and AllWISE data (specially W3 and W4) are very sensitive to T_{eff} variations at the L spectral types, but quite insensitive in the late-K and M dwarf domain. However, their sensitivity to metallicity must be investigated in detail with, for example, resolved photometry of M-dwarf wide common proper motion companions to FGK-type stars with well-determined stellar astrophysical parameters ([Montes et al. 2018](#); [Espada 2019](#)).

3.3.3. Absolute magnitude-colour

In Fig. 12 we show the M_G versus $G - J$ diagram. In Fig. 15 we show a similar diagram (see more examples in e.g. [Dupuy & Liu 2012](#)), but for r' instead of G , and we overplot a quadratic polynomial fit to 278 CARMENES GTO target stars with spectral types ranging from K7V to M9V ([Reiners et al. 2018b](#)). All of them have well-behaved *Gaia* astrometric solutions (i.e. $\text{RUWE} < 1.41$; Fig. 7) and do not have close companions ([Cortés-Contreras et al. 2017](#); [Baroch et al. 2018](#)), extreme val-

Table 5. Fit parameters for the empirical relations^a.

Y (mag)	X (mag)	a (mag)	b (mag ⁻¹)	c (mag ⁻²)	d (mag ⁻³)	e (mag ⁻⁴)	R^2	ΔX (mag)
M_r	$r' - J$	$+8.38 \pm 2.68$	-2.74 ± 2.36	$+1.47 \pm 0.68$	-0.132 ± 0.063	0	0.9398	[2.0, 5.1]
M_G	$G - J$	$+16.24 \pm 4.57$	-13.04 ± 4.80	$+5.64 \pm 1.66$	-0.622 ± 0.188	0	0.9308	[2.0, 4.0]
	(mag)	(mag)	(mag ⁻¹)	(mag ⁻²)	(mag ⁻³)	(mag ⁻⁴)		(mag)
$\log L/L_\odot$	M_J	$+2.051 \pm 0.075$	-0.662 ± 0.030	$+0.0267 \pm 0.0039$	-0.00102 ± 0.00016	0	0.9923	[4.4, 11.2]
		-3.906 ± 0.998	$+0.334 \pm 0.156$	-0.0263 ± 0.0061	0	0	0.9477	[11.2, 14.8]
$\log L/L_\odot$	M_G	$+0.145 \pm 0.201$	$+0.074 \pm 0.060$	-0.0382 ± 0.0060	$+0.00119 \pm 0.00019$	0	0.9901	[6.4, 14.0]
		-2.329 ± 0.687	$+0.092 \pm 0.084$	-0.0103 ± 0.0025	0	0	0.9782	[14.0, 20.2]
	(mag)	(mag)	(mag ⁻¹)	(mag ⁻²)	(mag ⁻³)	(mag ⁻⁴)		(mag)
BC_G	$G - J$	$+0.404 \pm 0.187$	$+0.161 \pm 0.239$	-0.465 ± 0.112	$+0.1159 \pm 0.0225$	-0.0115 ± 0.0017	0.9960	(1.5, 5.4]
BC_r	$r' - J$	$+0.557 \pm 0.085$	-0.036 ± 0.091	-0.318 ± 0.035	$+0.0552 \pm 0.0056$	-0.0037 ± 0.0003	0.9983	(1.5, 7.5]
BC_J	$G - J$	$+0.576 \pm 0.094$	$+0.735 \pm 0.104$	-0.132 ± 0.038	$+0.0115 \pm 0.0045$	0	0.9547	(0.5, 4.0]
BC_{W2}	$G - J$	-2.592 ± 0.667	$+5.845 \pm 1.005$	-2.611 ± 0.559	$+0.586 \pm 0.136$	-0.0496 ± 0.0122	0.9727	(1.5, 4.0]

Notes. ^(a) In all cases, the polynomial fits follow the form $Y = a + bX + cX^2 + dX^3 + eX^4$ and are applicable in the range ΔX . In all cases, R^2 is the correlation coefficient from the Pearson product-moment matrix. These relations should be applied to solar-metallicity stars only (Sect. 4). More significant figures are available at GitHub (Sect. 5).

ues of metallicity (Alonso-Floriano et al. 2015b; Passegger et al. 2018, 2019, 2020), young ages (Tal-Or et al. 2018), or large-amplitude photometric variability (Díez Alonso et al. 2019). We also fitted another quadratic polynomial to the M_G versus $G - J$ data of the GTO stars. Thus, with the parameter fits in Table 5 and only r' or G and J magnitudes, one can estimate a stellar distance with a median accuracy of 36 % for stars in the colour ranges listed in the column ΔX . From our knowledge of the CARMENES GTO stars, the most important contributor to the fit uncertainty is not the parallax or magnitude error, stellar variability, or unresolved multiplicity, but the intrinsic scatter of the M-dwarf colour sequence due to different metallicity.

The M_G versus $G - J$ relation is particularly helpful because, although there are about 420 million sources with known *Gaia* DR2 and 2MASS magnitudes (Marrese et al. 2019), there are several million near-infrared sources that lack a parallax determination. However, for the 31 single stars in our sample without published trigonometric parallaxes, we estimated photometric distances homogeneously from the M_r versus $r' - J$ relation assuming null extinction. Because of the relatively large uncertainty in the estimates, we did not use these photometric distances throughout our work, but only tabulated them in the online summary table described below. In general, we only recommend the use of these relations for estimating photometric distances for stars with solar-like metallicity, as well as good photometric quality (e.g. Bochanski et al. 2007, and see Sect. 4).

3.4. Absolute magnitudes and bolometric corrections

The absolute magnitude of a star is directly related to its bolometric luminosity. In our sample, we found that the J -band absolute magnitude, M_J , provides the correlation with VOSA luminosity that is most complete and that has the smallest scatter. Figure 16 shows L_{VOSA} (in solar units) versus M_J fitted in the late-K- to late-M- and L-dwarf domains, with three-degree and two-degree polynomials, respectively. Although in Table A.2 we list the fit parameters for both luminosities from 2MASS J and *Gaia* G , we preferred J over G because the larger effective width of the broad *Gaia* passband introduces more dispersion in the data, quantified by R^2 . With these relationships in the M-dwarf

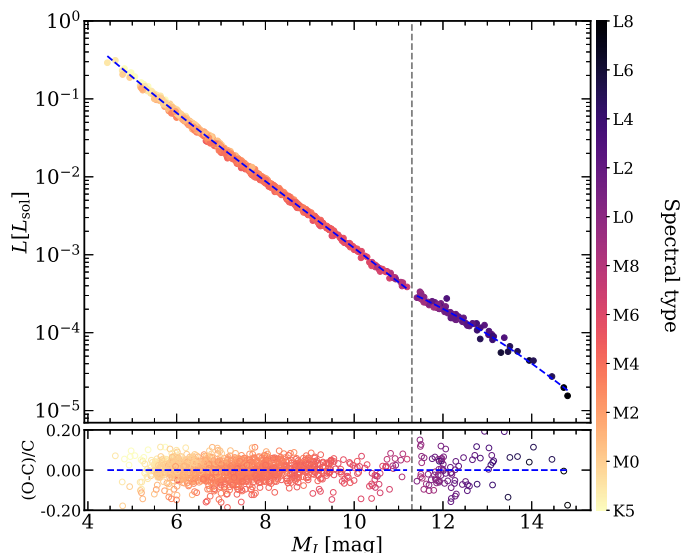


Fig. 16. Same as Fig. 12, but for L_{VOSA} vs. M_J and normalised fit residuals in the small bottom panel. The vertical dashed line separates the three-degree (late-K and M dwarfs) and two-degree (L dwarfs) fit ranges.

domain, it is possible to estimate bolometric luminosities from absolute magnitudes M_J and M_G with a relative precision of 4.2 % and 4.5 %, respectively.

We calculated bolometric corrections, $BC_\lambda = M_{\text{bol}} - M_\lambda$, for each investigated passband and plot them in Fig. 17. For the calculation, we followed the sign criterion of Böhm-Vitense et al. (1989) and the definition of the absolute bolometric magnitude M_{bol} by IAU Resolution B2 (Mamajek et al. 2015), which is independent of the solar luminosity,

$$M_{\text{bol}} = -2.5 \log_{10} \frac{L_\star}{L_0} = -2.5 \log_{10} L_\star + M_{\text{bol},0}, \quad (1)$$

where L_\star and L_0 are the luminosity of the star and the zero point of the absolute bolometric magnitude scale, respectively, and $M_{\text{bol},0} \equiv 71.197425$ mag.

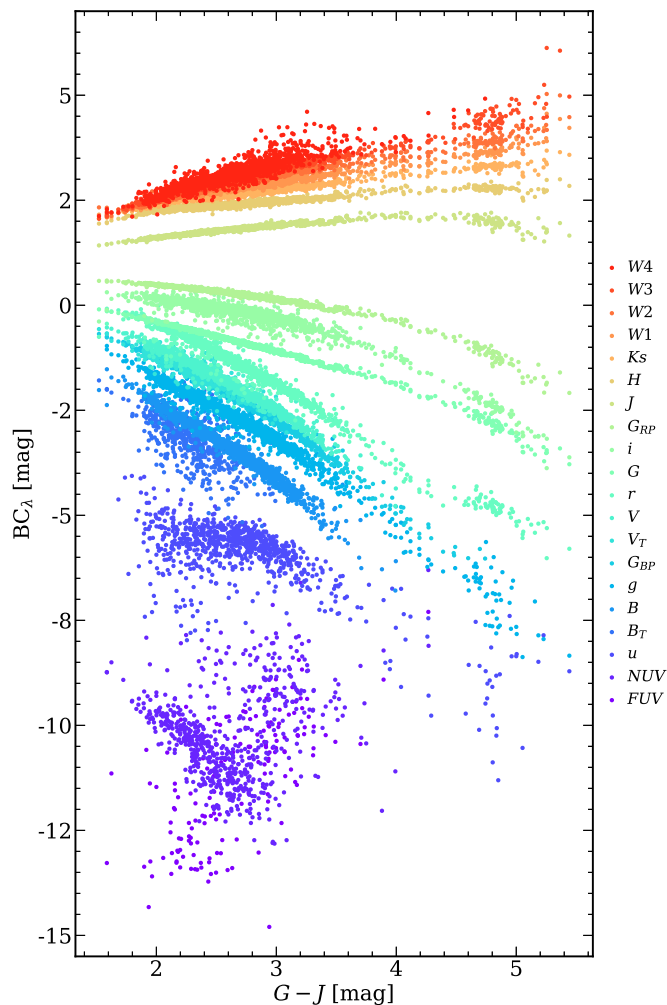


Fig. 17. Bolometric corrections for every star and passband vs. $G - J$ colour. The coloured sets contain all stars with available photometry in G , J , and the respective passband.

From the sample of 2479 stars, for the following analysis we discarded: (i) stars with poor photometric or astrometric behaviour based on quality indicators (Sects. 2.2 and 2.3), (ii) close binaries and stars with photometry contaminated by bright nearby companions ($\rho < 5$ arcsec; Sect. 2.4), (iii) over-luminous objects known to belong to young associations and moving groups (Sect. 3.2), and (iv) stars with extraordinarily anomalous colours or absolute magnitudes.

Of the different BC_λ versus $G - J$ combinations in Fig. 17, the narrowest sequence is that of BC_G . However, as illustrated by Fig. 18, the $BC_{r'}$ versus $r' - J$ sequence is even less scattered and spans wider ranges in X ($[1.5, 7.5]$ mag in $r' - J$ versus $[1.5, 5.4]$ mag in $G - J$) and Y ($[-5.8, 0.0]$ mag in $BC_{r'}$ versus $[-3.8, -0.1]$ mag in BC_G), probably due again to the broad G effective width. We fitted polynomials to the relations BC_G versus $G - J$, $BC_{r'}$ versus $r' - J$, BC_J versus $G - J$, and BC_{W2} versus $G - J$, and provide the corresponding parameters and correlation coefficients in Table 5. All in all, these relationships are complementary and can help to estimate relatively precise luminosities of M dwarfs with only a handful of widely available data (G and ϖ from *Gaia*, J from 2MASS, r' from a number of surveys including the forthcoming LSST).

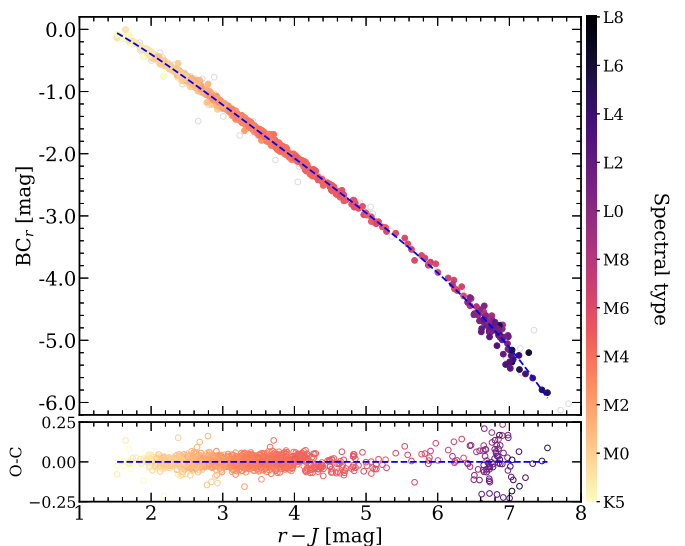


Fig. 18. Same as Fig. 12 but for $BC_{r'}$ vs. $r' - J$. A polynomial fit is shown as a blue dashed line.

3.5. Masses and radii

Finally, we derived radii \mathcal{R} and masses \mathcal{M} of the well-behaved stars. For \mathcal{R} , we used the Stefan-Boltzmann law $L = 4\pi\mathcal{R}^2\sigma T_{\text{eff}}^4$ and L and T_{eff} from VOSA. For \mathcal{M} we used the \mathcal{M} - \mathcal{R} relation in Eq. 6 of Schweitzer et al. (2019), which came from a compilation of detached, double-lined, double-eclipsing, main-sequence, M-dwarf binaries from the literature⁸. This relation is applicable in a wide range of metallicities for M dwarfs older than a few hundred million years. VOSA also computes two stellar radii, one from a model dependent dilution factor and d , the other using the Stefan-Boltzmann law, but we did not use them.

4. Discussion

Here we compare our L , T_{eff} , \mathcal{R} , \mathcal{M} , and photometric data with those in the literature. Tables 6 and 7 and Figs. 19 to 26 illustrate the discussion. In particular, in Table 6 we show average values of BC_G , BC_J , L , T_{eff} , \mathcal{M} , and \mathcal{R} for single, main-sequence stars with spectral types from K5 V to L2.0. The last column, N , indicates the number per spectral type bin of well-behaved stars (i.e. with no companions at $\rho < 5$ arcsec, no over-luminosity due to extreme youth, and of good *Gaia* DR2 astrometric and photometric quality). After applying a 2.5σ clipping, we calculated three-point rolling medians and standard deviations between M0.0 V and L2.0 (e.g. tabulated values for M4.0 V stars are the median and standard deviation of all individual BC_G values of stars with spectral types M3.5, M4.0, and M4.5 V), and simple medians and standard deviations for K5 V and K7 V stars. With these rolling medians, we conservatively smoothed potential inter-type variability due to the small number of stars per bin at the latest spectral types and the typical uncertainty in M-dwarf spectral type determination, of 0.5 dex (Hawley et al. 2002; Lépine et al. 2013; Alonso-Floriano et al. 2015b). The correspondingly large standard deviations denote the large natural scatter of the main sequence at the earliest spectral types and the difficulty in determining precise parameters at the latest ones. The boundary values for K5 V type were not smoothed and, therefore, must be handled with care. On the other

⁸ $\mathcal{M} = \alpha + \beta\mathcal{R}$, with $\alpha = -0.0240 \pm 0.0076 M_\odot$, $\beta = 1.055 \pm 0.017 M_\odot/R_\odot$, and \mathcal{M} and \mathcal{R} in solar units.

Table 6. Average astrophysical parameters for K5 V to L2.0 objects.

Spectral type	BC_G (mag)	BC_J (mag)	L ($10^{-4}L_\odot$)	T_{eff} (K)	\mathcal{R} (\mathcal{R}_\odot)	\mathcal{M} (\mathcal{M}_\odot)	N
K5 V	-0.206 ± 0.065	1.490 ± 0.047	1800 ± 420	4400 ± 180	0.693 ± 0.054	0.707 ± 0.057	13
K7 V	-0.393 ± 0.046	1.615 ± 0.027	960 ± 210	4050 ± 100	0.635 ± 0.046	0.646 ± 0.048	75
M0.0 V	-0.469 ± 0.082	1.654 ± 0.042	757 ± 230	3900 ± 140	0.613 ± 0.060	0.622 ± 0.063	104
M0.5 V	-0.570 ± 0.067	1.690 ± 0.038	585 ± 210	3800 ± 110	0.571 ± 0.076	0.578 ± 0.080	60
M1.0 V	-0.605 ± 0.054	1.719 ± 0.033	496 ± 150	3700 ± 85	0.550 ± 0.075	0.556 ± 0.079	112
M1.5 V	-0.664 ± 0.066	1.741 ± 0.037	409 ± 160	3600 ± 90	0.519 ± 0.082	0.524 ± 0.086	96
M2.0 V	-0.746 ± 0.077	1.769 ± 0.035	306 ± 130	3500 ± 105	0.473 ± 0.088	0.475 ± 0.093	99
M2.5 V	-0.825 ± 0.082	1.796 ± 0.034	228 ± 96	3400 ± 97	0.433 ± 0.086	0.432 ± 0.090	118
M3.0 V	-0.915 ± 0.085	1.827 ± 0.040	161 ± 74	3300 ± 87	0.389 ± 0.085	0.386 ± 0.090	144
M3.5 V	-0.985 ± 0.096	1.863 ± 0.043	111 ± 57	3300 ± 92	0.343 ± 0.082	0.338 ± 0.087	193
M4.0 V	-1.043 ± 0.093	1.890 ± 0.043	87 ± 47	3200 ± 88	0.309 ± 0.079	0.302 ± 0.083	170
M4.5 V	-1.160 ± 0.103	1.920 ± 0.041	50 ± 27	3100 ± 88	0.263 ± 0.069	0.253 ± 0.073	88
M5.0 V	-1.236 ± 0.122	1.951 ± 0.039	28 ± 13	3100 ± 58	0.207 ± 0.041	0.195 ± 0.043	52
M5.5 V	-1.420 ± 0.116	1.997 ± 0.057	20.1 ± 8.3	3000 ± 85	0.173 ± 0.032	0.159 ± 0.034	22
M6.0 V	-1.572 ± 0.178	2.062 ± 0.066	11.1 ± 3.9	2900 ± 108	0.138 ± 0.020	0.121 ± 0.021	14
M6.5 V	-1.837 ± 0.223	2.096 ± 0.065	7.2 ± 1.7	2750 ± 124	0.123 ± 0.011	0.106 ± 0.011	6
M7.0 V	-1.854 ± 0.129	2.105 ± 0.050	6.3 ± 1.1	2700 ± 94	0.119 ± 0.009	0.101 ± 0.010	4
M7.5 V	-2.169 ± 0.141	2.078 ± 0.044	5.8 ± 1.2	2500 ± 82	0.121 ± 0.008	0.104 ± 0.009	2
M8.0 V	-2.192 ± 0.163	2.082 ± 0.049	5.1 ± 1.6	2500 ± 91	0.121 ± 0.014	0.104 ± 0.014	7
M8.5 V	-2.342 ± 0.169	2.119 ± 0.052	3.4 ± 1.5	2400 ± 88	0.107 ± 0.015	0.088 ± 0.016	4
M9.0 V	-2.520 ± 0.158	2.137 ± 0.071	2.69 ± 0.35	2350 ± 86	0.096 ± 0.013	0.077 ± 0.014	5
M9.5 V	-2.627 ± 0.118	2.060 ± 0.073	2.35 ± 0.43	2300 ± 45	0.096 ± 0.007	0.077 ± 0.008	2
L0.0	-2.648 ± 0.102	2.031 ± 0.070	2.30 ± 0.43	2275 ± 59	0.097 ± 0.003	0.079 ± 0.004	12
L0.5	-2.746 ± 0.128	2.024 ± 0.081	2.17 ± 0.15	2250 ± 61	0.098 ± 0.004	0.079 ± 0.004	6
L1.0	-2.817 ± 0.123	1.974 ± 0.072	2.08 ± 0.26	2150 ± 165	0.101 ± 0.005	0.083 ± 0.006	15
L1.5	-2.868 ± 0.112	1.958 ± 0.070	1.81 ± 0.35	2000 ± 172	0.112 ± 0.015	0.094 ± 0.016	7
L2.0	-2.930 ± 0.101	1.951 ± 0.083	1.55 ± 0.24	1850 ± 92	0.116 ± 0.013	0.098 ± 0.014	14

hand, Table 7 complements Table A.2 and lists the average absolute magnitudes of K5 V to L2.0 objects in the 14 most representative bands (i.e. all except for *GALEX FUV* and *NUV*, SDSS9 u' , Tycho-2 B_T and V_T , and *WISE W4*). We applied the same rolling medians and 2.5σ clipping as in Table 6. For each spectral type K5–M7.0 V, a total of $6.227 \cdot 10^9$ different colours can be determined from the tabulated absolute magnitudes (e.g. $G - J = M_G - M_J$). For spectral types L0.0–2.0, the number of possible colours is 3 628 800.

Luminosities (Fig. 19). First, we compared our L computed with VOSA with those from a number of works in the literature (left panel – Golimowski et al. 2004; Vrba et al. 2004; Howard et al. 2010; Kundurthy et al. 2011; Bonfils et al. 2012; Mann et al. 2013; Gaidos & Mann 2014; Affer et al. 2016, 2019; Tuomi et al. 2014; Newton et al. 2015; Anglada-Escudé et al. 2016; Astudillo-Defru et al. 2017; Dittmann et al. 2017; Gillon et al. 2017; Maldonado et al. 2017; Suárez Mascareño et al. 2017a,b; Gaia Collaboration et al. 2018b; Hirano et al. 2018; Hobson et al. 2018). In spite of (or due to) the relatively large published L uncertainties of a few ultracool dwarfs, the agreement is in general excellent, especially in the case of Gaia Collaboration et al. (2018b). Our median L values per spectral type also match those of Pecaut & Mamajek (2013, right panel). When integrated from a well-calibrated, multi-band spectral energy distribution in a wide wavelength coverage and calculated with the latest *Gaia* parallaxes as in this work, L can become the most reliable “observable” of low-mass stars, instead of the widely used temperature, which

is inferred through colours, spectral classification, or expensive, model-dependent, spectral synthesis.

Effective temperatures (Fig. 20). Next, we compared our T_{eff} from VOSA with the values from the works referred to in the previous paragraph, except from Gaia Collaboration et al. (2018b), plus from Passegger et al. (2019), who in turn compared their T_{eff} with those from Rojas-Ayala et al. (2012), Gaidos & Mann (2014), Maldonado et al. (2015), Mann et al. (2015), Rajpurohit et al. (2018a), and Schweitzer et al. (2019). From the top left panel in Fig. 20, our T_{eff} are cooler than those of the literature by -86 ± 82 K. This systematic difference is within the grid step size of the theoretical models used by VOSA, of 100 K or 50 K, but appreciable in the whole $T_{\text{eff}} = 3000$ – 4000 K range. That VOSA does not interpolate between grid points may partly explain this systematic difference. In the empirical T_{eff} -spectral type relation shown in the top right panel, T_{eff} from Rajpurohit et al. (2018a) and Passegger et al. (2019) are, again, slightly warmer than ours in the late- and early-M domains, respectively. However, the agreement with the relation of Pecaut & Mamajek (2013) is exquisite. The K/M and M/L boundaries occur at about 3900 K and 2300 K, respectively, in line with the standard values (e.g. Habets & Heintze 1981; Kirkpatrick 2005, see also Table 6). In the Hertzsprung-Russell diagram in the bottom left panel, as expected, our targets are significantly less luminous than the very young stars and brown dwarfs of the same T_{eff} tabulated by Pecaut & Mamajek (2013) and Faherty et al. (2016), but our main sequence (excluding young targets) matches that of Newton et al. (2015). The

Table 7. Average absolute magnitudes for K5 V to L2.0 objects.

Spectral type	M_B (mag)	$M_{g'}$ (mag)	M_{GBP} (mag)	M_V (mag)	M_r (mag)	M_G (mag)	M_r (mag)
K5 V	8.33 ± 0.37	7.84 ± 0.35	7.32 ± 0.39	7.23 ± 0.28	6.92 ± 0.31	6.82 ± 0.35	6.52 ± 0.31
K7 V	9.65 ± 0.44	9.07 ± 0.40	8.51 ± 0.35	8.32 ± 0.38	7.75 ± 0.41	7.66 ± 0.30	7.11 ± 0.37
M0.0 V	10.11 ± 0.56	9.47 ± 0.50	8.93 ± 0.49	8.74 ± 0.49	8.14 ± 0.48	7.98 ± 0.41	7.42 ± 0.36
M0.5 V	10.57 ± 0.52	9.89 ± 0.49	9.36 ± 0.49	9.11 ± 0.48	8.59 ± 0.48	8.33 ± 0.41	7.72 ± 0.40
M1.0 V	10.90 ± 0.49	10.20 ± 0.45	9.70 ± 0.45	9.47 ± 0.47	8.87 ± 0.44	8.61 ± 0.39	7.92 ± 0.37
M1.5 V	11.24 ± 0.57	10.48 ± 0.53	9.99 ± 0.53	9.76 ± 0.52	9.15 ± 0.51	8.86 ± 0.45	8.17 ± 0.45
M2.0 V	11.72 ± 0.65	10.98 ± 0.61	10.47 ± 0.60	10.19 ± 0.58	9.63 ± 0.59	9.23 ± 0.53	8.55 ± 0.53
M2.5 V	12.19 ± 0.65	11.40 ± 0.63	10.97 ± 0.62	10.67 ± 0.62	10.10 ± 0.61	9.65 ± 0.54	8.94 ± 0.54
M3.0 V	12.77 ± 0.71	11.98 ± 0.66	11.52 ± 0.65	11.22 ± 0.66	10.67 ± 0.66	10.08 ± 0.57	9.38 ± 0.58
M3.5 V	13.28 ± 0.80	12.47 ± 0.78	12.01 ± 0.77	11.71 ± 0.75	11.16 ± 0.75	10.51 ± 0.67	9.79 ± 0.67
M4.0 V	13.75 ± 0.87	12.91 ± 0.84	12.47 ± 0.83	12.12 ± 0.81	11.61 ± 0.81	10.88 ± 0.72	10.13 ± 0.72
M4.5 V	14.39 ± 0.94	13.62 ± 0.90	13.15 ± 0.89	12.77 ± 0.87	12.26 ± 0.86	11.44 ± 0.77	10.67 ± 0.77
M5.0 V	15.30 ± 1.03	14.52 ± 1.05	14.10 ± 1.04	13.63 ± 1.00	13.15 ± 0.99	12.25 ± 0.81	11.42 ± 0.83
M5.5 V	16.45 ± 1.03	15.49 ± 0.98	15.04 ± 0.98	14.59 ± 0.89	14.05 ± 0.97	12.88 ± 0.55	12.09 ± 0.61
M6.0 V	17.21 ± 0.70	16.59 ± 0.99	16.07 ± 0.96	15.25 ± 0.39	15.14 ± 0.93	13.64 ± 0.64	12.86 ± 0.64
M6.5 V	18.65 ± 0.78	17.76 ± 0.91	17.40 ± 0.89	16.92 ± 0.81	16.36 ± 0.83	14.42 ± 0.58	13.73 ± 0.58
M7.0 V	18.92 ± 0.36	18.18 ± 0.40	17.66 ± 0.36	17.16 ± 0.23	16.76 ± 0.51	14.55 ± 0.22	14.05 ± 0.27
M7.5 V	...	18.62 ± 0.57	18.11 ± 0.54	...	17.07 ± 0.51	15.01 ± 0.39	14.33 ± 0.36
M8.0 V	...	18.96 ± 0.65	18.53 ± 0.81	...	17.41 ± 0.60	15.19 ± 0.51	14.50 ± 0.57
M8.5 V	...	19.28 ± 0.60	19.39 ± 0.69	...	17.72 ± 0.52	15.76 ± 0.55	15.07 ± 0.65
M9.0 V	...	20.11 ± 0.32	19.59 ± 0.32	...	18.11 ± 0.24	16.11 ± 0.25	15.67 ± 0.26
M9.5 V	...	20.23 ± 0.30	19.64 ± 0.25	...	18.41 ± 0.17	16.39 ± 0.20	15.83 ± 0.29
L0.0	...	20.26 ± 0.33	18.41 ± 0.23	16.51 ± 0.21	16.06 ± 0.22
L0.5	...	20.56 ± 0.68	18.61 ± 0.26	16.69 ± 0.24	16.28 ± 0.26
L1.0	...	21.13 ± 0.68	18.85 ± 0.19	16.80 ± 0.19	16.38 ± 0.21
L1.5	...	21.20 ± 0.55	18.94 ± 0.19	16.97 ± 0.25	16.54 ± 0.24
L2.0	...	21.17 ± 0.56	19.07 ± 0.17	17.15 ± 0.22	16.68 ± 0.20
Spectral type	M_{GRP} (mag)	M_J (mag)	M_H (mag)	M_{K_s} (mag)	M_{W1} (mag)	M_{W2} (mag)	M_{W3} (mag)
K5 V	6.06 ± 0.31	5.13 ± 0.26	4.55 ± 0.24	4.44 ± 0.22	4.33 ± 0.22	4.40 ± 0.32	4.33 ± 0.35
K7 V	6.78 ± 0.27	5.66 ± 0.31	5.02 ± 0.29	4.84 ± 0.28	4.76 ± 0.27	4.78 ± 0.30	4.72 ± 0.28
M0.0 V	7.07 ± 0.36	5.88 ± 0.30	5.22 ± 0.30	5.04 ± 0.28	4.93 ± 0.27	4.91 ± 0.22	4.88 ± 0.23
M0.5 V	7.36 ± 0.38	6.09 ± 0.32	5.44 ± 0.34	5.24 ± 0.32	5.11 ± 0.30	5.07 ± 0.27	5.03 ± 0.26
M1.0 V	7.59 ± 0.36	6.26 ± 0.33	5.63 ± 0.35	5.41 ± 0.33	5.26 ± 0.32	5.23 ± 0.28	5.18 ± 0.28
M1.5 V	7.83 ± 0.43	6.44 ± 0.40	5.81 ± 0.43	5.60 ± 0.42	5.46 ± 0.41	5.34 ± 0.33	5.32 ± 0.37
M2.0 V	8.16 ± 0.50	6.72 ± 0.45	6.10 ± 0.48	5.87 ± 0.46	5.73 ± 0.46	5.62 ± 0.41	5.57 ± 0.40
M2.5 V	8.54 ± 0.52	7.00 ± 0.48	6.41 ± 0.50	6.17 ± 0.49	6.03 ± 0.48	5.90 ± 0.45	5.82 ± 0.44
M3.0 V	8.94 ± 0.55	7.35 ± 0.50	6.77 ± 0.52	6.50 ± 0.51	6.33 ± 0.51	6.19 ± 0.48	6.11 ± 0.47
M3.5 V	9.33 ± 0.64	7.67 ± 0.60	7.10 ± 0.61	6.83 ± 0.60	6.66 ± 0.58	6.48 ± 0.56	6.39 ± 0.55
M4.0 V	9.68 ± 0.69	7.97 ± 0.64	7.40 ± 0.65	7.13 ± 0.64	6.95 ± 0.63	6.78 ± 0.61	6.65 ± 0.60
M4.5 V	10.19 ± 0.75	8.41 ± 0.67	7.81 ± 0.69	7.56 ± 0.67	7.36 ± 0.66	7.18 ± 0.64	7.04 ± 0.63
M5.0 V	10.98 ± 0.74	9.08 ± 0.59	8.53 ± 0.58	8.19 ± 0.56	7.99 ± 0.56	7.81 ± 0.55	7.63 ± 0.53
M5.5 V	11.53 ± 0.56	9.48 ± 0.48	8.88 ± 0.49	8.58 ± 0.47	8.37 ± 0.46	8.17 ± 0.45	8.02 ± 0.42
M6.0 V	12.10 ± 0.54	10.04 ± 0.42	9.47 ± 0.41	9.16 ± 0.40	8.88 ± 0.39	8.65 ± 0.40	8.56 ± 0.35
M6.5 V	12.92 ± 0.52	10.47 ± 0.19	9.85 ± 0.20	9.48 ± 0.19	9.25 ± 0.20	9.04 ± 0.24	8.80 ± 0.20
M7.0 V	13.06 ± 0.20	10.58 ± 0.13	9.97 ± 0.12	9.66 ± 0.18	9.42 ± 0.19	9.22 ± 0.17	9.01 ± 0.14
M7.5 V	13.46 ± 0.35	10.82 ± 0.23	10.16 ± 0.21	9.76 ± 0.19	9.55 ± 0.19	9.32 ± 0.18	9.06 ± 0.15
M8.0 V	13.62 ± 0.49	10.92 ± 0.34	10.25 ± 0.35	9.86 ± 0.32	9.60 ± 0.27	9.39 ± 0.24	9.10 ± 0.20
M8.5 V	14.18 ± 0.53	11.30 ± 0.37	10.62 ± 0.37	10.14 ± 0.35	9.85 ± 0.30	9.61 ± 0.26	9.25 ± 0.18
M9.0 V	14.51 ± 0.23	11.51 ± 0.03	10.91 ± 0.14	10.41 ± 0.24	10.06 ± 0.22	9.77 ± 0.19	9.38 ± 0.12
M9.5 V	14.72 ± 0.19	11.68 ± 0.17	10.99 ± 0.18	10.51 ± 0.19	10.19 ± 0.16	9.94 ± 0.14	9.39 ± 0.14
L0.0	14.88 ± 0.21	11.83 ± 0.18	11.07 ± 0.20	10.55 ± 0.21	10.25 ± 0.10	9.98 ± 0.13	9.41 ± 0.21
L0.5	15.07 ± 0.24	11.94 ± 0.12	11.14 ± 0.05	10.61 ± 0.06	10.28 ± 0.09	10.04 ± 0.14	9.51 ± 0.17
L1.0	15.18 ± 0.20	11.97 ± 0.15	11.14 ± 0.08	10.62 ± 0.09	10.32 ± 0.17	10.07 ± 0.17	9.60 ± 0.20
L1.5	15.32 ± 0.25	12.08 ± 0.19	11.30 ± 0.19	10.78 ± 0.19	10.44 ± 0.19	10.17 ± 0.19	9.68 ± 0.20
L2.0	15.51 ± 0.22	12.27 ± 0.24	11.47 ± 0.24	10.96 ± 0.22	10.63 ± 0.12	10.34 ± 0.12	9.77 ± 0.28

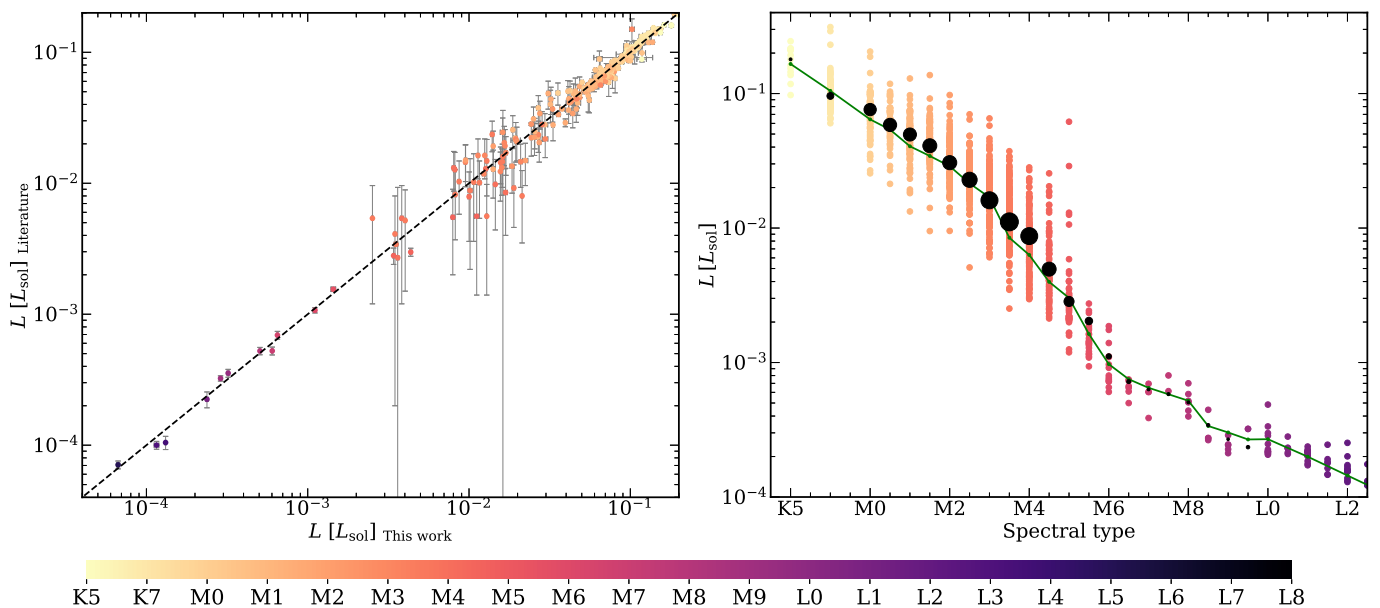


Fig. 19. Comparison of L from VOSA and from the literature (left) and individual (coloured points) and median L (black circles) as a function of spectral type as in Table 6 (right). In the right panel, the green line outlines the empirical L -spectral type sequence of Pecaut & Mamajek (2013, with updated values for M0.0 V to M9.5 V; E. E. Mamajek, priv. comm.) and the size of the black points is proportional to the number of stars per spectral type.

most convincing plot is perhaps the M_J versus T_{eff} diagram in the bottom right panel, where our M-dwarf main sequence perfectly overlaps with those defined by Lépine et al. (2013) and Gaidos & Mann (2014) and extrapolates reasonably well into the ultracool dwarf sequence of Dahn et al. (2002). The absolute magnitude in the vertical axis does not depend on models, Virtual Observatory tools, spectral synthesis, or multi-band photometry, but only on reliable 2MASS J -band magnitude and *Gaia* parallaxes.

Metallicity (Figs. 21 to 23). The role of metallicity in the empirical relations between physical parameters of M dwarfs has been the subject of investigation by many teams (e.g. Bonfils et al. 2005; Woolf & Wallerstein 2005; Casagrande et al. 2008; Rojas-Ayala et al. 2012; Boyajian et al. 2012; von Boetticher et al. 2019, see Sect. 4.3 in Alonso-Floriano et al. 2015a for a short review). Of them, Mann et al. (2015) showed that empirical relations such as absolute magnitude-radius, radius-temperature, or colour-temperature could benefit from incorporating an additional term that accounts for metallicity. However, mainly because of the limitations of the BT-Settl CIFIST grid of theoretical models stored in the VOSA database, in our work we computed L and T_{eff} assuming a solar metallicity ($[\text{Fe}/\text{H}] = 0$)⁹.

In order to quantify the impact of metallicity within our empirical relations in Table 5, first we compiled values of spectroscopically derived iron abundances of 510 single stars in our sample from Mann et al. (2015, 2019), Majewski et al. (2017), and Passegger et al. (2019). The compiled $[\text{Fe}/\text{H}]$ values ranged from -1.63 dex for the mid-M dwarf HD 285190 to $+0.59$ dex for the early-M dwarf LP 397-041, with a mean and dispersion of -0.04 ± 0.26 dex.

⁹ Actually, BT-Settl CIFIST models are defined for solar metal abundance, $[\text{M}/\text{H}]$, but here we used solar iron abundance, $[\text{Fe}/\text{H}]$, for simplicity.

Figure 21 displays the relations parametrised in Table 5, as well as the colour-spectral type diagram discussed in Sect. 3.3.1, colour-coded by the metallicity values from the literature. In either of the top plots (L vs. M_J and BC_G vs. $G-J$), the distribution of residuals did not show any correlation with the metal content of the stars. Both representations benefit from the fact that deriving L does not rely on precise $[\text{Fe}/\text{H}]$ measurements. In the bottom panels, the distribution of metallicity values in the $G-J$ versus spectral type diagram shows no significant dependence on metallicity. This lack of correlation is also apparent in the additional colour diagrams displayed in Appendix A. However, the M_G versus $G-J$ relation exhibits a notable correlation between metallicity and the residuals of the fit: more metallic stars appear brighter than less metallic stars of the same $G-J$ colour or, alternatively or simultaneously, more metallic stars appear redder than less metallic stars of the same M_G absolute magnitude. This dependence is most likely the main source of uncertainty for photometric distances, as we noted in Sect. 3.3.3. By using standard broad passbands in the red optical or the near infrared, such as r' or J , the effect of metallicity can be reduced compared to using wider, bluer passbands, such as G , which are more affected by the features that metallicity imprints on the spectra.

In the diagrams involving T_{eff} , Mann et al. (2015) pointed out that the effect of metallicity can be severely masked due to the steeper dependence on the temperature. This is an important point to underline because the uncertainties in T_{eff} of models are a major source of uncertainties in the final products of the SED fitting. In other words, the approximation of near-solar metallicity implies an error that is always within the errors due to temperature uncertainties. We argue that, with the exception of absolute magnitude against colours and extreme cases (i.e. very metal-poor stars), the models described in this work can be treated as independent of the metal content of the star.

As an additional test, we used VOSA to perform a new SED fit of the CARMENES GTO stars in the sample using the BT-Settl grid of spectra (“no CIFIST”; Allard et al. 2012), which allowed us to explore iron abundances different from $[\text{Fe}/\text{H}]$

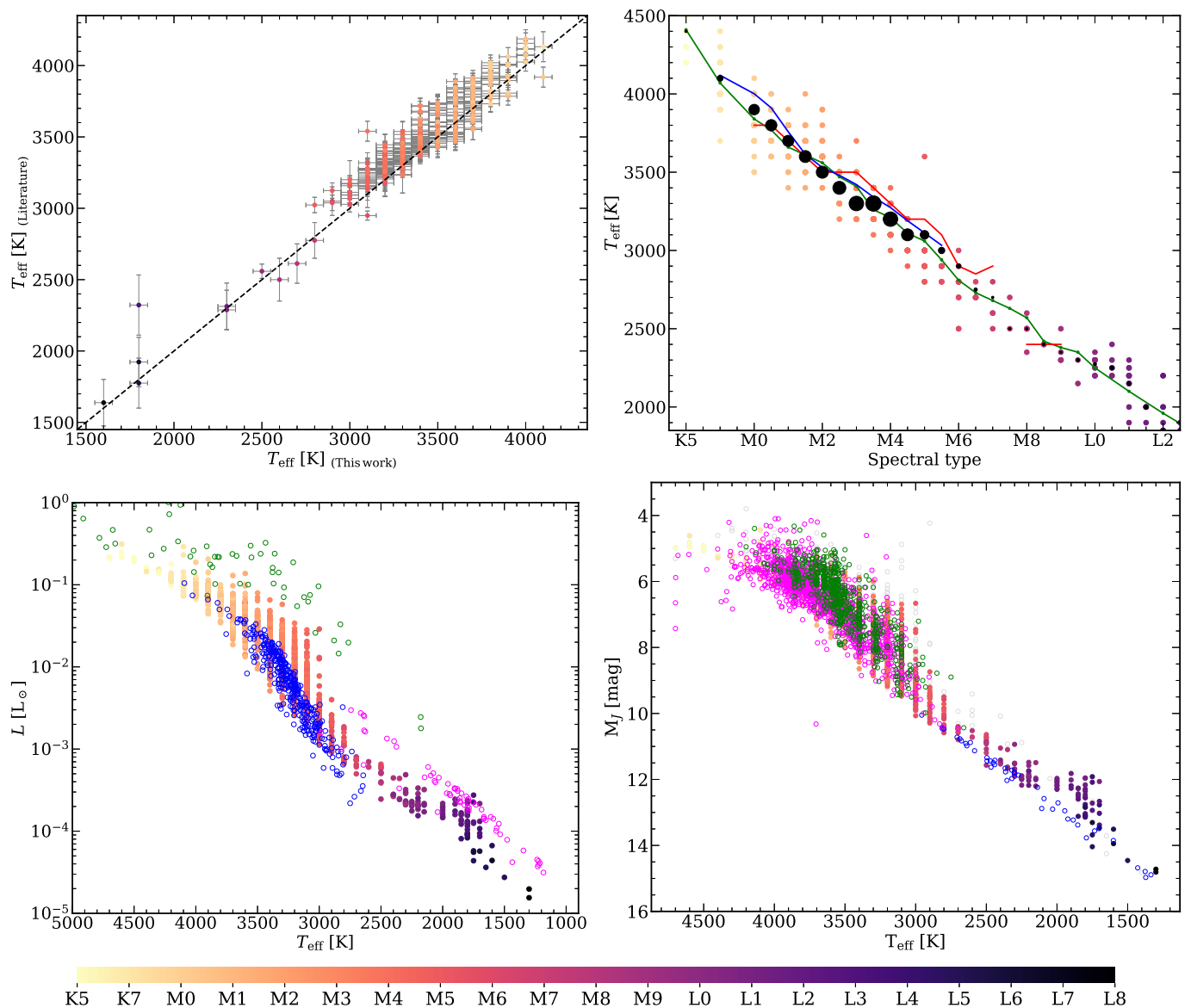


Fig. 20. Four representative diagrams involving T_{eff} . In the four panels our investigated stars are represented with filled circles colour-coded by spectral type. Top left: Comparison of T_{eff} from this work and from the literature. Top right: Individual (coloured points) and median (black circles) values of T_{eff} as a function of the spectral sequence shown in Table 6. The size of the black circles is proportional to the number of stars per spectral type. The green, red, and blue lines mark the mean values tabulated by Pecaut & Mamajek (2013), Rajpurohit et al. (2018a), and Passegger et al. (2019), respectively. Bottom left: L vs. T_{eff} . As a comparison we also plot pre-main sequence stars with BT-Settl model fitting from Pecaut & Mamajek (2013, green empty circles), M dwarfs in the MEarth sample with stellar parameters from Newton et al. (2015, blue empty circles), inferred from the pseudo-equivalent width of Mg I near-infrared lines), and high-confidence moving group members from Faherty et al. (2016, magenta empty circles) with parameters computed as in Filippazzo et al. (2015). Bottom right: J -band absolute magnitude vs. T_{eff} . As a comparison we also plot the samples of Dahn et al. (2002, blue open circles), Lépine et al. (2013, green open circles), and Gaidos & Mann (2014, magenta open circles).

= 0. In particular, we let $[\text{Fe}/\text{H}]$ vary between -1.5 dex and $+0.5$ dex, with a step size of 0.5 dex, and constrained T_{eff} and $\log g$ as in Table 3. The $[\text{Fe}/\text{H}]$ values derived from this new fit are compared to the spectroscopic values from the literature in Fig. 22. While the median of VOSA BT-Settl and published values are in fair agreement (-0.097 dex and $+0.033$ dex, respectively), the scatter of the VOSA $[\text{Fe}/\text{H}]$ values is much greater than that of the literature ($\sigma_{[\text{Fe}/\text{H}],\text{VOSA}} = 0.596$ dex and $\sigma_{[\text{Fe}/\text{H}],\text{literature}} = 0.216$ dex). From the diagram, VOSA assigned artificially low $[\text{Fe}/\text{H}]$ to stars with spectroscopically derived solar values, which reinforced our initial approach of setting $[\text{Fe}/\text{H}] = 0$. This is in line with the quality tests carried out by the VOSA

team in 2017, in which they compared VOSA metallicities with those derived by Yee et al. (2017), Lindgren & Heiter (2017), and Rajpurohit et al. (2018b). In particular, they concluded that “metallicities [...] provided by VOSA are not reliable due to the minor contribution of [this parameter] to the SED shape”¹⁰.

In Fig. 23 we compare the L and T_{eff} obtained for the GTO stars using BT-Settl CIFIST with $[\text{Fe}/\text{H}] = 0$ (used throughout this work) and BT-Settl with a free range in metallicity. While the derivation of bolometric luminosities in K dwarfs, with a normalised difference of $\Delta L/L = -0.0065 \pm 0.0046$, is marginally

¹⁰ <http://svo2.cab.inta-csic.es/theory/vosa/helpw4.php?otype=st>

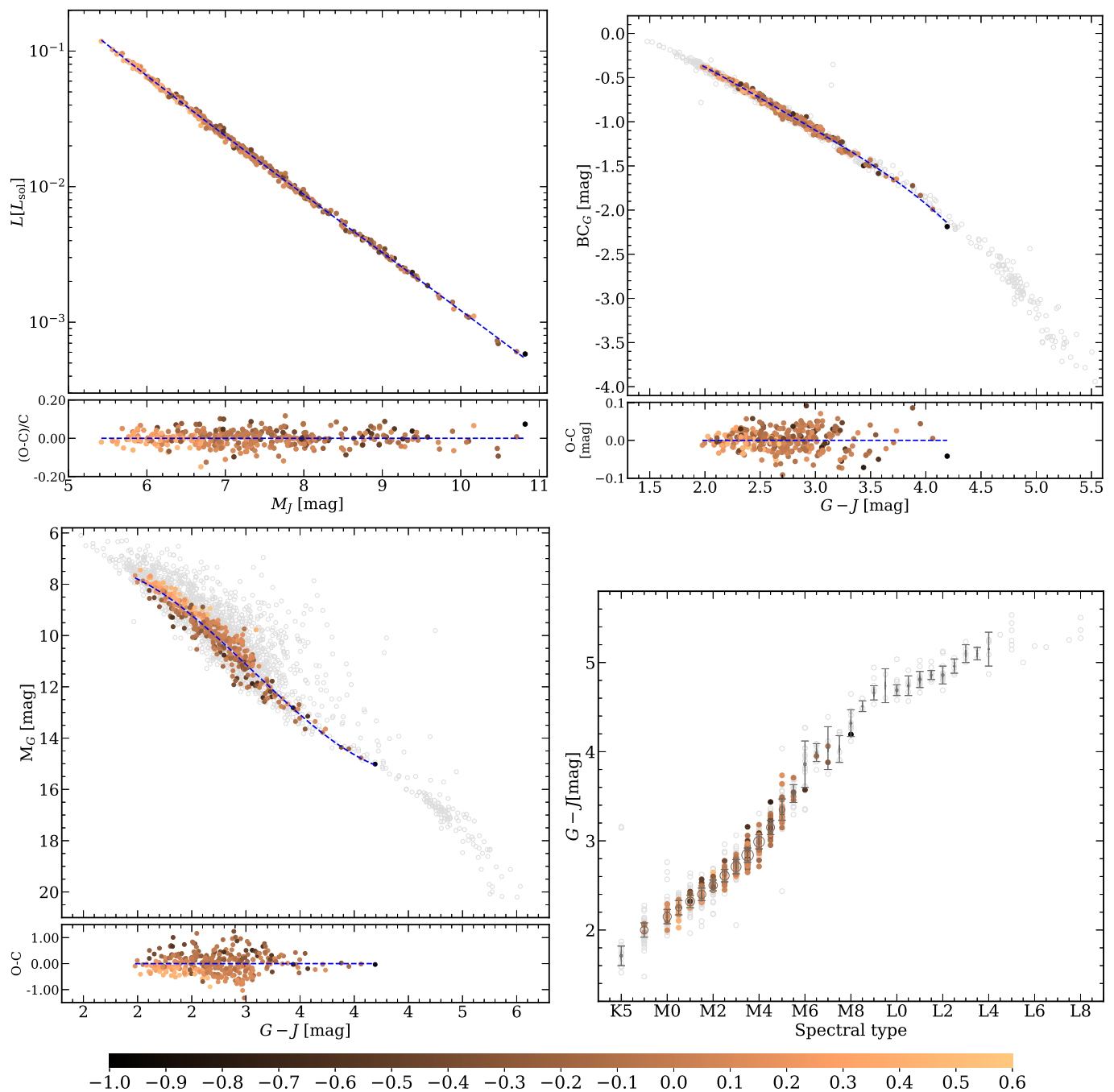


Fig. 21. Revisiting empirical relations in Table 5 for stars with $[\text{Fe}/\text{H}]$ values published in the literature. Top left: $L_{\text{VOSA,BT-Settl CIFIST}}$ vs. M_J . Top right: BC_G vs. $G - J$. Bottom left: M_G vs. $G - J$. The blue dashed lines in the three panels represent new 3-, 4-, and 3-degree polynomial fits, respectively. Bottom right: $G - J$ vs. spectral type. The grey circles represent the mean values with a symbol size proportional to the sample size in each type.

dependent on metallicity, the derivation in M dwarfs is independent: the normalised differences between L computed with the two methods is $\Delta L/L = 0.012 \pm 0.035$, consistent with zero. The T_{eff} difference is also consistent with zero, and its standard deviation is 101 K, identical to the T_{eff} step size in the M-dwarf domain.

Radii (Fig. 24). We compared our \mathcal{R} , derived from VOSA's L (BT-Settl CIFIST, $[\text{Fe}/\text{H}] = 0$) and T_{eff} using the Stefan-Boltzmann law, with the same works as in Fig. 19 (top left panel). Some of these works in turn compared their results with

independent direct radius determinations (e.g. near-infrared interferometry – Boyajian et al. 2012; von Braun et al. 2014). On average, our \mathcal{R} are larger by $0.022 \pm 0.037 R_{\odot}$, meaning they are identical within the dispersion of the data. However, the standard deviation includes both random errors (in magnitudes, parallax, SED integration) and systematic errors (in passband λ_{eff} and W_{eff} , VOSA minimisation procedure, CIFIST models), and the \mathcal{R} difference appears systematically across the whole sample, so it is likely to be significant. Furthermore, because of the T_{eff} shift with respect to Passegger et al. (2018) and other spectral synthesis works, our \mathcal{R} are also larger by about 5% than

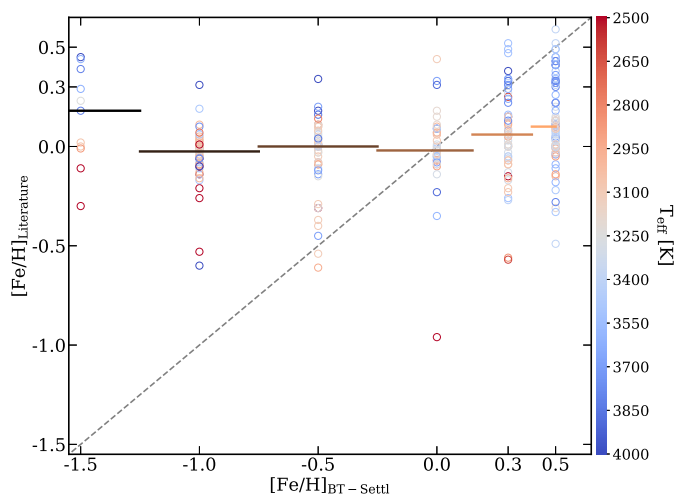


Fig. 22. Comparison of metallicities from VOSA BT-Settl fit and from literature for CARMENES GTO M dwarfs, colour-coded by BT-Settl CIFIST T_{eff} . Horizontal lines represent the median values in each BT-Settl [Fe/H] bin.

those of Schweitzer et al. (2019), who used almost identical L to ours. For that reason, when T_{eff} from spectral synthesis on high-resolution spectra is available, we recommend using it together with our L for determining \mathcal{R} (and \mathcal{M}), and use T_{eff} from VOSA when there is no spectral synthesis.

In spite of the large spread at spectral types earlier than M4.5 V and some poorly sampled SEDs later than M7.0 V, the matches with the \mathcal{R} -spectral type relation of Pecaut & Mamajek (2013) and the values reported by Mann et al. (2015) are also good (top right panel). Our \mathcal{R} - T_{eff} diagram (bottom left panel) naturally reproduces the sigmoid shape predicted by the widely used theoretical models of Baraffe et al. (1998), but shifted by ~ 100 K towards cooler T_{eff} (see previous paragraph). More than two decades after that cornerstone work by the Lyon group, Rabus et al. (2019) fitted an \mathcal{R} - T_{eff} relation using two linear polynomials and identified a discontinuous behaviour that the authors attributed to the transition between partially and fully convective stars at 3200–3340 K or $\sim 0.23 M_{\odot}$. Soon after, Cassisi & Salaris (2019) confirmed this discontinuity, but considered instead the contribution of the electron degeneracy to the gas equation of state as the physical phenomenon behind this behaviour (see also Chabrier & Baraffe 1997). While the boundary between partially and fully convective stars is better exposed in for example the $NUV - G_{RP}$ versus spectral type diagram (see Fig. A.2), in our data we did not find evidence for any discontinuity in the vicinity of 3250 K in the \mathcal{R} - T_{eff} diagram, but just a change of slope, as proven by Schweitzer et al. (2019, (see their Fig. 11)). The statistics in Rabus et al. (2019) were poorer than ours: they added around one hundred objects from Mann et al. (2015) to their sample of 22 low-mass dwarfs, while we have 1031 homogeneously investigated stars with T_{eff} in the 3000–3500 K interval. Furthermore, the continuity of \mathcal{R} as a function of L is obvious in the bottom right panel of Fig. 24.

Masses (Fig. 25). We compared our \mathcal{M} , derived from our \mathcal{R} and the \mathcal{M} - \mathcal{R} relation of Schweitzer et al. (2019), with those from the literature (same works as in Fig. 19, left panel). This comparison is shown in the left panel of Fig. 25. Among our parameters, \mathcal{M} is the one that shows more dissimilarities with respect to published values, although $\mathcal{M}_{\text{This work}} - \mathcal{M}_{\text{lit}} =$

$0.025 \pm 0.081 M_{\odot}$, consistent with a null difference (but probably significant as in \mathcal{M} when random and systematic errors are taken into account). For example, the two stars for which our \mathcal{M} deviate more than 80 % from published values are LP 229–17 (M3.5 V, $\mathcal{M}_{\text{This work}} = 0.476 \pm 0.017 M_{\odot}$, $\mathcal{M}_{\text{lit}} = 0.23 \pm 0.08 M_{\odot}$) and YZ CMi (M4.5 V, $\mathcal{M}_{\text{This work}} = 0.368 \pm 0.008 M_{\odot}$, $\mathcal{M}_{\text{lit}} = 0.19 \pm 0.08 M_{\odot}$), both from Gaidos & Mann (2014). The former star was tabulated as a spectroscopic binary by Houdebine et al. (2019), although we do not see any CARMENES radial-velocity variation attributable to binarity (Reiners et al. 2018b, see also Cortés-Contreras et al. 2017 for a lucky imaging analysis), while the latter star is a candidate member of the young β Pictoris moving group (not in Table 4 – Montes et al. 2001; Alonso-Floriano et al. 2015a) with strong chromospheric activity (Kahler et al. 1982; Kowalski et al. 2010; Tal-Or et al. 2018), which may partly explain the differences. In planet-host stars, such changes can translate into significant differences in the published (minimum) masses of M-dwarf planets.

We also compared our values of \mathcal{M} with those calculated from the \mathcal{M} - M_K relations of Delfosse et al. (2000), valid for $4.5 \text{ mag} \leq M_K \leq 9.5 \text{ mag}$, and Benedict et al. (2016), valid for $M_K \leq 10 \text{ mag}$, and the \mathcal{M} - M_{K_s} relation of Mann et al. (2019), valid for $4 \text{ mag} \leq M_{K_s} \leq 11 \text{ mag}$, and “safe” for $4.5 \text{ mag} \leq M_{K_s} \leq 10.5 \text{ mag}$. For the relations of Delfosse et al. (2000), we converted our 2MASS K_s magnitudes to CIT K values (Elias et al. 1982) using the colour transformation provided by Carpenter (2001). The means of the mass differences were: $\mathcal{M}_{\text{This work}} - \mathcal{M}_{\text{Del00}} = -0.0080 \pm 0.0320 M_{\odot}$, $\mathcal{M}_{\text{This work}} - \mathcal{M}_{\text{Ben06}} = 0.0242 \pm 0.0474 M_{\odot}$, and $\mathcal{M}_{\text{This work}} - \mathcal{M}_{\text{Man19}} = 0.0042 \pm 0.0223 M_{\odot}$. Taking into account the standard deviations, Mann et al. (2019) provided the relation that best matched our \mathcal{M} . In the right panel of Fig. 25 we show this relation, valid in a wide mass range from $0.075 M_{\odot}$ to $0.70 M_{\odot}$. Since we fixed $[\text{Fe}/\text{H}] = 0$, we used the Mann et al. (2019) relation independent of metallicity ($f = 0$). Besides, the authors stated that the impact of $[\text{Fe}/\text{H}]$ is sufficiently weak for the $f = 0$ relation to be safely used for most stars in the solar neighbourhood.

Colours (Fig. 26). Although with the advent of *Gaia* the $V - J$ colour should be replaced by $G - J$, the former had been used extensively in the past. The match of our mean $V - J$ colours as a function of T_{eff} with those of Pecaut & Mamajek (2013) is once again excellent, but the relation significantly deviates from the values tabulated by Casagrande et al. (2008). However, as noted by them, the range of applicability of their colour-temperature-metallicity relations involving $V - J$ is narrow, between 0.61 mag and 2.44 mag. As a result, from the top left panel, extrapolating the T_{eff} versus $V - J$ relation of Casagrande et al. (2008) beyond 2.44 mag may result in T_{eff} systematically cooler by more than 300 K. In the top right panel, we revisit the $r' - i'$ -spectral type diagram, which is an evolution of that with $R - I$ colour in the Johnson-Cousins passbands (Veeder 1974; Bessell 1979; Leggett 1992; Boyajian et al. 2012; Mann et al. 2015; Houdebine et al. 2019). We reproduce the reversal at M7.0–8.0 V ($r' - i' \sim 2.8 \text{ mag}$) observed by Hawley et al. (2002), Bochanski et al. (2007), and West et al. (2008), among many others. Therefore, we confirm that the $r' - i'$ colour alone cannot be used for spectral classification beyond M5.0 V. In the optical colour-colour diagram of the bottom left panel, our $g' - r'$ colours are slightly bluer than those of Davenport et al. (2014) for a fixed $r' - i'$, and significantly bluer, by about 0.5 mag, than those of Bochanski et al. (2007). Finally, in the bottom right panel, there

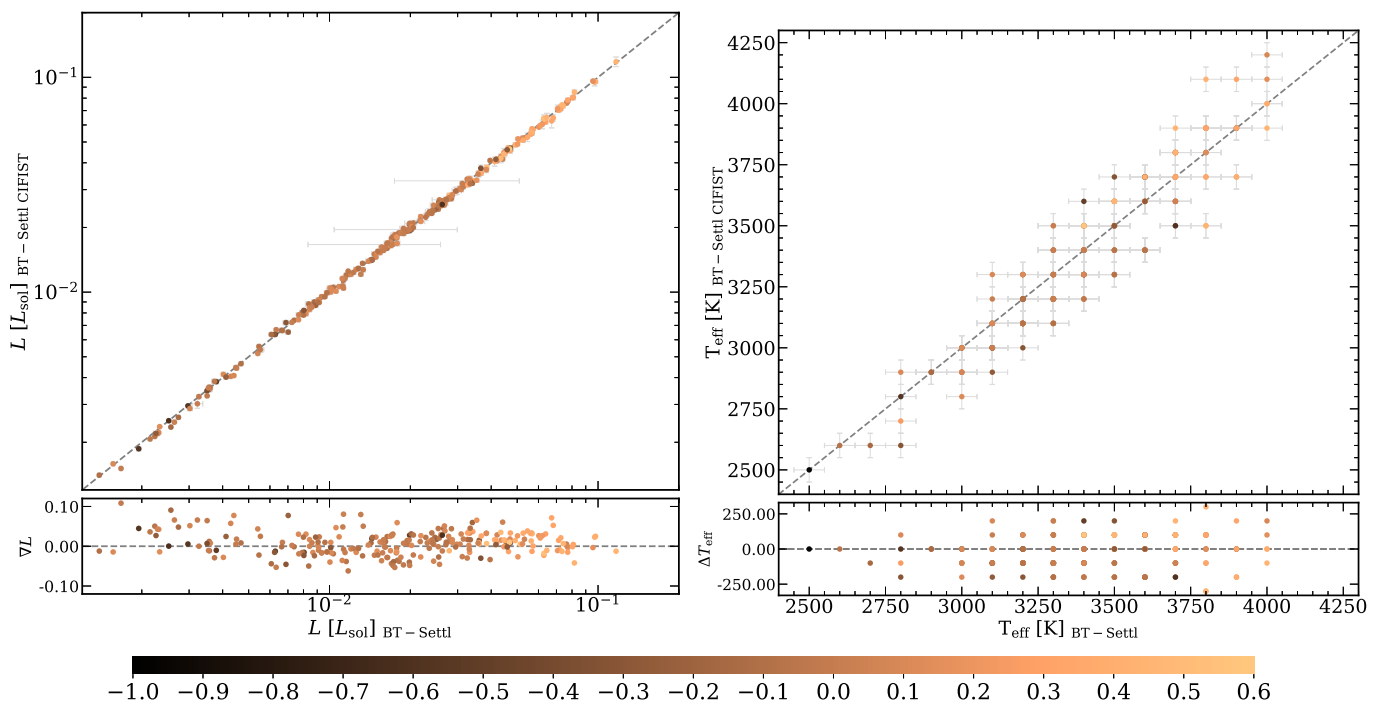


Fig. 23. Comparison of previous and recomputed L (left) and T_{eff} (right) using BT-Settl with $[\text{Fe}/\text{H}] = -1.5$ to $+0.5$ for CARMENES GTO M dwarfs, colour-coded by metallicities published in the literature. The small bottom panels depict $\nabla L = \log L_{\text{BT-Settl CIFIST}} - \log L_{\text{BT-Settl}}$ (left) and $\Delta T_{\text{eff}} = T_{\text{eff, BT-Settl CIFIST}} - T_{\text{eff, BT-Settl}}$ (right).

is a good agreement with the location of the M-dwarf main sequence of Knapp et al. (2004) in the near-infrared M_J versus $J - K_s$ diagram, but our data show instead the turnovers towards bluer and redder $J - K_s$ colours of late-K dwarfs and early-L dwarfs, respectively.

5. Summary

Here we present the most comprehensive photometric analysis to date of M dwarfs in the close solar neighbourhood, many of which are being followed-up by current radial-velocity and transit exoplanet surveys. We started with the latest version of the CARMENES input catalogue of 2194 M dwarfs, dubbed Carmencita, to which we added 168 and 117 single, nearby, bright K and ultracool dwarfs, respectively. Although our main objective was investigating luminosities, colours, and spectral energy distributions of M dwarfs, our sample contains stars and ultracool dwarfs as early as K5 V and as late as L8, which may avoid any boundary value problem. From public all-sky surveys, we collected 40 094 photometric magnitudes for the 2479 stars and ultracool dwarfs in 20 different passbands from the far ultraviolet, through the blue and red optical and near infrared, to the mid infrared. Except for the bluest passbands, the completeness of high-quality data is of the order of 97%. Thanks especially to *Gaia*, we could collect parallactic distances for 97.8% of the sample and identified close multiple systems unresolved by ground all-sky surveys and *WISE*. From the new data, we estimated spectro-photometric distances for 31 single stars without parallactic distance, and tabulated angular separations and position angles for 40 new close multiple systems and candidates.

Next, we computed bolometric luminosities, effective temperatures, and surface gravities for 1843 stars and ultracool dwarfs with parallactic distance and no physical companions at less than 5 arcsec or less than 5 mag fainter in *Gaia* G than

our target. For that, we used VOSA and all high-quality photometric data redder than SDSS u' . Because of the limitations of the BT-Settl CIFIST models implemented in VOSA, we set the metallicity to solar. However, except for a few stars with poorly sampled spectral energy distributions, the luminosities are independent of models at least at the 99.5% level. They supersede any pre-*Gaia* determination. From their loci in the Hertzsprung-Russell diagram, we identified 36 overluminous stars that had been previously assigned to young stellar kinematic groups and associations.

We examined colour-spectral type, colour-colour, colour-magnitude, luminosity-magnitude, and bolometric correction-colour diagrams. After discarding stars with young ages, close companions, and bad photometric or astrometric quality flags (i.e. *Gaia* `phot_bp_rp_excess_factor` and `RUWE`), we fitted empirical relations of absolute magnitude-colour, bolometric correction-colour, and luminosity-absolute magnitudes including widely available G , r' , and J magnitudes and *Gaia* DR2 parallaxes. In addition, we also used the Stefan-Boltzmann law and the M - R relation of Schweitzer et al. (2019) to derive radii and masses of all well-behaved stars in our sample. Finally, we tabulated median G - and J -band bolometric corrections, L , T_{eff} , R , and M , as well as absolute magnitudes in 14 passbands, for stars and ultracool dwarfs with spectral types from K5 V to L2.0.

We provide a summary table with the compiled astrophotometric data and derived stellar parameters of all our targets. The assembled catalogue in comma separated value (csv) format is available in its entirety in the electronic edition. As described in Table 8, for each star or ultracool dwarf we tabulate its identifiers, equatorial coordinates, spectral type (and reference), parallax and distance (and reference), all magnitudes and their uncertainties, origin, quality flags (when available), L , T_{eff} , and $\log g$ from VOSA, R and M from the Stefan-Boltzmann law and the M - R relation, *Gaia* DR2 identifier for primary and secondary sources (in the case of binary sources), four Boolean in-

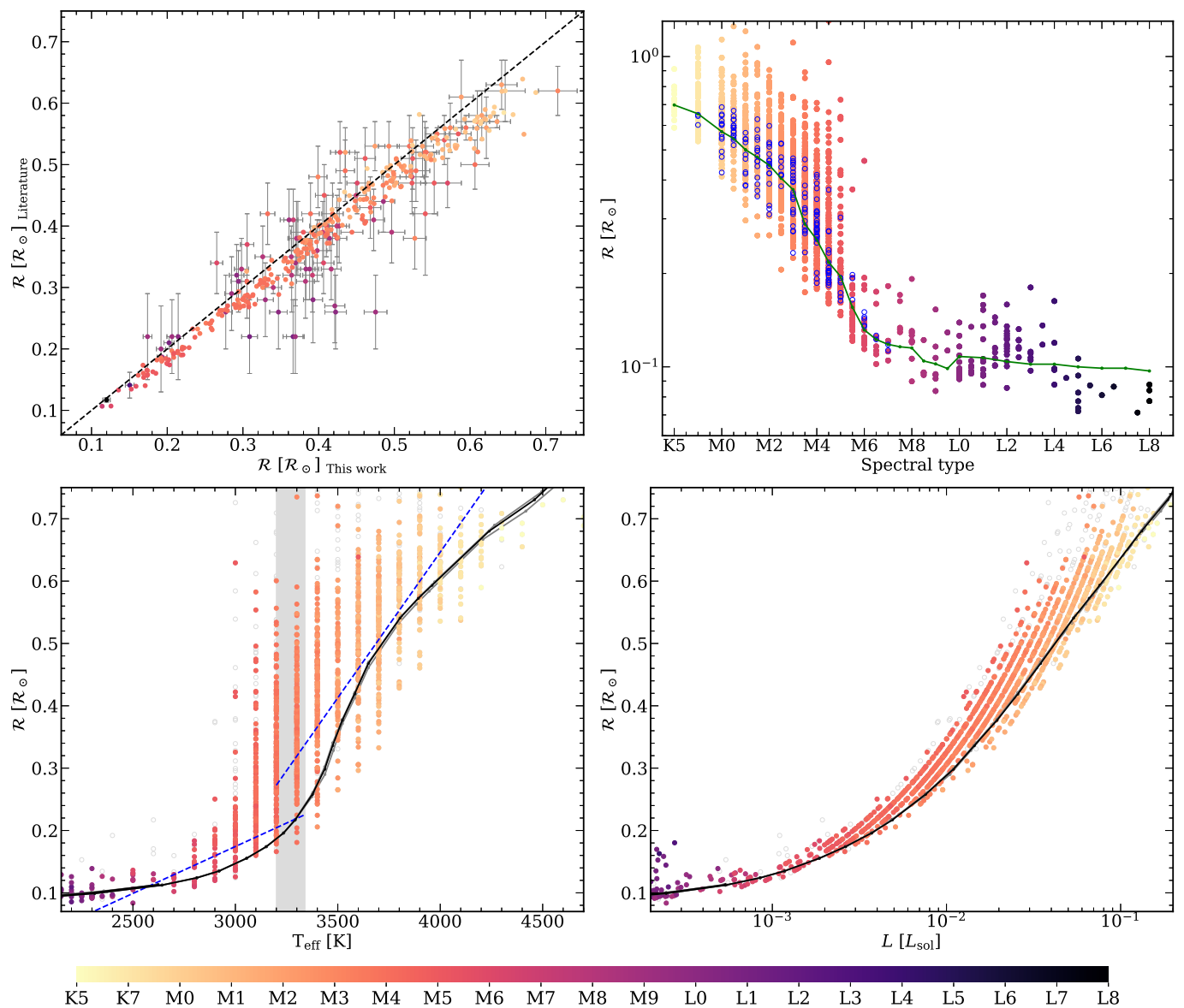


Fig. 24. Four representative diagrams involving \mathcal{R} . In the four panels our investigated stars are represented with filled circles colour-coded by spectral type. Top left: Comparison of \mathcal{R} from this work and from the literature, including Schweitzer et al. 2019 (with symbol-size error bars). Top right: Individual (coloured points) and median (black circles) values of \mathcal{R} as a function of the spectral sequence shown in Table 6. The green line marks the median values from Pecaut & Mamajek (2013) and the blue circles are stars from Mann et al. (2015). Bottom left: \mathcal{R} vs. T_{eff} . The black and grey solid lines are the NextGen isochrones of the Lyon group for 1.0, 4.0, and 8.0 Ga (overlapping), the blue dashed lines are the linear fittings from Rabus et al. (2019), and the grey shaded area is the region where they reported a possible discontinuity. Bottom right: \mathcal{R} vs. L . The black solid lines are the same isochrones as in the bottom left panel.

dices for close multiplicity ($\rho < 5$ arcsec), astrometric and photometric quality of the *Gaia* solution, and youth. Finally, most of the Python code developed by us for determining the parameters or preparing the plots shown in this work is available at GitHub¹¹.

There are many ways of improving our L , \mathcal{R} , and \mathcal{M} determinations. CatWISE (Eisenhardt et al. 2020), a recent NeOWISE enhanced and contributed product (Mainzer et al. 2011), represents a step forward with respect to the AllWISE mid-infrared photometry used here. The *Gaia* DR3, previously scheduled for the second half of 2021, will improve G , G_{BP} , and G_{RP} photometry and, especially, astrometry, with which we will have more accurate parallax and close multiplicity determinations. Soon af-

ter, in early 2022, the LSST, with its spectacularly large etendue and multi-band photometry in $u'g'r'i'z'y'$ passbands, will start operations. The first LSST data release will supersede all previous UCAC, SDSS, and Pan-STARRS optical datasets (but see also J-PAS, Benítez et al. 2014). The ESA *Euclid* mission will complement LSST in the near infrared at Galactic latitudes far from the ecliptic, especially for the latest M dwarfs. By that time, new grids of theoretical atmospheric models, with a much wider range of metallicities, will be available for VOSA, which will also be upgraded. Thanks to the Transiting Exoplanet Survey Satellite (*TESS*) and the discovery of new detached M-dwarf eclipsing binaries, the \mathcal{M} - \mathcal{R} relation will be refined and probably determined for different intervals of age.

There are even more ways to improve our results. To name a few: new volume-limited samples including all M dwarfs known

¹¹ <https://github.com/ccifuentesr/CARMENES-V>

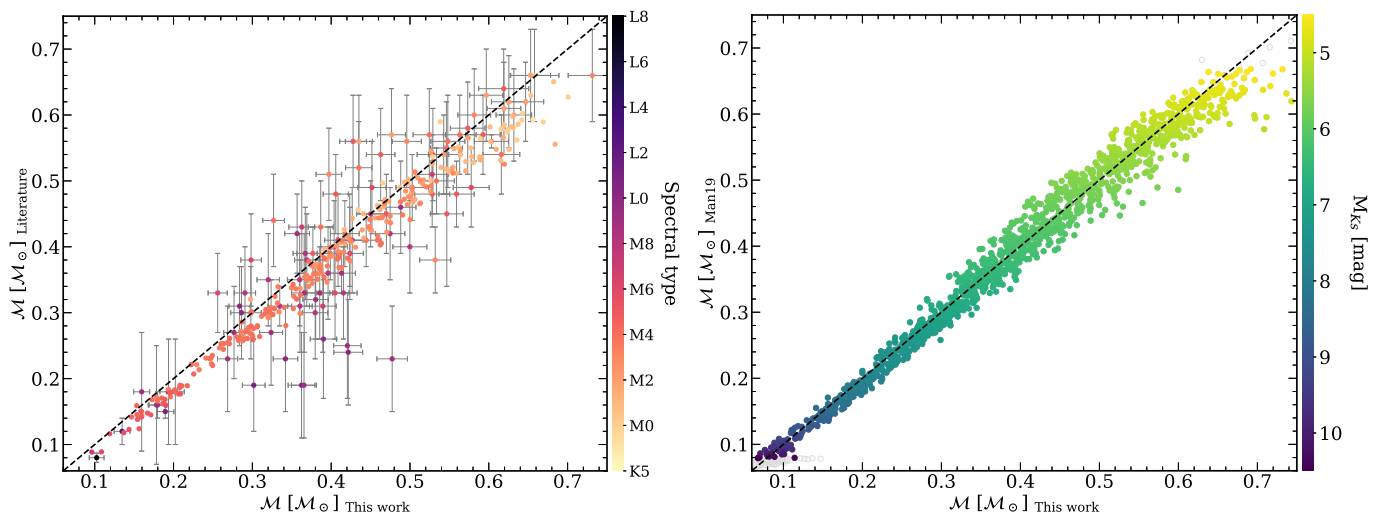


Fig. 25. Left: Comparison of our masses with those from the literature. Right: Comparison with those derived from absolute magnitude M_{K_s} using the metallicity-independent relation from Mann et al. (2019) only in its validity range ($4.5 \text{ mag} < M_{K_s} < 10.5 \text{ mag}$).

Table 8. Description of the online table.

Parameter	Units	Column(s)	Description
Karmn	...	1	Carmencita star identifier (JHHMMm+DDd) ^a
Name	...	2	Discovery name or most common name ^b
RA, DE	hms	3–4	Right ascension and declination (equinox J2000, epoch J2015.5)
SpType, SpTnum	...	5–6	Spectral type and its numerical format ^c
Ref_SpT	...	7	Reference for the spectral type
Plx, ePlx	mas	8–9	Parallax and its uncertainty
Ref_Plx	...	10	Reference for the parallax
d_pc, ed_pc	pc	11–12	Distance and its uncertainty
Ref_d	...	13	Reference for the distance
Lbol, eLbol	L_{\odot}	14–15	Luminosity and its uncertainty from VOSA
Teff	K	16	Effective temperature from VOSA ^d
logg	dex	17	Surface gravity from VOSA ^d
Radius, eRadius	R_{\odot}	18–19	Radius and its uncertainty
Mass, eMass	M_{\odot}	20–21	Mass and its uncertainty
NN_mag, eNN_mag	mag	22–97	Magnitude and its uncertainty for the NN passband ^e
Qf_NN, Ref_NN	mag	22–97	Quality flag (if available) and reference for the NN passband ^e
Gaia_id_1	...	98	<i>Gaia</i> DR2 identifier of single or primary star
Gaia_id_2	...	99	<i>Gaia</i> DR2 identifier of secondary star in close binary system
Multiple	...	100	Boolean index for close multiple stars
Young	...	101	Boolean index for overluminous young stars
RUWE	...	102	Boolean index for stars with <i>Gaia</i> RUWE > 1.41
Excess	...	103	Boolean index for stars with photometric flux excess in <i>Gaia</i> G_{B_p} and G_{R_p} passbands

Notes. ^(a) For the K dwarfs, we tabulate the SUPERBLINK catalogue identifier (Lépine & Shara 2005; Lépine et al. 2013). ^(b) For the ultracool dwarfs, we tabulate the *Gaia* UltraCool Dwarf Catalogue identifier (Smart et al. 2017, 2019). ^(c) SpTnum = –2 for K5 V, –1 for K7 V, 0.0 for M0.0 V, 0.5 for M0.5 V... 10.0 for L0.0, etc. ^(d) VOSA uncertainties are 50 K for T_{eff} (25 K for $T_{\text{eff}} \lesssim 2400$ K) and 0.5 dex for $\log g$. ^(e) FUV, NUV: GALEX DR5 FUV and NUV; BP, GG, RP: G_{B_p} , G , and G_{R_p} from *Gaia* DR2; BT, VT: B_T and V_T from Tycho-2; B, V: B and V from UCAC4 or APASS9; u, g, r, i: u' , g' , r' , and i' from SDSS9, UCAC4, APASS9, PanSTARRS-1 and/or CMC15; J, H, Ks: J , H , and K_s from 2MASS; W1, W2, W3, W4: W1, W2, W3, and W4 from AllWISE or WISE.

in the solar vicinity, not only limited to the Calar Alto sky, plus more intermediate- and late-K dwarfs and ultracool dwarfs, especially in the M6.0–9.5 V range; new spectral-synthesis determinations of T_{eff} , $\log g$, and [Fe/H] in late-type stars for calibration (e.g. with the equivalent width method or with deep learning – Marfil et al. 2018; V.M. Passegger et al., in prep.); discovery of low-mass spectroscopic binaries; or new studies that link kinematics, activity, and youth (and, therefore, radius

and surface gravity). All these will be taken into account by the CARMENES consortium to improve our knowledge of M dwarfs and their planets.

Acknowledgements. We thank the anonymous referee for the comments that helped to improve the quality of this paper, and also E. E. Mamajek and E. Gaidos for their valuable insights and suggestions. CARMENES is an instrument for the Centro Astronómico Hispano-Alemán de Calar Alto (CAHA, Almería, Spain). CARMENES is funded by the German Max-Planck-Gesellschaft (MPG), the Spanish Consejo Superior de Investigaciones Científicas (CSIC), the Eu-

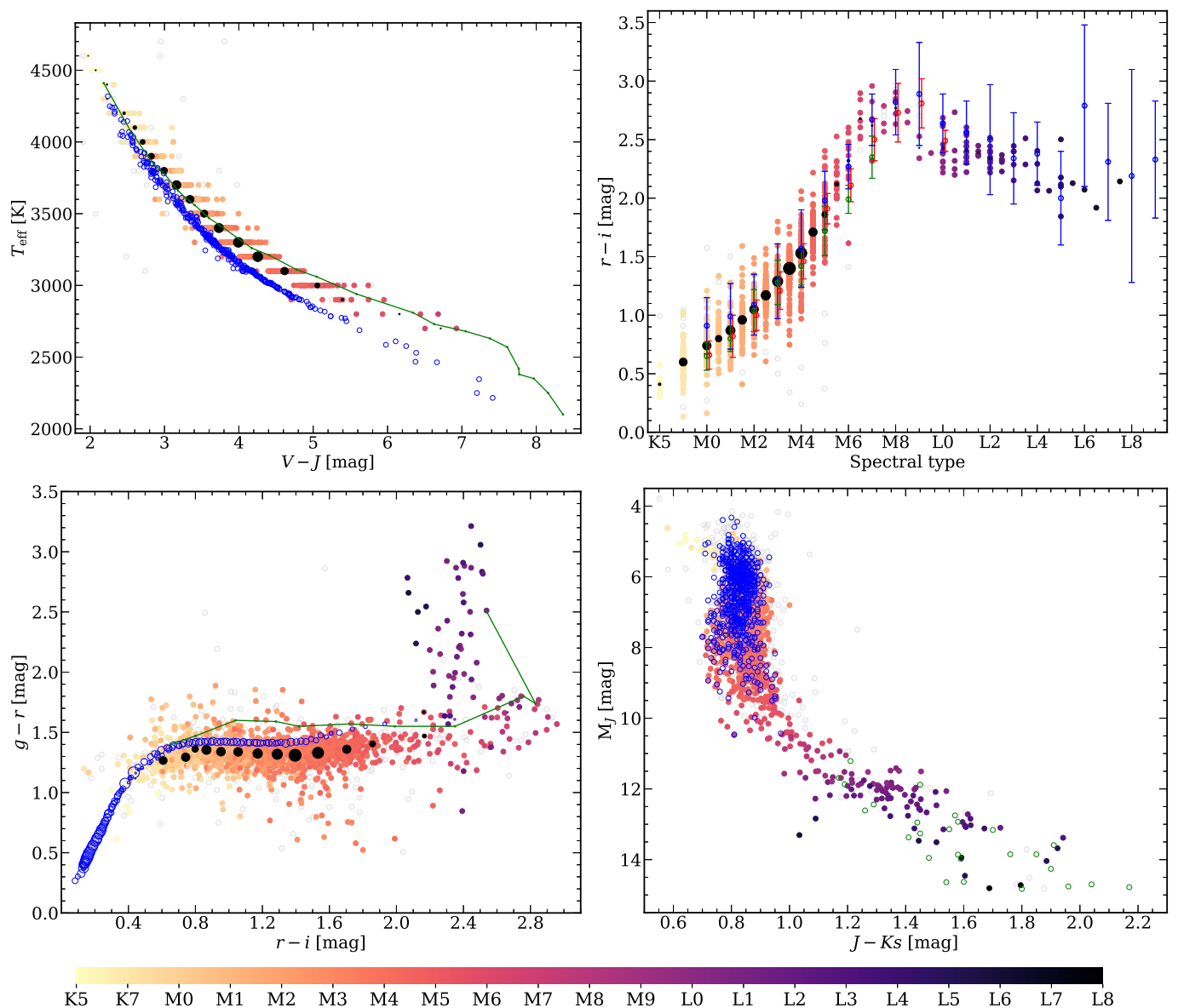


Fig. 26. Top left: T_{eff} vs. $V - J$. The blue empty circles and green line are data from Casagrande et al. (2008) and Pecaut & Mamajek (2013), respectively. Black filled circles are the mean colours from 2700 K to 4600 K in our sample, with a size proportional to the number of stars. Top right: $r' - i'$ vs. spectral type. Open circles are the mean colours of Hawley et al. (2002, blue), Bochanski et al. (2007, “inactive” colours, green), and West et al. (2008, red). Black filled circles are the mean colours from K5 V to L2 in our sample, taken from Table A.2, with a size proportional to the number of stars. The error bars are the standard deviation (Hawley et al. 2002; Bochanski et al. 2007) and the intrinsic scatter of the stellar locus (West et al. 2008). Bottom left: $g' - r'$ vs. $r - i'$. Black filled circles are the mean colours from K5 V to L2 in our sample, taken from Table A.2, with a size proportional to the number of stars. Blue empty circles are the mean colours by Davenport et al. (2014), with a size proportional to the numbers of stars, and the green line links the mean “inactive” colours by Bochanski et al. (2007) for spectral types M0 V to L0. Bottom right: M_J vs. $J - K_s$. Green and blue empty circles are data from Knapp et al. (2004) and Lépine et al. (2013), respectively. In the four panels, the stars in our sample are colour-coded by spectral type, and the discarded stars are plotted with grey empty circles.

ropean Union through FEDER/ERF FICTS-2011-02 funds, and the members of the CARMENES Consortium (Max-Planck-Institut für Astronomie, Instituto de Astrofísica de Andalucía, Landessternwarte Königstuhl, Institut de Ciències de l’Espai, Institut für Astrophysik Göttingen, Universidad Complutense de Madrid, Thüringer Landessternwarte Tautenburg, Instituto de Astrofísica de Canarias, Hamburger Sternwarte, Centro de Astrobiología and Centro Astronómico Hispano-Alemán), with additional contributions by the Spanish Ministry of Economy, the German Science Foundation through the Major Research Instrumentation Programme and DFG Research Unit FOR2544 “Blue Planets around Red Stars”, the Klaus Tschira Stiftung, the states of Baden-Württemberg and Niedersachsen, and by the Junta de Andalucía. This work was partly financed by the Spanish Ministry of Science and Innovation through grants AYA2016-79425-C3-1/2/3-P and BES-2017-080769, and by NASA through grant NNX17AG24G. C.C., F.J.A.P., R.D., and G.H. compiled data for this work during their MSc the-

ses at the Universidad Complutense de Madrid. This publication made use of VOSA and the Filter Profile Service, developed and maintained by the Spanish Virtual Observatory through grant AYA2017-84089, the SIMBAD database, the Aladin sky atlas, and the Vizier catalogue access tool developed at CDS, Strasbourg Observatory, France, and the Python libraries Matplotlib, NumPy, SciPy and collection of software packages AstroPy.

References

- Adams, F. C. & Laughlin, G. 1997, *Reviews of Modern Physics*, 69, 337
 Affer, L., Damasso, M., Micela, G., et al. 2019, *A&A*, 622, A193
 Affer, L., Micela, G., Damasso, M., et al. 2016, *A&A*, 593, A117
 Ahn, C. P., Alexandroff, R., Allende Prieto, C., et al. 2012, *ApJS*, 203, 21

- Allard, F., Homeier, D., & Freytag, B. 2012, *Philosophical Transactions of the Royal Society of London Series A*, 370, 2765
- Alonso-Floriano, F. J., Caballero, J. A., Cortés-Contreras, M., Solano, E., & Montes, D. 2015a, *A&A*, 583, A85
- Alonso-Floriano, F. J., Morales, J. C., Caballero, J. A., et al. 2015b, *A&A*, 577, A128
- Anglada-Escudé, G., Amado, P. J., Barnes, J., et al. 2016, *Nature*, 536, 437
- Ansdell, M., Gaidos, E., Mann, A. W., et al. 2015, *ApJ*, 798, 41
- Arenou, F., Luri, X., Babusiaux, C., et al. 2018, *A&A*, 616, A17
- Astudillo-Defru, N., Forveille, T., Bonfils, X., et al. 2017, *A&A*, 602, A88
- Bahcall, J. N. & Soneira, R. M. 1980, *ApJS*, 44, 73
- Bailer-Jones, C. A. L., Rybizki, J., Fousneau, M., Mantelet, G., & Andrae, R. 2018, *AJ*, 156, 58
- Baraffe, I., Chabrier, G., Allard, F., & Hauschildt, P. H. 1998, *A&A*, 337, 403
- Baraffe, I., Homeier, D., Allard, F., & Chabrier, G. 2015, *A&A*, 577, A42
- Baroch, D., Morales, J. C., Ribas, I., et al. 2018, *A&A*, 619, A32
- Bartlett, J. L., Lurie, J. C., Riedel, A., et al. 2017, *AJ*, 154, 151
- Bayo, A., Rodrigo, C., Barrado Y Navascués, D., et al. 2008, *A&A*, 492, 277
- Benedict, G. F., Henry, T. J., Franz, O. G., et al. 2016, *AJ*, 152, 141
- Benítez, N., Dupke, R., Moles, M., et al. 2014, *arXiv e-prints*, arXiv:1403.5237
- Bessell, M. S. 1979, *PASP*, 91, 589
- Bessell, M. S., Castelli, F., & Plez, B. 1998, *A&A*, 333, 231
- Best, W. M. J., Magnier, E. A., Liu, M. C., Aller, K. M., & Zhang, Z. 2017, in *American Astronomical Society Meeting Abstracts*, Vol. 229, *American Astronomical Society Meeting Abstracts #229*, 240.01
- Bianchi, L., Herald, J., Efremova, B., et al. 2011, *Ap&SS*, 335, 161
- Binks, A. S. & Jeffries, R. D. 2016, *MNRAS*, 455, 3345
- Bochanski, J. J., Hawley, S. L., Covey, K. R., et al. 2010, *AJ*, 139, 2679
- Bochanski, J. J., Munn, J. A., Hawley, S. L., et al. 2007, *AJ*, 134, 2418
- Böhm-Vitense, E., Böhm-Vitense, E., & Hm-Vitense, E. 1989, *Introduction to Stellar Astrophysics: Volume 1, Basic Stellar Observations and Data, Introduction to Stellar Astrophysics* (Cambridge University Press)
- Bonfils, X., Delfosse, X., Udry, S., et al. 2013, *A&A*, 549, A109
- Bonfils, X., Delfosse, X., Udry, S., et al. 2005, *A&A*, 442, 635
- Bonfils, X., Gillon, M., Udry, S., et al. 2012, *A&A*, 546, A27
- Bonnarel, F., Fernique, P., Bienaymé, O., et al. 2000, *A&AS*, 143, 33
- Boss, A. P. 2006, *ApJ*, 643, 501
- Boyajian, T. S., von Braun, K., van Belle, G., et al. 2012, *ApJ*, 757, 112
- Burgasser, A. J., Looper, D., & Rayner, J. T. 2010, *AJ*, 139, 2448
- Caballero, J. A., Béjar, V. J. S., Rebolo, R., & Zapatero Osorio, M. R. 2004, *A&A*, 424, 857
- Caballero, J. A., Burgasser, A. J., & Klement, R. 2008, *A&A*, 488, 181
- Caballero, J. A., Cortés-Contreras, M., Alonso-Floriano, F. J., et al. 2016, in *19th Cambridge Workshop on Cool Stars, Stellar Systems, and the Sun (CS19)*, *Cambridge Workshop on Cool Stars, Stellar Systems, and the Sun*, 148
- Caballero, J. A., de Burgos, A., Alonso-Floriano, F. J., et al. 2019, *A&A*, 629, A114
- Carpenter, J. M. 2001, *AJ*, 121, 2851
- Casagrande, L., Flynn, C., & Bessell, M. 2008, *MNRAS*, 389, 585
- Cassisi, S. & Salaris, M. 2019, *A&A*, 626, A32
- Chabrier, G. 2003, *PASP*, 115, 763
- Chabrier, G. & Baraffe, I. 1997, *A&A*, 327, 1039
- Chambers, K. C., Magnier, E. A., Metcalfe, N., et al. 2016, *ArXiv e-prints* [arXiv:1612.05560]
- Chelli, A. & Duvert, G. 2016, *A&A*, 593, L18
- Clanton, C. & Gaudi, B. S. 2014, *ApJ*, 791, 91
- Clarke, J. R. A., Pinfield, D. J., Gálvez-Ortiz, M. C., et al. 2010, *MNRAS*, 402, 575
- Cochrane, K. M. & Smith, G. H. 2019, *PASP*, 131, 114201
- Cortés-Contreras, M., Béjar, V. J. S., Caballero, J. A., et al. 2017, in *Highlights on Spanish Astrophysics IX*, ed. S. Arribas, A. Alonso-Herrero, F. Figueras, C. Hernández-Monteagudo, A. Sánchez-Lavega, & S. Pérez-Hoyos, 497–498
- Covey, K. R., Hawley, S. L., Bochanski, J. J., et al. 2008, *AJ*, 136, 1778
- Covey, K. R., Ivezić, Ž., Schlegel, D., et al. 2007, *AJ*, 134, 2398
- Crain, J. N., Sanders, W. L., Fomalont, E. B., & Sramek, R. A. 1986, *PASP*, 98, 325
- Cruz, K. L., Kirkpatrick, J. D., & Burgasser, A. J. 2009, *AJ*, 137, 3345
- Cutri, R. M. & et al. 2012, *VizieR Online Data Catalog*, 2311
- Cutri, R. M. & et al. 2014, *VizieR Online Data Catalog*, 2328
- Dahn, C. C., Harris, H. C., Subasavage, J. P., et al. 2017, *AJ*, 154, 147
- Dahn, C. C., Harris, H. C., Vrba, F. J., et al. 2002, *AJ*, 124, 1170
- Davenport, J. R. A., Ivezić, Ž., Becker, A. C., et al. 2014, *MNRAS*, 440, 3430
- del Burgo, C. & Allende Prieto, C. 2018, *MNRAS*, 479, 1953
- Delfosse, X., Forveille, T., Ségransan, D., et al. 2000, *A&A*, 364, 217
- Díez Alonso, E., Caballero, J. A., Montes, D., et al. 2019, *A&A*, 621, A126
- Díez Alonso, E., Suárez Gómez, S. L., González Hernández, J. I., et al. 2018, *MNRAS*, 476, L50
- Dittmann, J. A., Irwin, J. M., Charbonneau, D., & Berta-Thompson, Z. K. 2014, *ApJ*, 784, 156
- Dittmann, J. A., Irwin, J. M., Charbonneau, D., et al. 2017, *Nature*, 544, 333
- Dressing, C. D. & Charbonneau, D. 2015, *ApJ*, 807, 45
- Dupuy, T. J. & Liu, M. C. 2012, *ApJS*, 201, 19
- Eisenhardt, P. R. M., Marocco, F., Fowler, J. W., et al. 2020, *ApJS*, 247, 69
- Elias, J. H., Frogel, J. A., Matthews, K., & Neugebauer, G. 1982, *AJ*, 87, 1029
- Espada, D. 2019, MSc thesis, Universidad Complutense de Madrid, Spain
- Evans, D. W., Riello, M., De Angeli, F., et al. 2018, *A&A*, 616, A4
- Faherty, J. K., Rice, E. L., Cruz, K. L., Mamajek, E. E., & Núñez, A. 2013, *AJ*, 145, 2
- Faherty, J. K., Riedel, A. R., Cruz, K. L., et al. 2016, *ApJS*, 225, 10
- Ferguson, D., Gardner, S., & Yanny, B. 2017, *ApJ*, 843, 141
- Filippazzo, J. C., Rice, E. L., Faherty, J., et al. 2015, *ApJ*, 810, 158
- Finch, C. T. & Zacharias, N. 2016, *AJ*, 151, 160
- Fischer, D. A., Anglada-Escudé, G., Arriagada, P., et al. 2016, *PASP*, 128, 066001
- Fleming, T. A. 1998, *ApJ*, 504, 461
- Gagné, J., Lafrenière, D., Doyon, R., Malo, L., & Artigau, É. 2014, *ApJ*, 783, 121
- Gagné, J., Lafrenière, D., Doyon, R., Malo, L., & Artigau, É. 2015, *ApJ*, 798, 73
- Gaia Collaboration, Babusiaux, C., van Leeuwen, F., et al. 2018a, *A&A*, 616, A10
- Gaia Collaboration, Brown, A. G. A., Vallenari, A., et al. 2018b, *A&A*, 616, A1
- Gaia Collaboration, Brown, A. G. A., Vallenari, A., et al. 2016, *A&A*, 595, A2
- Gaidos, E. & Mann, A. W. 2014, *ApJ*, 791, 54
- Galli, P. A. B., Loinard, L., Ortiz-Léon, G. N., et al. 2018, *ApJ*, 859, 33
- Gatewood, G. & Coban, L. 2009, *AJ*, 137, 402
- Gillon, M., Triaud, A. H. M. J., Demory, B.-O., et al. 2017, *Nature*, 542, 456
- Gizis, J. E. 1997, *AJ*, 113, 806
- Gizis, J. E., Reid, I. N., & Hawley, S. L. 2002, *AJ*, 123, 3356
- Golimowski, D. A., Leggett, S. K., Marley, M. S., et al. 2004, *AJ*, 127, 3516
- Gray, R. O., Corbally, C. J., Garrison, R. F., McFadden, M. T., & Robinson, P. E. 2003, *AJ*, 126, 2048
- Habets, G. M. H. J. & Heintze, J. R. W. 1981, *A&AS*, 46, 193
- Haro, G., Iriarte, B., & Chavira, E. 1953, *Boletín de los Observatorios Tonantzintla y Tacubaya*, 1, 3
- Hawley, S. L., Covey, K. R., Knapp, G. R., et al. 2002, *AJ*, 123, 3409
- Hawley, S. L., Davenport, J. R. A., Kowalski, A. F., et al. 2014, *ApJ*, 797, 121
- Hawley, S. L., Gizis, J. E., & Reid, I. N. 1996, *AJ*, 112, 2799
- Heintz, W. D. 1987, *ApJS*, 65, 161
- Henden, A. A., Templeton, M., Terrell, D., et al. 2016, *VizieR Online Data Catalog*, 2336
- Henry, T. J., Jao, W.-C., Subasavage, J. P., et al. 2006, *AJ*, 132, 2360
- Henry, T. J., Kirkpatrick, J. D., & Simons, D. A. 1994, *AJ*, 108, 1437
- Henry, T. J. & McCarthy, Donald W., J. 1993, *AJ*, 106, 773
- Hernández, J., Hartmann, L., Calvet, N., et al. 2008, *ApJ*, 686, 1195
- Hewett, P. C., Warren, S. J., Leggett, S. K., & Hodgkin, S. T. 2006, *MNRAS*, 367, 454
- Hirano, T., Dai, F., Livingston, J. H., et al. 2018, *AJ*, 155, 124
- Hobson, M. J., Díaz, R. F., Delfosse, X., et al. 2018, *A&A*, 618, A103
- Høg, E., Fabricius, C., Makarov, V. V., et al. 2000, *A&A*, 355, L27
- Houdebine, É. R., Mullan, D. J., Doyle, J. G., et al. 2019, *AJ*, 158, 56
- Howard, A. W., Johnson, J. A., Marcy, G. W., et al. 2010, *ApJ*, 721, 1467
- Husser, T. O., Wende-von Berg, S., Dreizler, S., et al. 2013, *A&A*, 553, A6
- Janson, M., Durkan, S., Hippler, S., et al. 2017, *A&A*, 599, A70
- Jao, W.-C., Henry, T. J., Subasavage, J. P., et al. 2005, *AJ*, 129, 1954
- Jeffers, S. V., Schöfer, P., Lamert, A., et al. 2018, *A&A*, 614, A76
- Jenkins, L. F. 1952, *General catalogue of trigonometric stellar parallaxes*.
- Johnson, H. L., Mitchell, R. I., & Iriarte, B. 1962, *ApJ*, 136, 75
- Kahler, S., Golub, L., Harnden, F. R., et al. 1982, *ApJ*, 252, 239
- Kaiser, N., Burgett, W., Chambers, K., et al. 2010, in *Society of Photo-Optical Instrumentation Engineers (SPIE) Conference Series*, Vol. 7733, *Proc. SPIE*, 77330E
- Kasting, J. F., Whitmire, D. P., & Reynolds, R. T. 1993, *Icarus*, 101, 108
- Kirkpatrick, J. D. 2005, *ARA&A*, 43, 195
- Kirkpatrick, J. D., Henry, T. J., & Irwin, M. J. 1997, *AJ*, 113, 1421
- Kirkpatrick, J. D., Henry, T. J., & McCarthy, Jr., D. W. 1991, *ApJS*, 77, 417
- Kirkpatrick, J. D., Reid, I. N., Liebert, J., et al. 1999, *ApJ*, 519, 802
- Knapp, G. R., Leggett, S. K., Fan, X., et al. 2004, *AJ*, 127, 3553
- Kopparapu, R. k., Wolf, E. T., Arney, G., et al. 2017, *ApJ*, 845, 5
- Kowalski, A. F., Hawley, S. L., Holtzman, J. A., Wisniewski, J. P., & Hilton, E. J. 2010, *ApJ*, 714, L98
- Kundurthy, P., Agol, E., Becker, A. C., et al. 2011, *ApJ*, 731, 123
- Leggett, S. K. 1992, *ApJS*, 82, 351
- Lépine, S. & Bongiorno, B. 2007, *AJ*, 133, 889
- Lépine, S., Hilton, E. J., Mann, A. W., et al. 2013, *AJ*, 145, 102
- Lépine, S., Rich, R. M., & Shara, M. M. 2007, *ApJ*, 669, 1235
- Lépine, S. & Shara, M. M. 2005, *AJ*, 129, 1483
- Lépine, S., Thorstensen, J. R., Shara, M. M., & Rich, R. M. 2009, *AJ*, 137, 4109
- Liebert, J. & Gizis, J. E. 2006, *PASP*, 118, 659
- Lindgren, L., Hernández, J., Bombrun, A., et al. 2018, *A&A*, 616, A2
- Lindgren, S. & Heiter, U. 2017, *A&A*, 604, A97

- Luque, R., Pallé, E., Kossakowski, D., et al. 2019, *A&A*, 628, A39
- Mainzer, A., Bauer, J., Grav, T., et al. 2011, *ApJ*, 731, 53
- Maíz Apellániz, J. & Weiler, M. 2018, *A&A*, 619, A180
- Majewski, S. R., Schiavon, R. P., Frinchaboy, P. M., et al. 2017, *AJ*, 154, 94
- Makarov, V. V., Zacharias, N., Hennessy, G. S., Harris, H. C., & Monet, A. K. B. 2007, *ApJ*, 668, L155
- Maldonado, J., Affer, L., Micela, G., et al. 2015, *A&A*, 577, A132
- Maldonado, J., Scandariato, G., Stelzer, B., et al. 2017, *A&A*, 598, A27
- Malo, L., Artigau, É., Doyon, R., et al. 2014, *ApJ*, 788, 81
- Malo, L., Doyon, R., Lafrenière, D., et al. 2013, *ApJ*, 762, 88
- Mamajek, E. E., Torres, G., Prsa, A., et al. 2015, *arXiv e-prints*, arXiv:1510.06262
- Mann, A. W., Dupuy, T., Kraus, A. L., et al. 2019, *ApJ*, 871, 63
- Mann, A. W., Feiden, G. A., Gaidos, E., Boyajian, T., & von Braun, K. 2015, *ApJ*, 804, 64
- Mann, A. W., Gaidos, E., & Ansdell, M. 2013, *ApJ*, 779, 188
- Marfil, E., Montes, D., Taberner, H. M., et al. 2018, in *20th Cambridge Workshop on Cool Stars, Stellar Systems and the Sun*, Cambridge Workshop on Cool Stars, Stellar Systems, and the Sun, 32
- Marrese, P. M., Marinoni, S., Fabrizio, M., & Altavilla, G. 2019, *A&A*, 621, A144
- Mason, B. D., Wycoff, G. L., Hartkopf, W. I., Douglass, G. G., & Worley, C. E. 2001, *AJ*, 122, 3466
- Mochnicki, S. W., Gladders, M. D., Thomson, J. R., et al. 2002, *AJ*, 124, 2868
- Montes, D., González-Peinado, R., Taberner, H. M., et al. 2018, *MNRAS*, 479, 1332
- Montes, D., López-Santiago, J., Gálvez, M. C., et al. 2001, *MNRAS*, 328, 45
- Morales, J. C., Mustill, A. J., Ribas, I., et al. 2019, *Science*, 365, 1441
- Morales, J. C., Ribas, I., & Jordi, C. 2008, *A&A*, 478, 507
- Newton, E. R., Charbonneau, D., Irwin, J., & Mann, A. W. 2015, *ApJ*, 800, 85
- Niels Bohr Institute, Institute of Astronomy, C., & Real Instituto y Observatorio de La Armada. 2014, *VizieR Online Data Catalog*, 1327
- Passegger, V. M., Reiners, A., Jeffers, S. V., et al. 2018, *A&A*, 615, A6
- Passegger, V. M., Schweitzer, A., Shulyak, D., et al. 2019, *A&A*, 627, A161
- Passegger, V. M., Schweitzer, A., Shulyak, D., et al. 2020, *A&A*, 634, C2
- Pecaut, M. J. & Mamajek, E. E. 2013, *ApJS*, 208, 9
- Perryman, M. A. C., Brown, A. G. A., Lebreton, Y., et al. 1998, *A&A*, 331, 81
- Pirzkal, N., Sahu, K. C., Burgasser, A., et al. 2005, *ApJ*, 622, 319
- Preibisch, T., Guenther, E., & Zinnecker, H. 2001, *AJ*, 121, 1040
- Quirrenbach, A., Amado, P. J., Caballero, J. A., et al. 2014, *Society of Photo-Optical Instrumentation Engineers (SPIE) Conference Series*, Vol. 9147, CARMENES instrument overview, 91471F
- Quirrenbach, A., Amado, P. J., Ribas, I., et al. 2018, in *Society of Photo-Optical Instrumentation Engineers (SPIE) Conference Series*, Vol. 10702, Ground-based and Airborne Instrumentation for Astronomy VII, 107020W
- Rabus, M., Lachaume, R., Jordán, A., et al. 2019, *MNRAS*, 484, 2674
- Rajpurohit, A. S., Allard, F., Rajpurohit, S., et al. 2018a, *A&A*, 620, A180
- Rajpurohit, A. S., Allard, F., Teixeira, G. D. C., et al. 2018b, *A&A*, 610, A19
- Rajpurohit, A. S., Reylé, C., Allard, F., et al. 2013, *A&A*, 556, A15
- Ramírez, I. & Meléndez, J. 2005, *ApJ*, 626, 465
- Reid, I. N., Burgasser, A. J., Cruz, K. L., Kirkpatrick, J. D., & Gizis, J. E. 2001, *AJ*, 121, 1710
- Reid, I. N., Cruz, K. L., Allen, P., et al. 2004, *AJ*, 128, 463
- Reid, I. N., Gizis, J. E., Cohen, J. G., et al. 1997, *PASP*, 109, 559
- Reid, I. N., Hawley, S. L., & Gizis, J. E. 1995, *AJ*, 110, 1838
- Reiners, A., Joshi, N., & Goldman, B. 2012, *AJ*, 143, 93
- Reiners, A., Ribas, I., Zechmeister, M., et al. 2018a, *A&A*, 609, L5
- Reiners, A., Zechmeister, M., Caballero, J. A., et al. 2018b, *A&A*, 612, A49
- Riaz, B., Gizis, J. E., & Harvin, J. 2006, *AJ*, 132, 866
- Ribas, I., Tuomi, M., Reiners, A., et al. 2018, *Nature*, 563, 365
- Riedel, A. R., Subasavage, J. P., Finch, C. T., et al. 2010, *AJ*, 140, 897
- Rojas-Ayala, B., Covey, K. R., Muirhead, P. S., & Lloyd, J. P. 2012, *ApJ*, 748, 93
- Rojas-Ayala, B., Hilton, E. J., Mann, A. W., et al. 2013, *Astronomische Nachrichten*, 334, 155
- Röser, S., Schilbach, E., Piskunov, A. E., Kharchenko, N. V., & Scholz, R. D. 2011, *A&A*, 531, A92
- Scalo, J. M. 1986, *Fund. Cosmic Phys.*, 11, 1
- Scelsi, L., Maggio, A., Micela, G., et al. 2007, *A&A*, 468, 405
- Schöfer, P., Jeffers, S. V., Reiners, A., et al. 2019, *A&A*, 623, A44
- Scholz, R. D., Meusinger, H., & Jahreiß, H. 2005, *A&A*, 442, 211
- Schweitzer, A., Passegger, V. M., Cifuentes, C., et al. 2019, *A&A*, 625, A68
- Shkolnik, E. L., Allers, K. N., Kraus, A. L., Liu, M. C., & Flagg, L. 2017, *AJ*, 154, 69
- Skrutskie, M. F., Cutri, R. M., Stiening, R., et al. 2006, *AJ*, 131, 1163
- Smart, R. L., Marocco, F., Caballero, J. A., et al. 2017, *MNRAS*, 469, 401
- Smart, R. L., Marocco, F., Sarro, L. M., et al. 2019, *MNRAS*, 485, 4423
- Smith, G. H. 2018, *Ap&SS*, 363, 235
- Stauffer, J. R. & Hartmann, L. W. 1986, *ApJS*, 61, 531
- Stelzer, B., Marino, A., Micela, G., López-Santiago, J., & Liefke, C. 2013, *MNRAS*, 431, 2063
- Stephenson, C. B. 1986, *AJ*, 91, 144
- Suárez Mascareño, A., González Hernández, J. I., Rebolo, R., et al. 2017a, *A&A*, 597, A108
- Suárez Mascareño, A., González Hernández, J. I., Rebolo, R., et al. 2017b, *A&A*, 605, A92
- Sun, M., Jiang, B. W., Zhao, H., et al. 2018, *ApJ*, 861, 153
- Tal-Or, L., Zechmeister, M., Reiners, A., et al. 2018, *A&A*, 614, A122
- Tarter, J. C., Backus, P. R., Mancinelli, R. L., et al. 2007, *Astrobiology*, 7, 30
- Taylor, M. B. 2005, in *Astronomical Society of the Pacific Conference Series*, Vol. 347, *Astronomical Data Analysis Software and Systems XIV*, ed. P. Shopbell, M. Britton, & R. Ebert, 29
- Terrien, R. C., Mahadevan, S., Bender, C. F., Deshpande, R., & Robertson, P. 2015, *ApJ*, 802, L10
- Tonry, J. L., Stubbs, C. W., Lykke, K. R., et al. 2012, *ApJ*, 750, 99
- Trifonov, T., Kürster, M., Zechmeister, M., et al. 2018, *A&A*, 609, A117
- Tuomi, M., Jones, H. R. A., Barnes, J. R., Anglada-Escudé, G., & Jenkins, J. S. 2014, *MNRAS*, 441, 1545
- van Altena, W. F. 1966, *AJ*, 71, 482
- van Altena, W. F., Lee, J. T., & Hoffleit, E. D. 1995, *The general catalogue of trigonometric [stellar] parallaxes*
- van Leeuwen, F. 2007, *A&A*, 474, 653
- van Rhijn, P. J. & Raimond, J. J. 1934, *MNRAS*, 94, 508
- Veeder, G. J. 1974, *AJ*, 79, 1056
- von Boetticher, A., Triaud, A. H. M. J., Queloz, D., et al. 2019, *A&A*, 625, A150
- von Braun, K., Boyajian, T. S., van Belle, G. T., et al. 2014, *MNRAS*, 438, 2413
- Vrba, F. J., Henden, A. A., Luginbuhl, C. B., et al. 2004, *AJ*, 127, 2948
- Weinberger, A. J., Boss, A. P., Keiser, S. A., et al. 2016, *AJ*, 152, 24
- Weis, E. W., Deluca, E. E., & Uppgren, A. R. 1979, *PASP*, 91, 766
- West, A. A., Bochanski, J. J., Hawley, S. L., et al. 2006, *AJ*, 132, 2507
- West, A. A., Hawley, S. L., Bochanski, J. J., et al. 2008, *AJ*, 135, 785
- West, A. A., Walkowicz, L. M., & Hawley, S. L. 2005, *PASP*, 117, 706
- Winters, J. G., Henry, T. J., Lurie, J. C., et al. 2015, *AJ*, 149, 5
- Woolf, V. M. & Wallerstein, G. 2005, *MNRAS*, 356, 963
- Yee, S. W., Petigura, E. A., & von Braun, K. 2017, *ApJ*, 836, 77
- Zacharias, N., Finch, C. T., Girard, T. M., et al. 2012, *VizieR Online Data Catalog*, 1322
- Zechmeister, M., Dreizler, S., Ribas, I., et al. 2019, *A&A*, 627, A49
- Zechmeister, M., Kürster, M., & Endl, M. 2009, *A&A*, 505, 859
- Zhang, Z. H., Pokorný, R. S., Jones, H. R. A., et al. 2009, *A&A*, 497, 619
- Zuckerman, B. & Song, I. 2004, *ARA&A*, 42, 685

Appendix A: Long tables and additional diagrams

Table A.1. Star candidates belonging to multiple systems not tabulated by the Washington Double Star Catalog (WDS).

Identifier	Name ^a	Spectral type	α (J2015.5)	δ (J2015.5)	π [mas]	$\mu_{\alpha} \cos \delta$ [mas a ⁻¹]	μ_{δ} [mas a ⁻¹]	μ_{total} [mas a ⁻¹]	G [mag]	θ [deg]	ρ [arcsec]
J00026+383	2M J00024011+3821453	M4.0 V	00:02:40.00	+38:21:44.1	24.54 ± 0.24	-70.31 ± 0.27	-22.34 ± 0.19	73.77 ± 0.27	13.1900 ± 0.0012	34.0	1.419
			00:02:40.06	+38:21:45.4	24.16 ± 0.38	-57.16 ± 0.54	-35.59 ± 0.20	67.33 ± 0.47	13.3648 ± 0.0014		
I01007+2356	PM J01007+2356	K7 V	01:00:46.85	+23:56:54.4	24.75 ± 0.04	129.88 ± 0.06	8.41 ± 0.06	130.15 ± 0.06	10.7186 ± 0.0007	4.7	1.480
			01:00:46.85	+23:56:55.9	14.6491 ± 0.0089		
J01074-025	RAVE J010727.5-023326	K5 V	01:07:27.46	-02:33:27.4	6.77 ± 0.05	-54.38 ± 0.09	-62.33 ± 0.05	82.72 ± 0.07	12.1930 ± 0.0003	165.2	1.363
			01:07:27.48	-02:33:28.8	6.42 ± 0.08	-54.13 ± 0.17	-61.36 ± 0.07	81.82 ± 0.12	14.5322 ± 0.0020		
J02026+105	RX J0202.4+1034	M4.5 V	02:02:28.15	+10:34:51.9	70.43 ± 0.53	-54.60 ± 1.07	-96.95 ± 0.77	111.27 ± 0.85	11.8652 ± 0.0012	25.3	0.904
			02:02:28.18	+10:34:52.7	68.79 ± 1.20	-101.45 ± 2.02	-58.95 ± 1.43	117.33 ± 1.89	12.3296 ± 0.0064		
J02287+156	BPM 85139	M2.0 V	02:28:47.14	+15:38:53.6	28.53 ± 0.11	170.91 ± 0.18	-9.17 ± 0.17	171.15 ± 0.18	11.5139 ± 0.0037	147.7	0.814
			02:28:47.17	+15:38:52.9	13.0258 ± 0.0055		
J02289+226	BPM 85140	M2.0 V	02:28:58.41	+22:36:24.5	17.16 ± 0.04	148.78 ± 0.08	-48.74 ± 0.07	156.56 ± 0.08	11.3170 ± 0.0006	147.4	3.022
			02:28:58.52	+22:36:21.9	17.19 ± 0.53	134.47 ± 1.13	-36.20 ± 0.99	139.26 ± 1.12	12.0611 ± 0.0003		
J03207+397	LP 198-637	M1.5 V	03:20:45.41	+39:42:59.4	31.60 ± 0.51	126.71 ± 1.33	-129.25 ± 0.86	181.00 ± 1.12	10.9868 ± 0.0020	278.1	0.783
			03:20:45.35	+39:42:59.7	11.2553 ± 0.0065		
I03276+0956	GJ 3226	K7 V	03:27:38.21	+09:56:05.3	22.80 ± 0.09	77.33 ± 0.15	-24.81 ± 0.14	81.22 ± 0.15	10.5483 ± 0.0014	296.8	1.541
			03:27:38.12	+09:56:06.0	23.82 ± 0.12	57.31 ± 0.19	-13.65 ± 0.21	58.91 ± 0.19	10.5825 ± 0.0008		
J03284+352	LSPM J0328+3515	M2.0 V	03:28:29.35	+35:15:18.7	20.90 ± 0.09	99.21 ± 0.15	-121.12 ± 0.08	156.56 ± 0.11	12.1366 ± 0.0007	204.2	1.230
			03:28:29.31	+35:15:17.5	21.14 ± 0.09	95.48 ± 0.15	-108.47 ± 0.08	144.51 ± 0.12	12.1711 ± 0.0010		
J03544-091	StKM 1-430	M1.0 V	03:54:25.52	-09:09:29.2	47.39 ± 0.04	-95.44 ± 0.06	110.84 ± 0.05	146.27 ± 0.06	10.5351 ± 0.0006	153.2	3.177
			03:54:25.62	-09:09:32.1	47.40 ± 0.06	-96.46 ± 0.09	98.93 ± 0.08	138.17 ± 0.09	11.8800 ± 0.0012		
J05530+047	G 106-007	M1.5 V	05:53:04.74	+04:43:02.7	24.70 ± 0.10	258.57 ± 0.28	-295.56 ± 0.20	392.71 ± 0.24	11.3303 ± 0.0011	278.1	1.517
			05:53:04.64	+04:43:02.9	15.8285 ± 0.0108		
I07245+1836	PM J07245+1836	K7 V	07:24:32.30	+18:36:31.3	19.99 ± 0.05	53.55 ± 0.09	-36.35 ± 0.08	64.72 ± 0.09	10.8267 ± 0.0005	326.9	1.836
			07:24:32.23	+18:36:32.9	12.6023 ± 0.0024		
J07418+050 ^b	G 050-001	M2.5 V+	07:41:52.56	+05:02:23.1	36.09 ± 0.07	-248.35 ± 0.13	-87.34 ± 0.10	263.26 ± 0.12	11.6216 ± 0.0009	136.1	1.006
			07:41:52.61	+05:02:22.4	16.1257 ± 0.0263		
J07545-096	2M J07543272-0941478	M3.5 V	07:54:32.61	-09:41:47.9	27.81 ± 0.10	-91.49 ± 0.16	-13.16 ± 0.11	92.43 ± 0.16	12.6737 ± 0.0014	129.9	1.233
			07:54:32.67	-09:41:48.7	13.9321 ± 0.0029		
I08192+5752	PM J08192+5752	K7 V	08:19:14.01	+57:52:26.8	19.67 ± 0.04	39.66 ± 0.06	-79.76 ± 0.06	89.08 ± 0.06	10.7381 ± 0.0005	93.3	1.475
			08:19:14.19	+57:52:26.6	19.71 ± 0.14	40.66 ± 0.23	-72.23 ± 0.46	82.89 ± 0.42	14.1599 ± 0.0067		
J09050+028	LP 546-48	M1.5 V	09:05:04.12	+02:50:03.8	42.58 ± 0.25	-312.21 ± 0.39	29.17 ± 0.42	313.57 ± 0.39	10.9288 ± 0.0021	253.0	1.214
			09:05:04.04	+02:50:03.5	12.1972 ± 0.0021		
J09527+554	G 195-043	M1.5 V	09:52:45.24	+55:28:16.3	28.51 ± 0.36	298.92 ± 0.59	-201.23 ± 0.64	360.34 ± 0.61	11.3624 ± 0.0008	331.1	2.716
			09:52:45.14	+55:28:18.9	27.15 ± 0.12	285.07 ± 0.23	-190.75 ± 0.15	343.00 ± 0.21	16.4864 ± 0.0034		
I10526+0029	PM J10526+0029	K7 V	10:52:39.52	+00:29:01.5	25.18 ± 0.08	-91.32 ± 0.10	-31.13 ± 0.08	96.48 ± 0.09	10.1687 ± 0.0016	251.0	1.594
			10:52:39.42	+00:29:01.0	12.7067 ± 0.0042		
I11585+4626 ^c	PM J11585+4626	K7 V	11:58:33.82	+46:26:28.9	16.20 ± 0.06	-129.71 ± 0.07	1.77 ± 0.06	129.72 ± 0.07	10.9651 ± 0.0011	333.9	1.540
			11:58:33.77	+46:26:30.4	14.50 ± 0.14	-141.05 ± 0.31	1.26 ± 0.17	141.05 ± 0.31	11.5845 ± 0.0015		
J12191+318 ^b	LP 320-626	M4.0 V+	12:19:05.57	+31:50:43.6	11.1940 ± 0.0006	225.2	1.764
			12:19:05.48	+31:50:42.2	35.13 ± 0.09	-295.73 ± 0.10	5.02 ± 0.11	295.77 ± 0.10	13.9526 ± 0.0023		
J12390+470	G 123-049	M2.0 V	12:39:05.24	+47:02:21.4	11.1336 ± 0.0044	110.4	0.463
			12:39:05.28	+47:02:21.2	43.50 ± 0.05	384.45 ± 0.07	-118.41 ± 0.08	402.27 ± 0.07	11.2091 ± 0.0009		
J12513+221	GJ 1166A	M3.0 V	12:51:23.72	+22:06:15.7	30.32 ± 0.51	-177.34 ± 0.98	50.54 ± 0.79	184.40 ± 0.96	12.1313 ± 0.0019	91.8	1.263
			12:51:23.81	+22:06:15.6	13.3117 ± 0.0038		
J13282+300	BD+30 2400	M0.0 V	13:28:17.54	+30:02:43.1	25.33 ± 0.08	-186.41 ± 0.25	-183.87 ± 0.13	261.84 ± 0.20	10.5043 ± 0.0006	320.1	1.243

Table A.1. continued.

Identifier	Name ^a	Spectral type	α (J2015.5)	δ (J2015.5)	π [mas]	$\mu_{\alpha} \cos \delta$ [mas a ⁻¹]	μ_{δ} [mas a ⁻¹]	μ_{total} [mas a ⁻¹]	G [mag]	θ [deg]	ρ [arcsec]
J13445+249	LP 379-098	M1.0 V	13:28:17.48 13:44:33.39	+30:02:44.1 +24:57:03.7	14.1569 ± 0.0103 11.5057 ± 0.0021	355.8	0.879
J13490+026	Wolf 1495	M1.5 V	13:44:33.39 13:49:01.18	+24:57:04.6 +02:47:23.3	11.8891 ± 0.0098 10.7706 ± 0.0210	315.7	0.680
I15380+3224 ^c	PM J15380+3224	K7 V	13:49:01.15 15:38:04.49	+02:47:23.8 +32:24:31.9	55.78 ± 0.75	149.68 ± 1.64	-333.14 ± 1.56	365.22 ± 1.57	10.8252 ± 0.0075 11.2639 ± 0.0021	143.8	1.061
J16573+271	2M J16572235+2708304	M2.0 V	15:38:04.53 16:57:22.27	+32:24:31.0 +27:08:31.1	15.10 ± 0.25	-74.75 ± 0.39	-83.43 ± 0.48	112.02 ± 0.44	11.3307 ± 0.0019 12.3752 ± 0.0011	117.6	1.048
I17068+3212	PM J17068+3212	K7 V	16:57:22.34 17:06:48.88	+27:08:30.6 +32:11:59.3	13.2959 ± 0.0025 10.7788 ± 0.0003	31.4	3.279
J18116+061	NLTT 46076	M3.0 V	17:06:49.00 18:11:36.49	+32:12:02.2 +06:06:27.8	31.93 ± 0.03	46.05 ± 0.09	-82.76 ± 0.06	94.71 ± 0.07	12.6244 ± 0.0004 11.9662 ± 0.0074	139.6	0.625
J18400+726	LP 044-334	M6.5 V	18:11:36.51 18:40:02.20	+06:06:27.3 +72:40:57.1	13.5146 ± 0.0077 15.3854 ± 0.0114	110.3	0.821
I18447+6241	PM J18447+6241	K7 V	18:40:02.32 18:44:47.49	+72:40:56.5 +62:41:08.3	15.7040 ± 0.0035 10.7927 ± 0.0006	277.5	1.342
I21088+1247	BD+12 4554	K7 V	18:44:47.30 21:08:51.84	+62:41:08.7 +12:47:36.9	14.7260 ± 0.0167 10.4390 ± 0.0005	2.5	1.833
I21415+4925	PM J21415+4925	K7 V	21:08:51.85 21:41:31.36	+12:47:38.7 +49:25:38.1	14.4780 ± 0.0077 9.9125 ± 0.0003	308.8	1.609
J22012+323	TYC 2723-908-1	M1.5 V	21:41:31.26 22:01:14.12	+49:25:39.3 +32:23:13.9	30.10 ± 0.10	50.32 ± 0.60	-88.08 ± 0.83	101.44 ± 0.78	13.2790 ± 0.0044 11.4391 ± 0.0012	239.8	1.295
I22142+1712	PM J22142+1712	K7 V	22:01:14.04 22:14:12.84	+32:23:13.1 +17:12:24.4	32.10 ± 0.20	107.88 ± 0.27	53.40 ± 0.31	120.37 ± 0.28	12.8902 ± 0.0022 10.7551 ± 0.0006	268.2	1.510
I22569+0031	PM J22569+0031	K7 V	22:14:12.73 22:56:54.65	+17:12:24.4 +00:31:23.6	15.4819 ± 0.0194 10.9107 ± 0.0145	22.4	0.907
I22596+2154	PM J22596+2154	K7 V	22:56:54.67 22:59:41.42	+00:31:24.4 +21:54:05.8	17.57 ± 0.68	13.04 ± 1.16	-82.42 ± 0.87	83.44 ± 0.88	11.0021 ± 0.0058 10.1878 ± 0.0006	37.3	2.093
J23051+452	LSPM J2305+4517	M3.5 V	22:59:41.51 23:05:08.99	+21:54:07.6 +45:17:32.9	13.3417 ± 0.0037 12.3370 ± 0.0021	80.7	0.785
J23489+098	[R78b] 377	M1.0 V	23:05:09.06 23:48:58.97	+45:17:33.1 +09:51:53.4	14.3079 ± 0.0029 11.3848 ± 0.0009	20.1	1.945
J23590+208	G 129-051	M2.5 V	23:48:59.02 23:59:00.73	+09:51:55.2 +20:51:37.3	20.76 ± 0.08	141.19 ± 0.18	-43.69 ± 0.06	147.80 ± 0.17	13.9181 ± 0.0013 12.0177 ± 0.0072	170.7	0.521
			23:59:00.73 23:59:00.73	+20:51:36.7 +20:51:36.7	12.3273 ± 0.0186		

Notes. ^(a) Primaries “A” are always brighter than secondaries “B” in the G band. ^(b) Previously identified as spectroscopic binaries in [Reiners et al. \(2012\)](#) and [Jeffers et al. \(2018\)](#). ^(c) Common proper motion pairs with $\Delta\pi > 5\%$ labelled in Fig. 8.

Table A.2. continued.

Spectral type	$r - i$ [mag]	$i - G_{RP}$ [mag]	$G_{RP} - J$ [mag]	$J - H$ [mag]	$H - K_s$ [mag]	$K_s - W1$ [mag]	$W1 - W2$ [mag]	$W2 - W3$ [mag]	$W3 - W4$ [mag]
K5 V	0.41 ± 0.07 (13)	0.40 ± 0.20 (12)	0.95 ± 0.06 (13)	0.57 ± 0.03 (14)	0.14 ± 0.03 (14)	0.08 ± 0.06 (14)	0.04 ± 0.19 (15)	-0.02 ± 0.20 (15)	0.01 ± 0.13 (10)
K7 V	0.60 ± 0.12 (106)	0.34 ± 0.12 (99)	1.12 ± 0.05 (104)	0.63 ± 0.03 (112)	0.17 ± 0.03 (112)	0.11 ± 0.04 (109)	-0.03 ± 0.06 (109)	0.05 ± 0.06 (112)	0.06 ± 0.11 (112)
M0.0 V	0.74 ± 0.14 (119)	0.36 ± 0.11 (117)	1.22 ± 0.05 (118)	0.63 ± 0.04 (120)	0.19 ± 0.03 (119)	0.12 ± 0.05 (116)	0.02 ± 0.09 (117)	0.02 ± 0.08 (119)	0.10 ± 0.09 (118)
M0.5 V	0.80 ± 0.13 (70)	0.36 ± 0.08 (71)	1.28 ± 0.05 (72)	0.63 ± 0.03 (72)	0.21 ± 0.03 (71)	0.12 ± 0.05 (70)	0.05 ± 0.09 (70)	0.03 ± 0.07 (71)	0.11 ± 0.09 (73)
M1.0 V	0.87 ± 0.11 (140)	0.36 ± 0.09 (139)	1.32 ± 0.04 (139)	0.62 ± 0.04 (140)	0.21 ± 0.03 (138)	0.14 ± 0.04 (138)	0.05 ± 0.09 (138)	0.06 ± 0.06 (138)	0.09 ± 0.11 (141)
M1.5 V	0.96 ± 0.14 (124)	0.37 ± 0.11 (121)	1.37 ± 0.05 (119)	0.63 ± 0.04 (121)	0.21 ± 0.03 (121)	0.14 ± 0.04 (122)	0.06 ± 0.08 (121)	0.06 ± 0.06 (123)	0.09 ± 0.11 (125)
M2.0 V	1.05 ± 0.12 (125)	0.38 ± 0.11 (126)	1.44 ± 0.05 (127)	0.61 ± 0.05 (128)	0.23 ± 0.03 (128)	0.15 ± 0.04 (126)	0.09 ± 0.07 (126)	0.07 ± 0.05 (126)	0.10 ± 0.12 (122)
M2.5 V	1.17 ± 0.11 (147)	0.40 ± 0.10 (144)	1.51 ± 0.05 (147)	0.59 ± 0.04 (150)	0.24 ± 0.03 (147)	0.16 ± 0.05 (147)	0.11 ± 0.05 (149)	0.08 ± 0.04 (149)	0.12 ± 0.13 (144)
M3.0 V	1.29 ± 0.11 (173)	0.41 ± 0.10 (172)	1.58 ± 0.05 (172)	0.59 ± 0.04 (172)	0.25 ± 0.03 (171)	0.16 ± 0.04 (173)	0.13 ± 0.05 (172)	0.09 ± 0.05 (172)	0.13 ± 0.14 (162)
M3.5 V	1.40 ± 0.13 (240)	0.44 ± 0.12 (235)	1.66 ± 0.05 (237)	0.58 ± 0.05 (242)	0.26 ± 0.03 (241)	0.17 ± 0.04 (241)	0.15 ± 0.05 (239)	0.10 ± 0.05 (239)	0.15 ± 0.15 (226)
M4.0 V	1.53 ± 0.15 (205)	0.47 ± 0.13 (201)	1.76 ± 0.06 (202)	0.58 ± 0.04 (206)	0.27 ± 0.03 (206)	0.18 ± 0.04 (201)	0.17 ± 0.04 (200)	0.12 ± 0.04 (199)	0.19 ± 0.17 (169)
M4.5 V	1.71 ± 0.13 (116)	0.49 ± 0.09 (116)	1.87 ± 0.06 (116)	0.56 ± 0.04 (116)	0.29 ± 0.03 (116)	0.20 ± 0.04 (114)	0.19 ± 0.03 (114)	0.15 ± 0.04 (115)	0.23 ± 0.21 (88)
M5.0 V	1.85 ± 0.21 (59)	0.59 ± 0.14 (59)	2.02 ± 0.12 (61)	0.58 ± 0.03 (62)	0.31 ± 0.03 (62)	0.21 ± 0.03 (62)	0.20 ± 0.03 (61)	0.16 ± 0.04 (60)	0.28 ± 0.28 (43)
M5.5 V	2.12 ± 0.15 (26)	0.64 ± 0.13 (26)	2.14 ± 0.08 (27)	0.57 ± 0.04 (27)	0.33 ± 0.02 (26)	0.23 ± 0.03 (26)	0.21 ± 0.05 (27)	0.17 ± 0.05 (27)	0.23 ± 0.16 (21)
M6.0 V	2.32 ± 0.25 (13)	0.83 ± 0.12 (12)	2.33 ± 0.16 (12)	0.60 ± 0.08 (15)	0.37 ± 0.03 (15)	0.23 ± 0.02 (15)	0.21 ± 0.04 (15)	0.21 ± 0.07 (15)	0.33 ± 0.22 (5)
M6.5 V	2.68 ± 0.14 (7)	0.82 ± 0.10 (7)	2.49 ± 0.07 (7)	0.61 ± 0.03 (7)	0.37 ± 0.02 (7)	0.24 ± 0.04 (7)	0.20 ± 0.03 (7)	0.23 ± 0.03 (7)	0.10 ± 0.15 (4)
M7.0 V	2.62 ± 0.26 (5)	0.99 ± 0.15 (5)	2.52 ± 0.17 (5)	0.58 ± 0.06 (5)	0.38 ± 0.04 (5)	0.26 ± 0.09 (5)	0.21 ± 0.03 (5)	0.23 ± 0.08 (5)	0.21 ± 0.07 (3)
M7.5 V	2.66 ± 0.09 (3)	0.91 ± 0.05 (3)	2.52 ± 0.09 (3)	0.64 ± 0.01 (3)	0.37 ± 0.03 (3)	0.25 ± 0.05 (3)	0.21 ± 0.01 (3)	0.27 ± 0.06 (3)	...
M8.0 V	2.77 ± 0.10 (6)	1.03 ± 0.10 (6)	2.75 ± 0.12 (9)	0.66 ± 0.03 (9)	0.41 ± 0.03 (9)	0.25 ± 0.04 (9)	0.24 ± 0.05 (9)	0.28 ± 0.04 (8)	...
M8.5 V	2.70 ± 0.05 (2)	1.12 ± 0.02 (2)	2.93 ± 0.05 (4)	0.64 ± 0.05 (4)	0.46 ± 0.01 (4)	0.33 ± 0.04 (4)	0.28 ± 0.05 (4)	0.35 ± 0.08 (4)	0.32 ± 0.05 (3)
M9.0 V	2.43 ± 0.09 (2)	1.17 ± 0.02 (3)	3.06 ± 0.08 (5)	0.67 ± 0.06 (5)	0.46 ± 0.04 (5)	0.35 ± 0.03 (5)	0.29 ± 0.03 (5)	0.49 ± 0.08 (5)	0.30 (1)
M9.5 V	2.39 (1)	1.18 (1)	3.12 ± 0.11 (2)	0.84 ± 0.07 (2)	0.57 ± 0.03 (2)	0.34 ± 0.02 (2)	0.28 ± 0.02 (2)	0.45 ± 0.08 (2)	...
L0.0	2.43 ± 0.16 (10)	1.16 ± 0.03 (9)	3.07 ± 0.05 (11)	0.75 ± 0.05 (12)	0.50 ± 0.05 (12)	0.33 ± 0.04 (12)	0.27 ± 0.04 (12)	0.49 ± 0.15 (12)	...
L0.5	2.38 ± 0.19 (5)	1.17 ± 0.02 (4)	3.15 ± 0.06 (6)	0.73 ± 0.06 (7)	0.53 ± 0.06 (7)	0.33 ± 0.02 (7)	0.26 ± 0.02 (7)	0.45 ± 0.07 (7)	...
L1.0	2.41 ± 0.10 (14)	1.20 ± 0.04 (14)	3.18 ± 0.10 (15)	0.82 ± 0.05 (15)	0.51 ± 0.06 (15)	0.36 ± 0.05 (15)	0.24 ± 0.04 (15)	0.46 ± 0.10 (14)	...
L1.5	2.39 ± 0.03 (5)	1.23 ± 0.06 (4)	3.23 ± 0.06 (7)	0.80 ± 0.08 (8)	0.52 ± 0.04 (8)	0.40 ± 0.09 (8)	0.27 ± 0.03 (8)	0.55 ± 0.11 (6)	...
L2.0	2.34 ± 0.08 (12)	1.16 ± 0.03 (11)	3.24 ± 0.10 (12)	0.85 ± 0.09 (14)	0.53 ± 0.07 (14)	0.40 ± 0.06 (14)	0.27 ± 0.02 (14)	0.54 ± 0.15 (14)	...
L2.5	2.31 ± 0.05 (5)	1.20 ± 0.04 (4)	3.31 ± 0.07 (5)	0.91 ± 0.04 (6)	0.54 ± 0.08 (6)	0.45 ± 0.06 (6)	0.26 ± 0.03 (6)	0.56 ± 0.32 (6)	...
L3.0	2.34 ± 0.11 (5)	1.25 ± 0.01 (2)	3.48 ± 0.09 (3)	1.00 ± 0.08 (6)	0.64 ± 0.07 (6)	0.58 ± 0.09 (6)	0.33 ± 0.07 (6)	0.43 ± 0.17 (6)	...
L3.5	2.40 ± 0.11 (2)	1.35 ± 0.04 (2)	3.37 ± 0.03 (2)	0.93 ± 0.05 (2)	0.58 ± 0.05 (2)	0.58 ± 0.06 (2)	0.30 ± 0.01 (2)	0.53 ± 0.13 (2)	...
L4.0	2.22 ± 0.13 (4)	1.31 ± 0.07 (3)	3.50 ± 0.15 (4)	0.90 ± 0.09 (5)	0.57 ± 0.07 (5)	0.53 ± 0.09 (5)	0.27 ± 0.02 (5)	0.32 ± 0.14 (5)	...
L4.5	2.06 (1)	1.13 (1)	0.69 (1)	0.82 (1)	0.37 (1)	0.66 (1)	...
L5.0	2.15 ± 0.21 (5)	1.53 (1)	3.75 (1)	1.01 ± 0.16 (5)	0.59 ± 0.14 (5)	0.70 ± 0.09 (5)	0.38 ± 0.11 (6)	0.52 ± 0.33 (6)	...
L5.5	2.13 (1)	0.88 (1)	0.56 (1)	0.67 (1)	0.28 (1)	0.62 (1)	...
L6.0	2.07 (1)	1.71 (1)	3.49 (1)	0.69 (1)	0.34 (1)	0.75 (1)	0.34 (1)	0.76 (1)	...
L6.5	1.92 (1)	1.00 (1)	0.59 (1)	0.76 (1)	0.37 (1)	0.61 (1)	...
L7.0
L7.5	2.14 (1)	1.18 (1)	0.70 (1)	0.88 (1)	0.47 (1)	1.10 (1)	...
L8.0

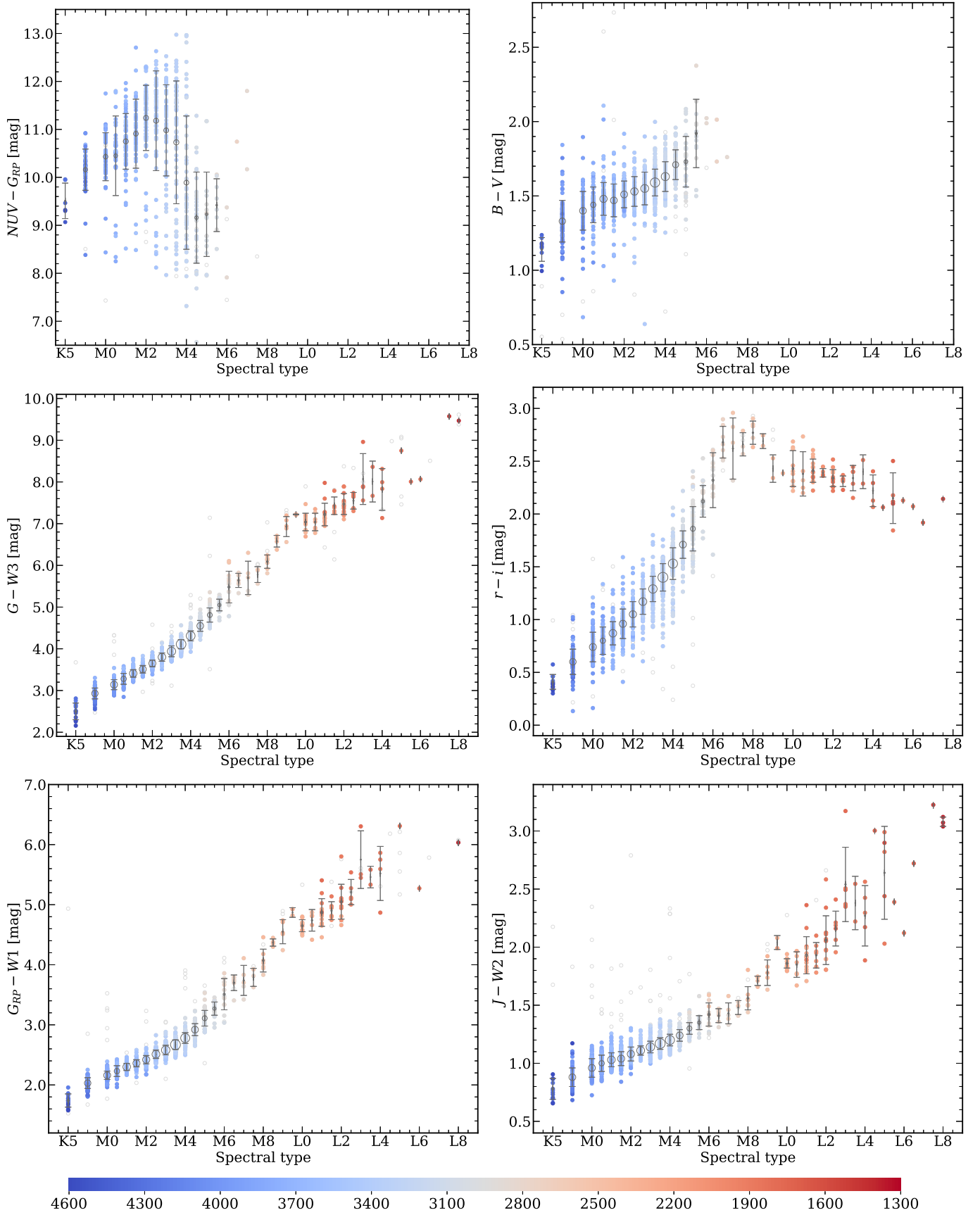


Fig. A.1. Six representative colour-spectral type diagrams, colour-coded by effective temperature.

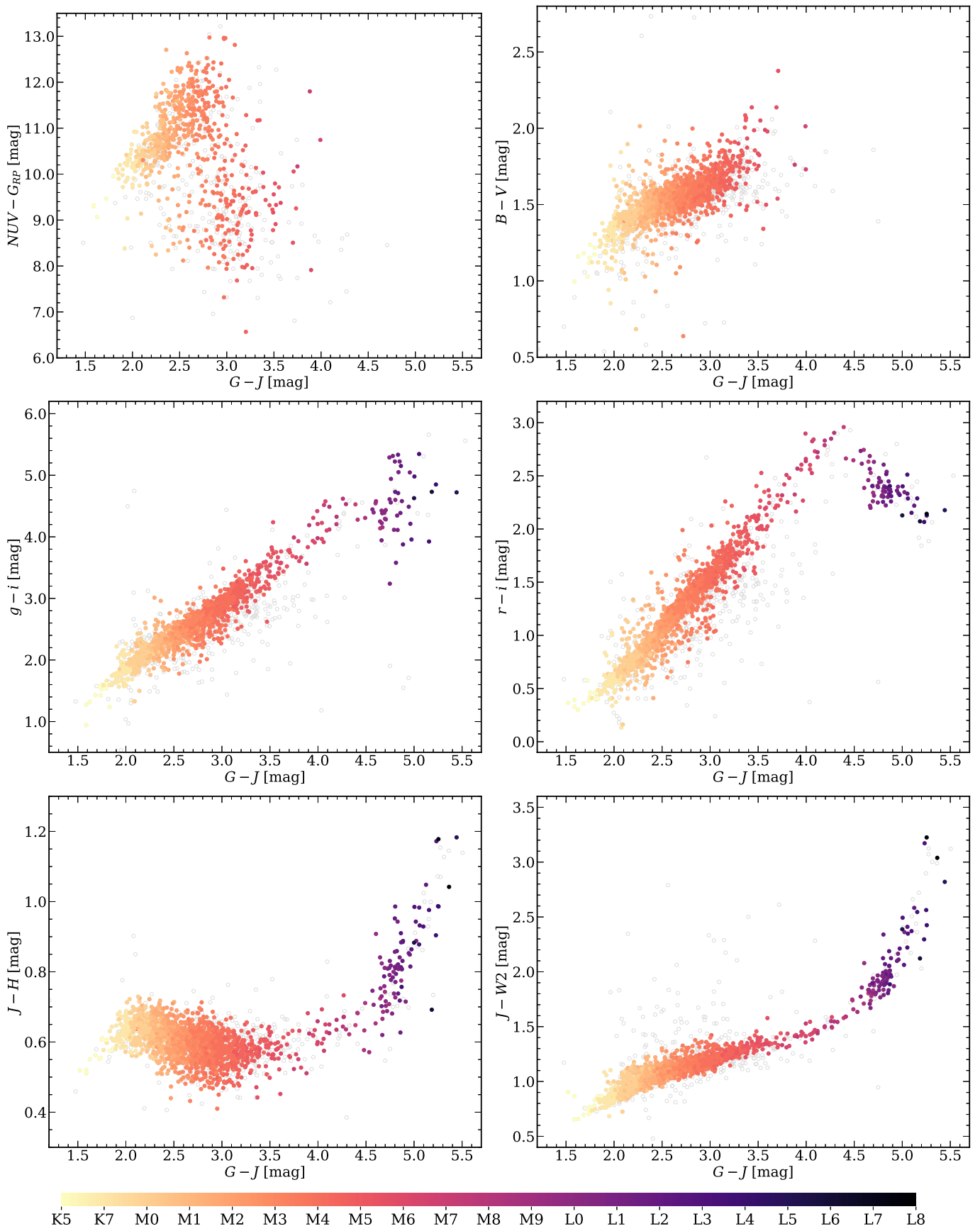


Fig. A.2. Six representative colour-colour diagrams, colour-coded by spectral type.